UC-106
LBL-27956

Lawrence Berkeley Laboratory
UNIVERSITY OF CALIFORNIA

APPLIED SCIENCE DIVISION

The Continuous Crystallization of Sulfur Formed by the Liquid-Phase Reaction of Hydrogen Sulfide and Sulfur Dioxide

C.A. Stevens* and S. Lynn

*(Ph.D. Thesis)

September 1989

For Reference

Not to be taken from this room

APPLIED SCIENCE DIVISION

LBL-27956 Copy 1
Bldg. 50 Library.

Prepared for the U.S. Department of Energy under Contract Number DE-AC03-76SF00098.

DISCLAIMER

This document was prepared as an account of work sponsored by the United States Government. While this document is believed to contain correct information, neither the United States Government nor any agency thereof, nor the Regents of the University of California, nor any of their employees, makes any warranty, express or implied, or assumes any legal responsibility for the accuracy, completeness, or usefulness of any information, apparatus, product, or process disclosed, or represents that its use would not infringe privately owned rights. Reference herein to any specific commercial product, process, or service by its trade name, trademark, manufacturer, or otherwise, does not necessarily constitute or imply its endorsement, recommendation, or favoring by the United States Government or any agency thereof, or the Regents of the University of California. The views and opinions of authors expressed herein do not necessarily state or reflect those of the United States Government or any agency thereof or the Regents of the University of California.

LBL-27956

THE CONTINUOUS CRYSTALLIZATION OF SULFUR FORMED BY THE LIQUID-PHASE REACTION OF HYDROGEN SULFIDE AND SULFUR DIOXIDE

by

Craig A. Stevens and Scott Lynn

Applied Sciences Division
Lawrence Berkeley Laboratory
1 Cyclotron Road
Berkeley, California 94720

September 1989

This work was supported by the Morgantown Energy Technology Center, Assistant Secretary for Fossil Energy, Office of Coal Utilization, Advanced Research and Technology Development, Division of Surface Coal Gasification through the U.S. Department of Energy under Contract No. DE-AC03-76SF00098.

The Continuous Crystallization of Sulfur Formed by the Liquid-Phase Reaction of Hydrogen Sulfide and Sulfur Dioxide

Craig Aldred Stevens

Abstract

The crystallization of elemental sulfur is a unit operation in a process being developed to remove hydrogen sulfide from industrial gas streams. The sulfur is formed by the irreversible, liquid-phase reaction of hydrogen sulfide (H_2S) and sulfur dioxide (SO_2). The crystals produced from the process solvent must be high-quality, marketable sulfur. In addition, the size and shape of the sulfur crystals must be conducive to easy separation of the crystals from the process solvent. Information on the effects of process design parameters on both crystal-size distribution and sulfur quality is required to design and operate the reactor/crystallizer.

Low-temperature sulfur solubility data in triethylene glycol dimethyl ether (Triglyme) and diethylene glycol methyl ether (DGM) were collected. The effects of temperature and water concentration in the solvents on sulfur solubility were correlated. The thermal crystallization of sulfur from Triglyme was studied in a laboratory-scale experimental crystallizer. The dependence of crystal-size distribution on residence time, slurry density, impeller power input, and water concentration in the solvent was determined. A crystallization model, applicable to the experimental crystallizer, was derived from population balance theory and verified using the experimental data. The crystallization kinetics of the sulfur/Triglyme system were obtained from the crystallization model. The reactive crystallization of sulfur formed by the reaction between H_2S and SO_2 was also studied. A reactor/crystallizer model was developed from the reaction kinetics and from the thermal crystallization kinetics. Reactive crystallization experiments verified the model. An industrial-sized reactor/crystallizer was designed from the model. The purity and morphology of the sulfur crystals produced from both thermal and reactive crystallization experiments indicate that a marketable sulfur product can be produced.

Acknowledgments

While attending U.C. Berkeley, I've had the good fortune to work with many generous and talented people. Their eagerness to help and to share their ideas has enriched my stay. I've thoroughly enjoyed working with Professor Scott Lynn. His careful attention and guidance have provided an excellent environment for chemical engineering research. He knew when to let me go and when to set me straight. I learned a great deal more than chemical engineering from Professor Lynn. My labmates deserve my utmost gratitude for their friendship and, when necessary, their abuse. I want to thank Steve Sciamanna and Marshall Hix for showing me the nuts and bolts of experimentation. Dan Neumann was instrumental in securing my addiction to computers. Dave Weingaertner helped me build the monster walk-in hood. Tom Colson always reminded me to "lighten up." I owe Jim Russell for some great ultimate frisbee games. Dannes Hutapea showed me that a Mac really is a useful machine. Thanks to Kay Ekman and Ferne Kasarda for their help in interfacing with the monolithic U.C. system. Their pleasant company was an oasis in Gilman Hall.

My wife, Nancy, has been a great source of emotional support. Her enthusiasm and love have helped me to retain my perspective and to return to the lab the next day. She rejoiced with me when victorious and consoled me when defeated. My parents and parents-in-law have always given their love and support. They've helped me to keep my sense of humor and shown me that things really aren't all that bad. When I was young, my father nudged me into the engineering world. Thanks Dad.

The HIAC PSA-720 was loaned to me by Mr. Lee Miller. Without it, this work would have been far more difficult. I sincerely appreciate his philanthropy.

This work was supported by the Morgantown Energy Technology Center, Assistant Secretary for Fossil Energy, Office of Coal Utilization, Advanced Research and Technology Development, Division of Surface Coal Gasification, through the Department of Energy under contract DE-AC03-76SF00098.

TABLE OF CONTENTS

Chapter 1: Introduction 1

1.1 Why Crystallize Sulfur? 1

1.2 Conventional Technology 1

1.3 The UCB Sulfur Recovery Process 2

1.4 Sulfur Crystallization 4

1.5 Scope of Crystallization Work 5

Chapter 2: Low Temperature Sulfur Solubility 10

2.1 Preface 10

2.2 Solid-Liquid Equilibrium Theory 10

2.2.1 Solid Solubility in Pure Solvents 10
2.2.2 Solid Solubility Near the Solid Melting Temperature 12
2.2.3 Effect of Temperature on Solid Solubility 13

2.3 Experimental Apparatus 14

2.4 Experimental Method 14

2.5 Sulfur Solubility in Triglyme and Dowanol DM 16

2.5.1 Sulfur Solubility in Triglyme 17
2.5.2 Sulfur Solubility in Dowanol DM 17
2.5.3 Results and Discussion 18

2.6 Effect of Water on Sulfur Solubility 19

2.6.1 Effect of Water on Sulfur Solubility in Triglyme 19
2.6.2 Effect of Water on Sulfur Solubility Dowanol DM 20

2.7 Summary 20

Chapter 3: Thermal Crystallization 33

3.1 Preface 33

3.2 Crystal-Size Distribution Theory 34

3.2.1 Ideal Crystallizer Model 36
3.2.2 Modified Crystallizer Model 40
3.2.3 Comparison of Models 43
3.2.4 Effect of Residence Time on Models 43
3.2.5 Effect of Slurry Density on Models 45
3.2.6 Effect of Impeller Power Input on Models 46

3.3 Thermal Crystallization Experimental Apparatus 47

3.3.1 Back-Mixed Crystallizer 47
3.3.2 Fluidized-Bed Crystallizer 49
3.3.3 Apparatus for Analyzing the Crystal-Size Distribution 50

3.4 Experimental Method 52

3.4.1 Back-Mixed Crystallizer Operation 52
3.4.2 Fluidized-Bed Crystallizer Operation 54
3.4.3 Crystal-Size Distribution Analysis 55
3.4.4 Data Reduction 56
3.4.5 Operating Parameters for the Experimental Crystallizer 58

3.4.5.1 Variable Residence Time 58
3.4.5.2 Variable Slurry Density 58
3.4.5.3 Variable Impeller Power Input 59
3.4.5.4 Variable Water Concentration in the Solvent 59

3.5 Computational Method and Data Analysis 60

3.5.1 Ideal Crystallizer Model 61
3.5.2 Modified Crystallizer Model 62
3.5.3 Effect of Operating Parameters on Models 63

3.5.3.1 Variable Residence Time 64
3.5.3.2 Variable Slurry Density 66
3.5.3.3 Variable Impeller Power Input 68
3.5.3.4 Variable Water Concentration in the Solvent 71

3.6 Back-Mixed Crystallizer Results and Discussion 73

3.6.1 Experimental Crystal-Size Distribution 74

3.6.1.1 Application of the Ideal Crystallizer Model 74
3.6.1.2 Application of the Modified Crystallizer Model 75
3.6.1.3 Verification of the Crystallizer Model Assumptions 78

3.6.2 Dependence of Crystal-Size Distribution on Residence Time 78

3.6.2.1 Determination of the Kinetic Constants 79
3.6.2.2 Dependence of Model Parameters on Residence Time 80
3.6.2.3 Application of the Crystallizer Model with Constant Z 82
3.6.2.4 Sensitivity of the Design Equation to Critical Particle Size and Z 83

3.6.3 Dependence of Crystal-Size Distribution on Slurry Density 84

3.6.3.1 Determination of the Kinetic Constants 87
3.6.3.2 Dependence of Model Parameter Z on Slurry Density 89
3.6.3.3 Application of the Crystallizer Model with Constant Z 89
3.6.3.4 Prediction of the Experimental Data from the Design Equation 90

3.6.4 Dependence of Crystal-Size Distribution on Impeller Power Input 91

3.6.4.1 Minimum Impeller Rotation Rate 92
3.6.4.2 Effect of Impeller Rotation Rate on Crystal-Size Distribution 93
3.6.4.3 Determination of Impeller Power Input Exponent 93

3.6.5 Dependence of Crystal-Size Distribution on Water Concentration 96

3.6.5.1 Determination of Kinetic Constants 98
3.6.5.2 Prediction of the Experimental Data from the Design Equation 98

3.7 Fluidized-Bed Crystallizer Results and Discussion 99

3.8 Sulfur Purity and Morphology 100

3.8.1 Sulfur Purity Analysis 101

3.8.1.1 Method of the Sulfur Purity Analysis 101
3.8.1.2 Results and Discussion of the Sulfur Purity Analysis 102

3.8.2 Sulfur Morphology Analysis 102

3.9 Summary 103

3.10 Nomenclature 106

3.10.1 Variables for Crystallization Kinetics 106
3.10.2 Variables for HIAC Particle-Size Analyzer 107
3.10.3 Variables for Impeller Power and Rotation Rate Correlations 107
3.10.4 Variables for Water Concentration Determination 108

Chapter 4: Reactive Crystallization 145

4.1 Preface 145

4.2 Reactor/Crystallizer Model 146

4.2.1 Reaction Model 146
4.2.2 Crystallization Model 148

4.3 Experimental Apparatus 150

4.3.1 Back-Mixed Crystallizer 150
4.3.2 Fluidized-Bed Crystallizer 152

4.4 Experimental Method 152

4.4.1 Back-Mixed Crystallizer Operation 153
4.4.2 Fluidized-Bed Crystallizer Operation 155

4.5 Back-mixed Crystallizer Results and Discussion 155

4.5.1 Validity of the Reactor/Crystallizer Model 155
4.5.2 Use of the Reactor/Crystallizer Model 156

4.5.3 Comparison of the Experimental and Model Results 158
4.5.4 Effects of Reaction on Crystallization 159

4.6 Fluidized-Bed Crystallizer Results and Discussion 160

4.7 Sulfur Purity and Morphology 160

4.8 UCBSRP Reactor/Crystallizer Design 162

4.8.1 Reactor/Crystallizer: One CSTR 163
4.8.2 Reactor/Crystallizer: One CSTR and PFR 163
4.8.3 Reactor/Crystallizer: Three CSTR's and One PFR 165

4.9 Summary 166

4.10 Nomenclature 168

References 183

Appendix A 187

A.1 Experimental Data: Sulfur Solubility in Polyglycol Ether Solvents 188

A.2 Computer Programs for Data Regression 191

Appendix B 195

B.1 Sample HIAC Particle-Size Analysis 196

B.2 Computer Programs for Data Reduction and Analysis 198

B.2.1 ANALYSIS.FOR 198
B.2.2 DESIGN.FOR 217
B.2.3 CSD.FOR 219

B.3 Detailed Results of the Constrained MSCPR Analysis of Experimental Runs 221

Appendix C 224

C.1 Sample Calculations for an Experimental Run 224

CHAPTER 1

INTRODUCTION

1.1 Why Crystallize Sulfur?

Found in many industrial gas streams, hydrogen sulfide (H_2S) is toxic, corrosive, malodorous, and a catalyst poison. H_2S must therefore be removed from almost all industrial gas streams in which it is present. Conventional technology used to remove H_2S from gas streams such as gasified coal, natural gas, and refinery fuel gas has many shortcomings. A new process that overcomes these shortcomings is being developed to recover elemental sulfur from H_2S-laden gas streams. A unit operation in this new process is the crystallization of elemental sulfur from solution.

1.2 Conventional Technology

A typical treatment facility used to remove H_2S from sour gas streams is composed of three processing steps (Kohl and Riesenfeld, 1985). First, the H_2S is concentrated using an alkanolamine absorber and stripper, where the H_2S and other acid gases are removed from the bulk gas stream. The H_2S concentration specified for the treated gas is usually less than one ppm. This stringent specification requires an H_2S-free solvent stream at the top of the absorber and therefore requires a large heat load at the bottom of the amine stripper to rid the solvent of H_2S. Second, the concentrated H_2S gas stream is sent to the well-known Claus process, where the H_2S is converted to elemental sulfur by a high-temperature, catalytic, gas-phase reaction:

$$2\ H_2S + SO_2 \longleftrightarrow 3/x\ S_x + 2\ H_2O$$

The sulfur dioxide (SO_2) required in the reaction is produced by burning approximately one-third of the H_2S with air. The reaction is performed above the dew point of sulfur to prevent condensation on the alumina catalyst. The reaction is equilibrium-limited, which precludes total conversion of H_2S to elemental sulfur. The

typical conversion of the Claus process with three catalytic converters and intermediate sulfur condensation is approximately 98 percent. The molten sulfur produced from the Claus process is of extremely good quality. However, since Claus sulfur contains significant amounts of dissolved H_2S (~200 ppm) which can be hazardous, the molten sulfur is degassed before being sent to sales.

Third, the remaining sulfur compounds (H_2S and SO_2) in the Claus tail gas require additional processing. A large number and variety of Claus tail gas processes are used (Ferguson, 1975). Some processes remove the H_2S outright by converting it to elemental sulfur or to other substances. Other processes convert the tail gas sulfur compounds entirely to either H_2S or SO_2, then absorb and recycle the H_2S or SO_2 back to the Claus process (thereby increasing the load on the Claus process). The Stretford process, often used for Claus tail gas treatment and also for stand-alone sour gas treatment, is based on an aqueous oxidation-reduction reaction. Elemental sulfur is produced from dissolved hydrosulfide (dissociated H_2S) by oxidizing it with sodium vanadate in a buffered solution. The sodium vanadate is regenerated with air and anthraquinone disulfonic acid (ADA). Although the sulfur conversion is high, the build-up of undesirable sulfoxy compounds in the process solution requires neutralization with a base, and the continuous removal of some of the solution as a waste stream. The partly amorphous elemental sulfur produced from the Stretford process is in a colloidal suspension, requiring undependable filter and centrifuge equipment and further processing to produce a marketable sulfur product. All in all, the treatment processes for sour gas streams are complex, expensive to build and operate, oftentimes unreliable, and present waste-disposal problems.

1.3 The UCB Sulfur Recovery Process

The University of California Berkeley Sulfur Recovery Process (UCBSRP) is a new process being developed to recover H_2S from industrial gas streams and convert it to elemental sulfur. The process principle is based on the irreversible liquid-phase

reaction of H_2S and SO_2, the same reaction as in the Claus process, carried out in the liquid phase where it goes to completion at near-ambient temperature. The process is composed of four steps. First, H_2S and, optionally, other gases are absorbed in a polar organic solvent. Second, the dissolved H_2S is converted to elemental sulfur by reacting it with SO_2 dissolved in the same solvent. Third, the elemental sulfur is recovered from the solvent by crystallization; the water and co-absorbed gases are recovered by flashing and stripping. Finally, the SO_2 required in step two is generated by burning one-third of the sulfur produced from the crystallization step. The SO_2 is absorbed in part of the solvent from the stripping step. A schematic diagram of the configuration of the UCBSRP used to remove H_2S selectively from a gas stream is shown in Figure 1.1.

The goals for the process being developed are the following: the capability to reduce the H_2S and SO_2 concentrations in the treated gas streams to less than one ppm, the flexibility to treat a variety of gas streams, and the ability to produce a marketable sulfur product. While accomplishing the above goals, the process must reduce capital and operating costs and minimize waste streams. The process solvent is a polyglycol ether solution that contains a homogeneous catalyst. The criteria in selecting a solvent are that the solvent adequately dissolve H_2S, SO_2, and sulfur, exhibit both low volatility and miscibility with water, and that it be nontoxic and of reasonable cost. A list of some of the solvents that satisfy these criteria is given in Table 1.1. The solubilities of sulfur and selected process gases in these solvents were studied by Sciamanna (1986, 1988). The reaction kinetics were studied in a variety of solvent/catalyst combinations by Neumann (1986). The irreversible liquid-phase reaction is first-order with respect to both reactants and is slightly exothermic. The reaction is catalyzed by heterocyclic aromatic nitrogen compounds. The catalyst must satisfy all but the first criterion used in the selection of the process solvent. A list of some of the catalysts identified by Neumann is shown in Table 1.2. Additional

reaction kinetics and corrosion studies were made by Crean (1987). Absorber tray efficiencies and the reactive absorption of H_2S in an SO_2-laden solvent were investigated by Hix (1989).

The advantages of the UCBSRP over conventional technology include the following: Fewer processing steps provides better operating reliability and lower capital costs. Fewer energy-intensive unit operations reduces operating costs. Process steam, produced from a waste-heat boiler in the sulfur furnace, generally exceeds the needs of the process. Other gas constituents co-absorbed with H_2S from the treated gas may be produced as pure by-products. High H_2S-removal efficiency and wide applicability to sulfur recovery problems are additional advantages. A variety of process applications have been studied, such as the removal of H_2S from gasified coal (Neumann, 1986), the production of high-purity hydrogen from gasified coal (Colson, 1989), an integrated treatment of natural gas (Sciamanna, 1986 & 1988), and the removal of H_2S from the recycle gas for a crude oil residuum hydrotreater (Lynn, *et al.*, 1986).

1.4 Sulfur Crystallization

The elemental sulfur produced by the liquid-phase reaction in the UCBSRP is removed from the process solvent by crystallization. The overriding requirement of the crystallizer is to produce high-quality sulfur crystals with a crystal-size distribution which enables the sulfur solids to be separated from their mother liquor. The amount of downstream sulfur handling is dictated by the quality of the sulfur produced from the crystallizer. To minimize cost and downtime, the downstream sulfur handling must be kept simple, as is obtained with a high-throughput, multiple-wash, pusher-type centrifuge. This equipment can remove the solids from the process solvent, wash the solids with process water to recover residual solvent, and spin-dry the solids nearly free of liquid. Filter operations are not desirable for downstream sulfur handling because of slow filtering rates and laborious filter cake handling.

Another process-dictated condition of the crystallizer is that the vessel should operate at the lowest temperature in the process to eliminate sulfur precipitation elsewhere. However, the temperature of the vessel should be above ambient so that process cooling water, instead of costly refrigeration, may be used to extract the heat of reaction and to cool the solvent. The reaction and crystallization operations are integrated into one vessel to reduce capital costs and to simplify sulfur slurry handling. The liquid-phase reaction of H_2S and SO_2 must be sufficiently fast so that the vessel size is acceptable. The crystallization kinetics must produce the crystal-size distribution desired of the sulfur product. The vessel's internal hydrodynamics and external flow configuration, such as fines reduction and effluent classification, both affect the crystallization kinetics. The sulfur crystal morphology and crystal habit must be consistent and provide rapid solvent removal in a continuous centrifuge. The sulfur purity must be high, with little solvent occlusion, so that further processing is not required and the sulfur product can be burned in the furnace to produce SO_2 or handled immediately for sales.

1.5 Scope of Crystallization Work

The goal of the research program on the UCBSRP is to obtain the physical and chemical data required to design process configurations for different applications and to evaluate the processes' economic potential. The goal of this crystallization work is to determine the process conditions needed to produce sulfur crystals that are viable in an industrial process and attractive as a marketable product. The scope of this study is to determine the dependence of the sulfur crystal-size distribution on the process design parameters. The information required to execute this study were the sulfur and gas solubilities in the process solvent, the reaction kinetics, and the operating conditions of the various process configurations that were investigated. The method of reaching this goal consisted of three steps. First, the solubility of sulfur in the process

solvent was determined for the operating conditions of the crystallizer. Second, the crystallization of sulfur from solution without reaction (thermal crystallization) was studied to determine the crystallization kinetics of the sulfur/solvent system. A crystal-size distribution model was formulated from population-balance theory. Using the model, the dependence of nucleation and growth on the crystallizer operating variables was determined. Third, the effect of the reaction on the crystallization kinetics (reactive crystallization) and the subsequent crystal-size distribution was investigated. The model of thermal crystallization developed in the second step was extended to reactive crystallization in the third step. The extended model was used to predict the crystal-size distribution from operating conditions. The predicted crystal-size distribution was compared to the experimental data.

List of Tables for Chapter 1

1.1 Selected Polyglycol Ether Solvents for UCBSRP

1.2 Selected Catalysts for UCBSRP

List of Figures for Chapter 1

1.1 Process Flow Diagram of UCBSRP -- Highly-Selective H_2S Removal

Table 1.1

Selected Polyglycol Ether Solvents for UCBSRP

Common Name	Compound	Chemical Formula
Diglyme	Di ethylene glycol dimethyl ether	$CH_3 - (OCH_2CH_2)_2 - OCH_3$
Triglyme	Tri ethylene glycol dimethyl ether	$CH_3 - (OCH_2CH_2)_3 - OCH_3$
Tetraglyme	Tetra ethylene glycol dimethyl ether	$CH_3 - (OCH_2CH_2)_4 - OCH_3$
Dowanol DM	Di ethylene glycol methyl ether	$CH_3 - (OCH_2CH_2)_2 - OH$
Dowanol TBH	Tri ethylene glycol n-butyl ether	$C_4H_9 - (OCH_2CH_2)_3 - OH$
Dowanol DPM	Di propylene glycol methyl ether	$CH_3 - (OCH_2CH_2CH_2)_2 - OH$

Table 1.2

Selected Catalysts for UCBSRP

Compound	Structure
3-Pyridyl Carbinol	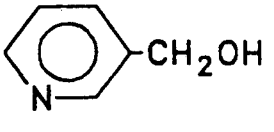
Quinoline	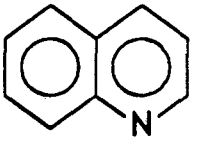
N,N Dimethyl Aniline	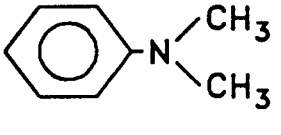

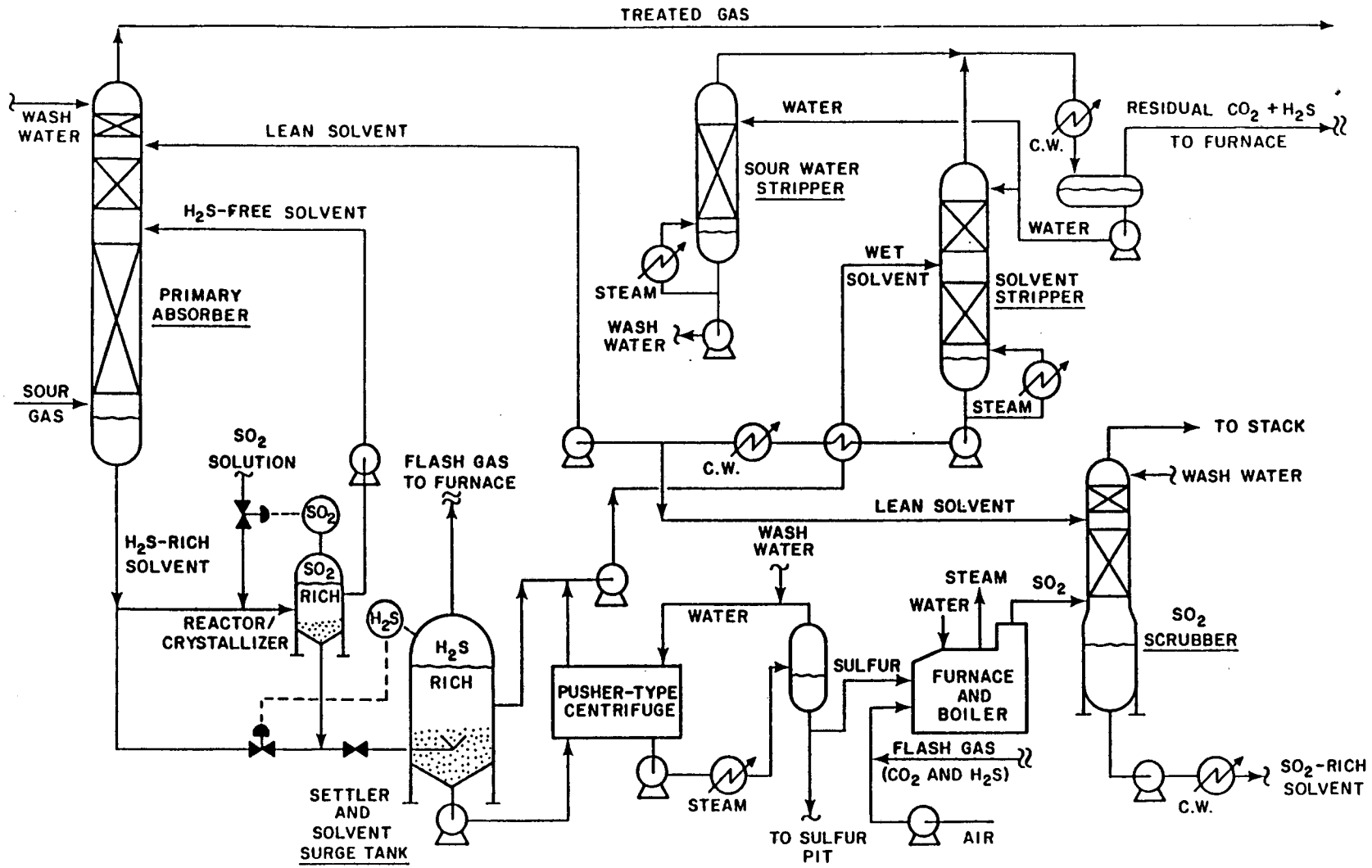

Figure 1.1 Process Flow Diagram of UCBSRP -- Highly-Selective H_2S Removal

CHAPTER 2

LOW TEMPERATURE SULFUR SOLUBILITY

2.1 Preface

Mass-balance calculations must be performed around the unit operations in the University of California Berkeley Sulfur Recovery Process (UCBSRP). Data for the sulfur solubility in the process solvent are required to perform some of these calculations. Sciamanna (1986, 1988) reported the solubility of sulfur in selected polyglycol ether solutions from 160°C (well above the melting point of sulfur) down to approximately 60°C. Since several of the unit operations, including the crystallizer, operate at temperatures below 60°C, sulfur solubility in these solvents at reduced temperatures was needed. From the list of selected solvents in Table 2.1, two were chosen to study sulfur solubility at low temperature. These solvents were triethylene glycol dimethyl ether (Triglyme) and diethylene glycol monomethyl ether (Dowanol DM). These two solvents were chosen because one is a diether and the other a monoether and because both were expected to give results representative of their respective type of ether solvent. In addition to determining the temperature dependence of sulfur solubility in these solvents, the effect of water concentration in the solvent on sulfur solubility was also investigated.

2.2 Solid-Liquid Equilibrium Theory

The classical thermodynamic framework used to describe the solubility of solids in liquids is well understood. An excellent development of this theory is discussed by Prausnitz (1986). This theoretical framework yields the expression that was used to correlate the data from this study.

2.2.1 Solid Solubility in Pure Solvents

The solid-liquid equilibrium expression is formulated from the following universal

thermodynamic relation: the chemical potential of the pure solid must equal that of the solute in the liquid solution. From this relation, the saturation concentration of the solid solute in the liquid solvent is mathematically expressed as:

$$\ln(x_s\gamma_s) = -\frac{\Delta s_f}{R}\left(\frac{T_m}{T_s} - 1\right) + \frac{\Delta C_p}{R}\left(\frac{T_m}{T_s} - 1\right) - \frac{\Delta C_p}{R}\ln\left(\frac{T_m}{T_s}\right) \tag{2-1}$$

where: R = universal gas constant (J/mol-K)

T_m = melting temperature of the solute (K)

T_s = temperature of the saturated solute/solvent system (K)

x_s = mole fraction of the solute in solution

γ_s = activity coefficient of the solute in solution

Δs_f = entropy of fusion of the solute @ T_m [= $\Delta h_f/T_m$] (J/mol-K)

ΔC_p = heat-capacity difference [= C_p(*liquid*) - C_p(*solid*)] (J/mol-K)

This expression is the result of two simplifications. First, for most solutes at near-ambient pressure, there is little difference between the triple-point temperature and the melting temperature. Correspondingly, there is little difference between the heat of fusion (Δh_f) at the triple-point temperature and the heat of fusion at the melting temperature. The melting-point variables are therefore substituted for the triple-point variables to produce Equation (2-1). Second, the heat-capacity difference (the difference between the heat capacity of the hypothetical liquid solute at the saturated temperature and the heat capacity of the solid solute at the melting temperature) is assumed constant over the temperature range: T_m to T_s.

Two additional assumptions were made which enabled use of Equation (2-1) for this study. First, the sulfur/solvent solutions were assumed to be non-ideal ($\gamma_s \neq 1$). Furthermore, since all of the solutions are relatively dilute, the activity coefficient was assumed to be independent of both temperature and solute concentration ($\gamma_s \neq f(T,x_s)$). No attempt was made to predict the value of the solute activity coefficient. Second, the dependence of solute weight percent on solute mole fraction was assumed linear.

This is a good assumption when the dissolved solute concentrations are very low, as in the sulfur/solvent system studied in this work. This assumption enabled comparison of sulfur solubility data from several solvents that have different molecular weights. The solute weight percent was substituted for its mole fraction and the terms in Equation (2-1) were consolidated to express the dependence of sulfur solubility on inverse saturation temperature (T_s), normalized by the sulfur melting temperature (T_m). The following expression was used to correlate the experimental data:

$$\ln w_s = A\frac{T_m}{T_s} + B \ln\left(\frac{T_m}{T_s}\right) + C \tag{2-2}$$

where w_s is the solute weight percent and A, B, and C are fitted constants. This form is suggested by Broul, *et al.* (1984) for characterizing the solubility of inorganic solutes in aqueous solutions.

2.2.2 Solid Solubility Near the Solid Melting Temperature

Further simplification of Equation (2-1) can be made when the saturation temperature (T_s) is close to the solute melting temperature (T_m). On the right-hand side of Equation (2-1), the heat capacity terms tend to cancel each other and the entropy-of-fusion term becomes dominant. The ΔC_p terms are thus neglected and the resulting expression is:

$$\ln(x_s\gamma_s) = -\frac{\Delta s_f}{R}\left(\frac{T_m}{T_s} - 1\right) \tag{2-3}$$

Again, the solute weight percent was substituted for its mole fraction and the consolidation of the terms in Equation (2-3) was made to express the dependence of sulfur solubility on inverse saturation temperature, normalized by the sulfur melting temperature. The experimental data near the solute melting temperature were correlated using the following expression:

$$\ln w_s = E\frac{T_m}{T_s} + F \tag{2-4}$$

where E and F are fitted constants. No attempt was made to predict the values of the

constants A through F *a priori*; these constants were used soley to correlate the experimental data.

2.2.3 Effect of Temperature on Solid Solubility

General trends of solute solubility may be elucidated by determining the dependence of solute concentration on saturation temperature. The first derivative of Equation (2-1) with respect to inverse saturation temperature is:

$$\frac{d\ \ln(x_s\gamma_s)}{d\ (T_m/T)} = -\frac{\Delta s_f}{R} + \frac{\Delta C_p}{R}\ (1 - T/T_m) \tag{2-5}$$

At temperatures near the solute melting temperature, the heat capacity term in Equation (2-5) is negligible. As a result, the solubility dependence on inverse temperature is linear, as exemplified in Equation (2-3). A semi-log plot of solute concentration versus inverse temperature has a constant, negative slope. For temperatures well below the melting point of the solute, the heat capacity term has a significant contribution to the right-hand side of Equation (2-5). The slope of the solubility curve may be described qualitatively using the following arguments. The entropy of fusion of the solute at its melting temperature is constant and always positive. The difference in heat capacity between the hypothetical liquid at T and that of the solid at T_m (ΔC_p) is not constant with respect to temperature but is also a positive value. From Equation (2-5), the slope of a semi-log plot of solute concentration versus inverse temperature increases monotonically from a negative value as the temperature is decreased (as T_m/T is increased). This is observed from the second derivative of Equation (2-1):

$$\frac{d^2\ \ln(x_s\gamma_s)}{d\ (T_m/T)^2} = \frac{\Delta C_p}{R}\ T^2 \tag{2-6}$$

The right-hand side of Equation (2-6) is always positive and the curve of solute concentration versus inverse temperature is concave upward. This information is of practical importance when fitting Equations (2-2) and (2-4) to experimental data,

which may have significant scatter so that a statistical fit gives erroneous trends.

2.3 Experimental Apparatus

The experimental apparatus used to study sulfur solubility in the polyglycol ether solvents was a simple temperature-controlled equilibrium cell. A schematic diagram of the apparatus is shown in Figure 2.1. The cell was constructed with a 50-milliliter test tube, partially immersed in an oil bath. The sulfur/solvent sample was held in the test tube and agitated by a small magnetic stir bar. A mercury thermometer with graduations of 0.2^{o}C was immersed in the cell sample to monitor the cell's temperature. The oil bath was composed of 800 milliliters of clear mineral oil. The bath was contained in a one-liter beaker and agitated using a large magnetic stir bar. The contents of the oil bath were placed on a modified hot plate/magnetic stirrer. For temperatures above ambient, the hot plate was controlled by a mercury thermoregulator switch which was immersed in the oil bath. For temperatures below ambient, the oil bath was immersed in an ice bath and placed on the hot plate/magnetic stirrer to stir the oil bath and equilibrium cell sample. A Hewlett-Packard 8452A UV-VIS spectrophotometer (190 - 820 nm wavelength range) was used to measure the absorbance of equilibrium cell samples and determine the sulfur solubility.

2.4 Experimental Method

The solubility of sulfur in the polyglycol ether solvents is quite low compared to its solubility in solvents in which it dissolves readily, such as carbon disulfide. At elevated temperatures, the sulfur solubility in the process solvents may be determined by watching the solute dissolve with the un-aided eye and noting the saturation temperature. Sciamanna (1986, 1988) used this method of sulfur solubility measurement. However, at low temperatures the solubility of sulfur in the solvents is so low that visually determining the saturation temperature is difficult. A

spectrophotometer was used to determine the sulfur solubility in this study because the spectrophotometer is well suited for this range of solubility and because the dissolved sulfur absorbs light (forms a yellow-colored solution) in the UV-VIS wavelength range.

The solubility of sulfur is dependent on the water concentration in the solvent. The Triglyme (SpecialtyChem Products Ansul E-161) and Dowanol DM (Dow Chemical, U.S.A.) solvents are hygroscopic and absorb water during shipping and handling. Both solvents were therefore pretreated before using them in the equilibrium cell experiments. The two solvents were heated to approximately 100°C and sparged with dry nitrogen for at least one hour to rid the solvents of water. The clean solvents were subsequently bottled and their exposure to the atmosphere minimized.

With the spectrophotometer, the relationship of solution absorbance versus sulfur concentration in each solvent was determined. This was accomplished by making sulfur-solvent solutions of known sulfur concentration and measuring the absorbance in the spectrophotometer. The calibration was made for absorbance values that were 75 to 90 percent of the maximum of the photometric range of the spectrophotometer. At least ten repetitions or scans were made of each sample. When measuring the absorbance of sulfur in Triglyme, the absorbance was noted for the maximum of each spectrum; the maximum ranged from 316 to 336 nm. For sulfur in Dowanol DM, the absorbance was recorded at 300 nm (near the maximum absorbance) from each spectrum. Calibration curves were then constructed relating the absorbance to the concentration of sulfur in each solvent.

The equilibrium cell was filled with approximately 15 grams of solvent and no more than 2.0 grams of sulfur (Mallinckrodt Sublimed Sulfur). The sublimed sulfur powder, which exists as a monoclinic sulfur allotrope, was recrystallized from the solvent in which the solubility study was made. This was done to produce rhombic

sulfur crystals, which are more easily dissolved in the solvent than the monoclinic form. Excess solid sulfur was always present in the cell to provide sufficient sulfur for the solvent to dissolve. The solution was heated to just below the temperature of interest. Precautions were taken to always approach the saturation temperature of interest by increasing the temperature of the cell, instead of allowing the temperature to fall from some higher value. This was done so that supersaturation of the solution was avoided and subsequent extraneous solubility values observed. After the cell contents were given time to reach equilibrium, the stirring was stopped and the excess sulfur solids allowed to settle. A small portion of the solution (less than five milliliters) was removed for analysis in the spectrophotometer. At least three spectrophotometer scans of each sample were made when measuring the absorbance. The techniques used in the calibration procedure to determine the absorbance of the calibration standards were used to determine the absorbance of the equilibrium samples. For the more concentrated samples, where the absorbance of an undiluted sample exceeded the range of absorbance values used in the calibration, the sample was diluted with a known amount of clean solvent. The diluted sample was analyzed in the spectrophotometer and the sample's actual sulfur concentration calculated from the absorbance and amount of diluent added.

2.5 Sulfur Solubility in Triglyme and Dowanol DM

The experimental data from this study were correlated by applying the solid-liquid equilibrium theory discussed in Section 2.2. The data from this study were then compared to the data of Sciamanna (1986, 1988) and combined with them to elucidate overall sulfur solubility trends in the process solvents. The data from this study and the Sciamanna data used in this study are tabulated in Appendix A. Throughout this study, the sulfur was assumed to be in the cyclo-octa (S_8 ring) orthorhombic allotropic form.

2.5.1 Sulfur Solubility in Triglyme

The experimental data from this work were first plotted in the form suggested by Equation (2-3). This enabled direct comparison with the Sciamanna data. The Sciamanna data of interest to this work were those taken at temperatures below the melting point of sulfur. A least-squares regression of each set of data, Sciamanna's and those from this work, was used to determine the constants of Equation (2-4). Figure 2.2 shows both sets of data with their respective fitted lines. Obviously, the fitted lines are only applicable to the temperature range of each data set. The slope of each line is described by Equation (2-5), where the heat-capacity difference term has a significant contribution for the low-temperature fitted line. The low-temperature data were then plotted as $\ln(w_s)$ versus T_m/T to compare with Equation (2-1). A regression of the data from this study only was used to determine the constants in Equation (2-2). The curve fitted to the data exhibited the concave-upward curvature described by Equation (2-6). Although the fitted curve predicted the high-temperature data well, the extrapolation from the low-temperature data is large. Therefore, the low-temperature and high-temperature data were combined to determine the constants in Equation (2-2) for the entire temperature range. Figure 2.3 shows the fitted curve in the form of Equation (2-2) for both sets of data. The constants for Equation (2-2) are listed in Table 2.2. The fitted curve in the form of Equation (2-2) exhibits the concave-upward curvature and compares well with both the data from Sciamanna and the data from this study.

2.5.2 Sulfur Solubility in Dowanol DM

The method of data analysis and comparison in studying the solubility of sulfur in Dowanol DM was the same as that in Triglyme. Figure 2.4 shows the results of applying Equation (2-4) to each set of data: the low-temperature data taken in this work and the high-temperature data from Sciamanna. As in the Triglyme study, the two data sets could not be fit by a single line. The curve in the form of Equation (2-

2) fitted to the low-temperature data only did not agree with the temperature-dependence expressions derived in Section 2.2.3. This disagreement is a result of the effect of the scatter of the low-temperature experimental data in a small temperature range on the statistical regression analysis. When the regression of both sets of data in the form of Equation (2-2) was made, the data from a much larger temperature range forced the fitted curve to agree with the concave-upward expression of Equation (2-6). The data and the plot of Equation (2-2) are shown in Figure 2.5. Table 2.2 lists the constants generated from both sets of data for Equation (2-2). The fitted curve in Figure 2.5 compares very well to the experimental data over the entire temperature range.

2.5.3 Results and Discussion

The application of Equation (2-1) to the experimental data from this work and from Sciamanna gave an expression that can be used over the entire temperature range of the data. This application is superior to using separate versions of Equation (2-3) for each temperature range where data were taken; such a procedure is not convenient when calculating sulfur solubility for process conditions. Sciamanna reported that the high-temperature data followed the trend described by Equation (2-3), where the saturation temperature was removed from the sulfur melting temperature (386 K) by a maximum of 50 K (13 % reduction in temperature from T_m). The low-temperature data were removed from the sulfur melting temperature by a maximum of 111 K or a 29 percent reduction in temperature from T_m. At temperatures far removed from the solute melting temperature, the heat-capacity difference terms in Equation (2-1) contribute to the solute solubility . This phenomenon is illustrated by the low-temperature data shown above. When the regression of both sets of data in the form of Equation (2-2) was made, the temperature dependence of the resulting fitted curves was in agreement with the derivative expressions produced from the theoretical model. The use of Equation (2-2) with constants fitted to the data from this work and from

Sciamanna allows interpolation between the two data sets to be made.

2.6 Effect of Water on Sulfur Solubility

As illustrated in a previous investigation (Sciamanna, 1986 & 1988), the solubility of sulfur is dependent on water concentration in the solvents of interest. The theoretical model developed in Section 2.2 was modified to quantify the water effect on sulfur solubility. The dependence of sulfur solubility on water concentration was assumed to be exponential because of the trends shown by Sciamanna. Equation (2-2) was therefore modified by simply adding a linear water concentration term:

$$\ln w_s = A\frac{T_m}{T_s} + B \ln\left(\frac{T_m}{T_s}\right) + C + D\, w_w \qquad (2\text{-}7)$$

where w_w is the weight percent of water in the solvent on a sulfur-free basis. The modification has only an empirical basis, and was implemented only to correlate the data.

2.6.1 Effect of Water on Sulfur Solubility in Triglyme

The data used to quantify the water effect in Triglyme were taken from Sciamanna (1986, 1988). The only solubility data available where water was present in any of the diether solvents were for Diglyme with five weight percent water. An assumption was made to enable the comparison of sulfur solubility in Triglyme to that in Diglyme. As shown by Sciamanna, the solubility of sulfur in the diether solvents on a weight basis is approximately invariant for the three solvents studied: Diglyme, Triglyme, and Tetraglyme. This is illustrated in Figure 2.6. The sulfur solubility in Triglyme containing zero and five weight percent water was therefore assumed equal to the sulfur solubility in Diglyme with the same water concentrations. Although equating the sulfur solubility in Diglyme with that in Triglyme is not entirely correct, this assumption provides a first approximation for the effect of water on sulfur solubility in Triglyme. To determine the value of the coefficient D in Equation (2-7), the coefficients A, B, and C were held constant at values found in Section 2.5.1. The

value of D was found by a least-squares regression of the high-temperature data only. The water-free solubility data for Diglyme, Triglyme, and Tetraglyme were used in the analysis to smooth the data. The high-temperature data, the resulting curves produced by Equation (2-7), and the low-temperature data are shown in Figure 2.7. The value of D for sulfur solubility in Triglyme is listed in Table 2.2.

2.6.2 Effect of Water on Sulfur Solubility in Dowanol DM

High-temperature data from Sciamanna were used to determine the effect of water concentration in Dowanol DM on sulfur solubility. Sulfur solubility data were available at 0.0, 2.5, and 5.0 weight percent water in Dowanol DM. The method of determining the value of D in Equation (2-7) was the same as the determination of D for Triglyme: the coefficients A, B, and C were held constant at the values found in Section 2.5.2 and the value of D determined by a least-squares regression. The high-temperature data from Sciamanna, the resulting curves produced by Equation (2-7), and the low-temperature data from this work are shown in Figure 2.8. The value of D for sulfur solubility in Dowanol DM is listed in Table 2.2.

2.7 Summary

The solubilities of sulfur in both Triglyme and Dowanol DM were correlated using a model derived from a theoretical framework. The model is applicable to a temperature range of 8° to $113^{o}C$ (the melting point of sulfur) and a water concentration range of zero to five weight percent for each solvent. The effect of water was characterized by modifying the model with an additional term. The semi-theoretical model is applicable over the entire range of process conditions anticipated in the UCBSRP, all of which are below the sulfur melting temperature.

Comparison of the sulfur solubility in Triglyme and that in Dowanol DM shows that Triglyme dissolves more sulfur than Dowanol DM. Refer to Figure 2.9 for a comparison of all of the data used in this study. The ability of Triglyme to hold more

sulfur in solution than Dowanol DM may affect the selection of a process solvent for some operating conditions.

List of Tables for Chapter 2

2.1 Sulfur Solubility Study Compounds

2.2 Sulfur Solubility in Polyglycol Ethers

List of Figures for Chapter 2

2.1 Sulfur Solubility Apparatus

2.2 Sulfur Solubility in Triglyme with Equation (2-4)

2.3 Sulfur Solubility in Triglyme with Equation (2-2)

2.4 Sulfur Solubility in Dowanol DM with Equation (2-4)

2.5 Sulfur Solubility in Dowanol DM with Equation (2-2)

2.6 Effect of Water on Sulfur Solubility in Diethers

2.7 Estimated Effect of Water on Sulfur Solubility in Triglyme

2.8 Effect of Water on Sulfur Solubility in Dowanol DM

2.9 Effect of Water on Sulfur Solubility in Polyglycol Ether Solvents

Table 2.1

Sulfur Solubility Study Compounds

Common Name	Compound	MW[1]	BP(°C)[2]
Diglyme	Di ethylene glycol dimethyl ether	134.17	162
Triglyme	Tri ethylene glycol dimethyl ether	178.22	216
Tetraglyme	Tetra ethylene glycol dimethyl ether	222.28	275
Dowanol DM	Di ethylene glycol methyl ether	120.15	194

Common Name	Compound	MW[1]	MP(°C)[3]
Sulfur	Rhombic (α) S_8	256.53	113

[1]MW = Molecular Weight
[2]BP = Boiling Point @ 1 atm.
[3]MP = Melting Point @ 1 atm.

Table 2.2

Sulfur Solubility in Polyglycol Ethers

	A	B	C	D
Triglyme	14.92	-29.82	-13.13	-0.07544
Dowanol DM	12.85	-26.85	-11.89	-0.08889

$$\ln w_s = A\frac{T_m}{T_s} + B \ln\left(\frac{T_m}{T_s}\right) + C + D\, w_w$$

where:
T_s = saturation temperature in Kelvin
T_m = melting temperature of sulfur (386 K)
w_s = weight percent sulfur in solvent (water-free basis)
w_w = weight percent water in solvent (sulfur-free basis)

Figure 2.1
Sulfur Solubility Apparatus

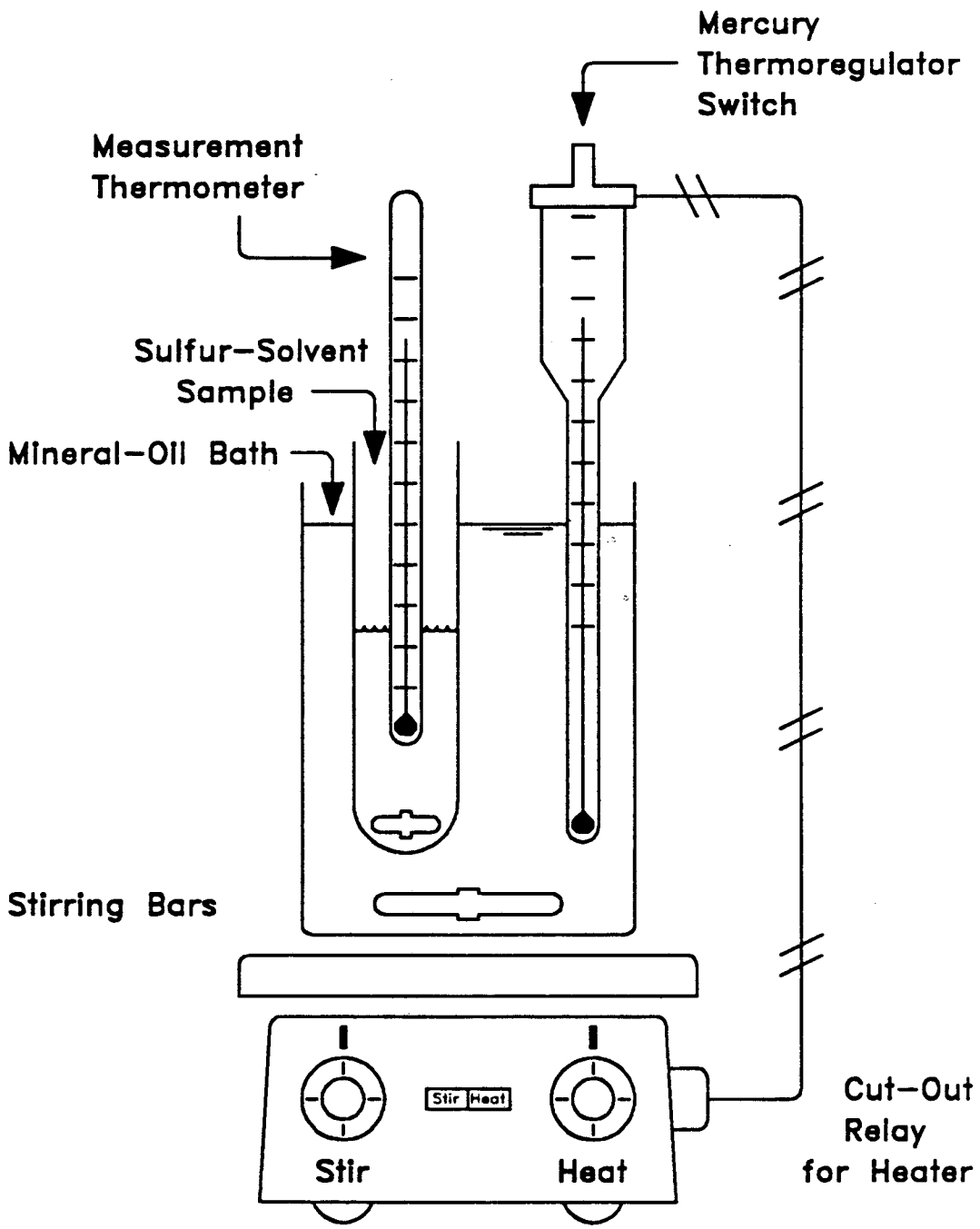

Figure 2.2

Sulfur Solubility in Triglyme

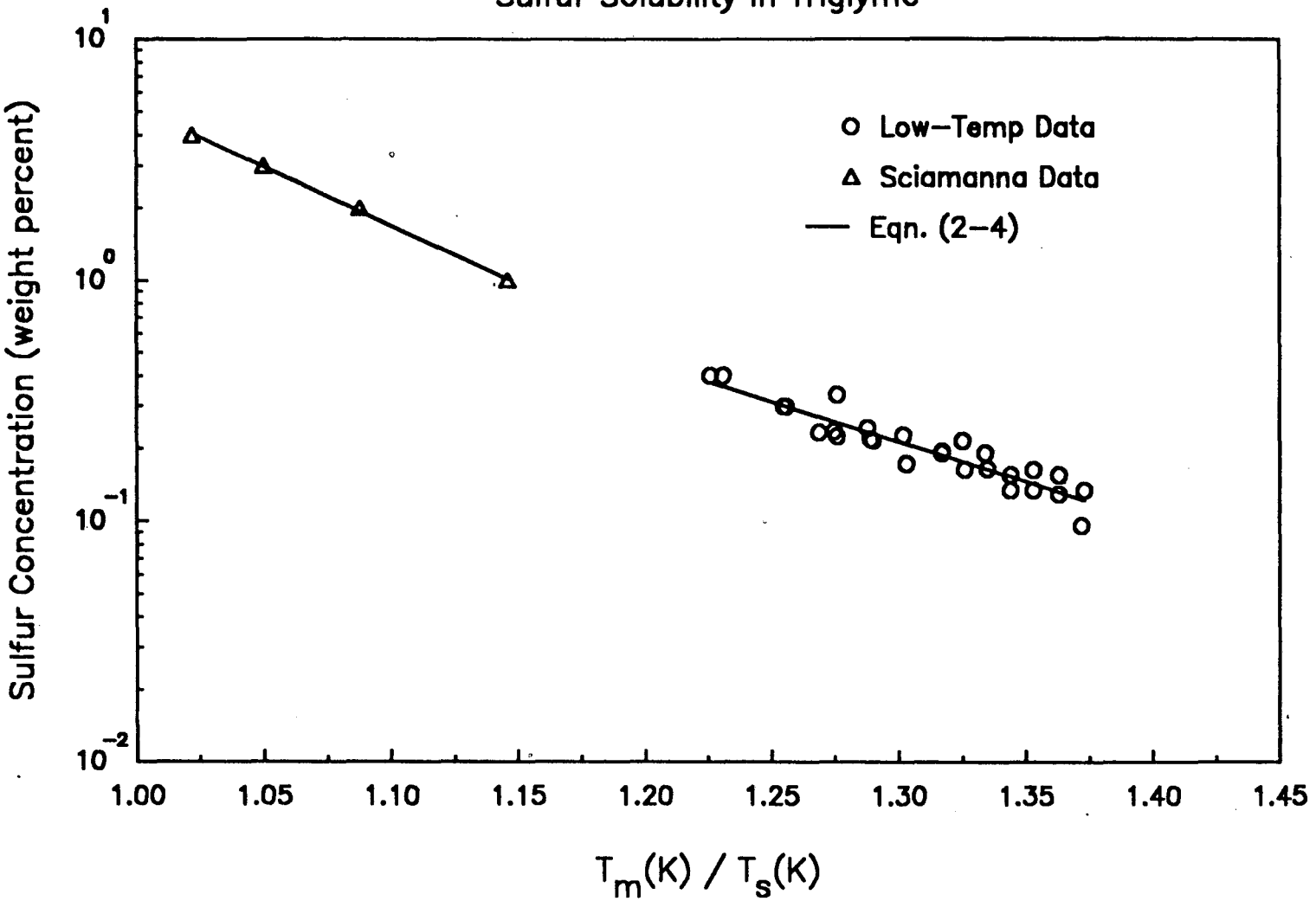

Figure 2.3

Sulfur Solubility in Triglyme

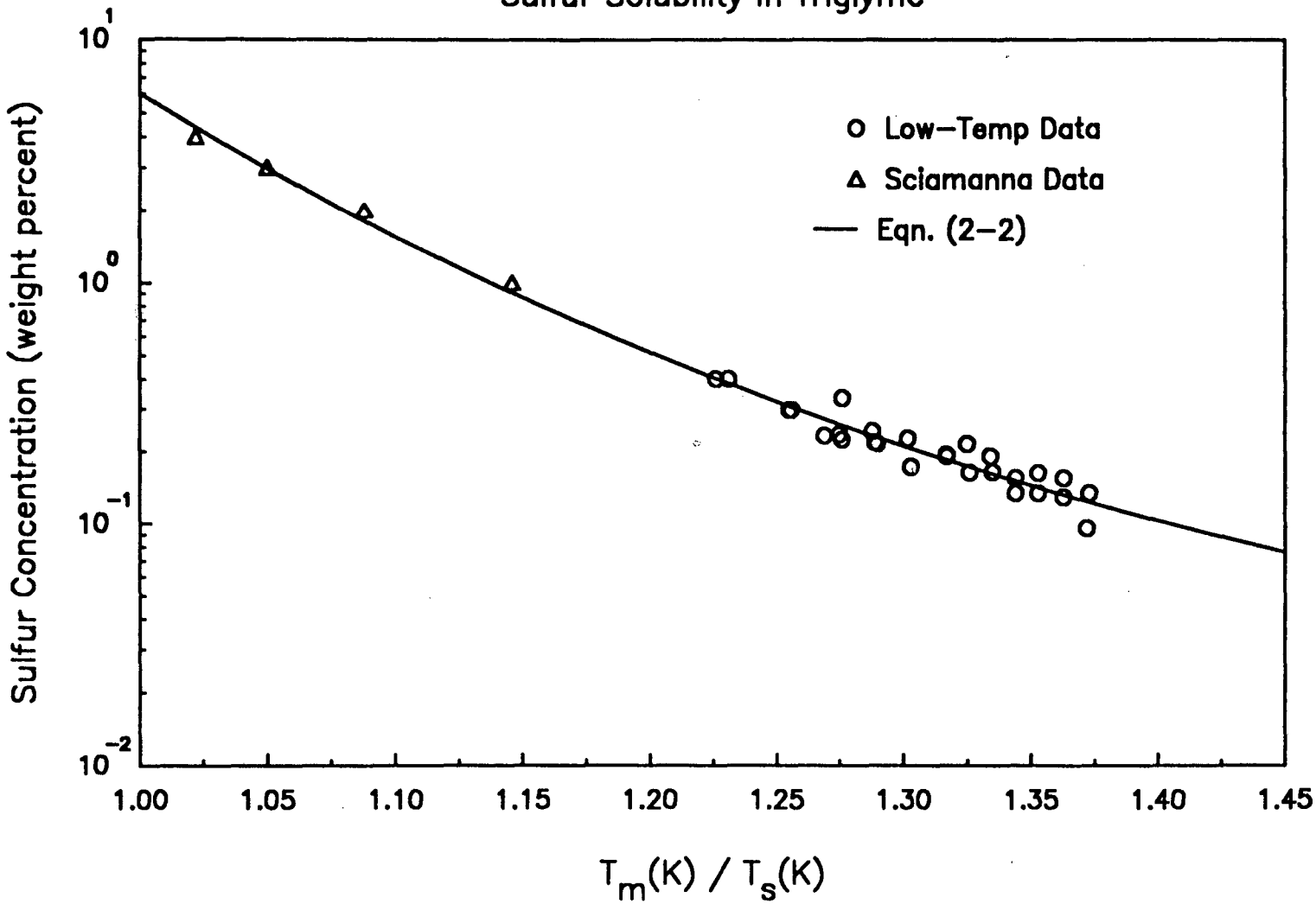

Figure 2.4

Sulfur Solubility in Dowanol DM

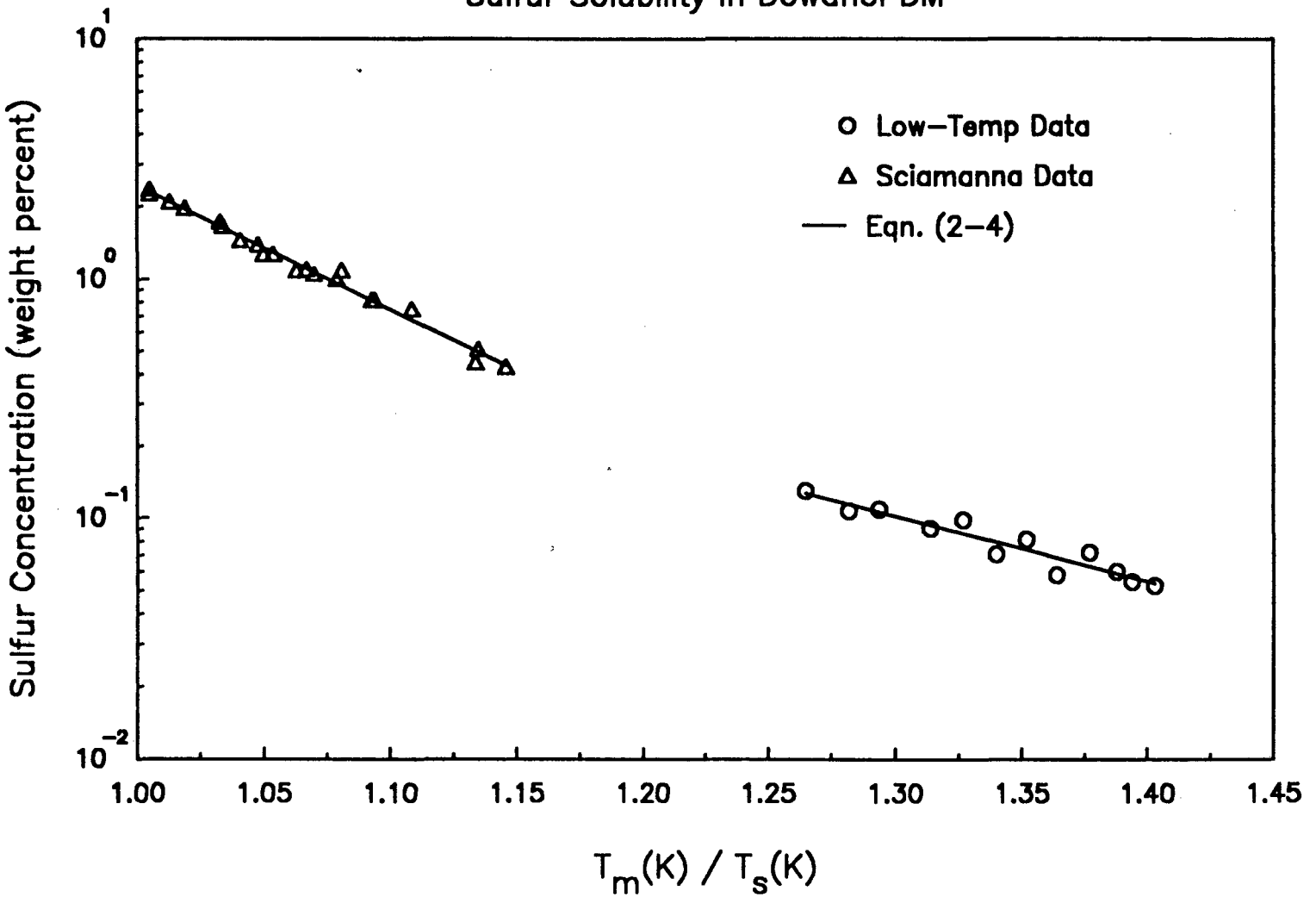

Figure 2.5

Sulfur Solubility in Dowanol DM

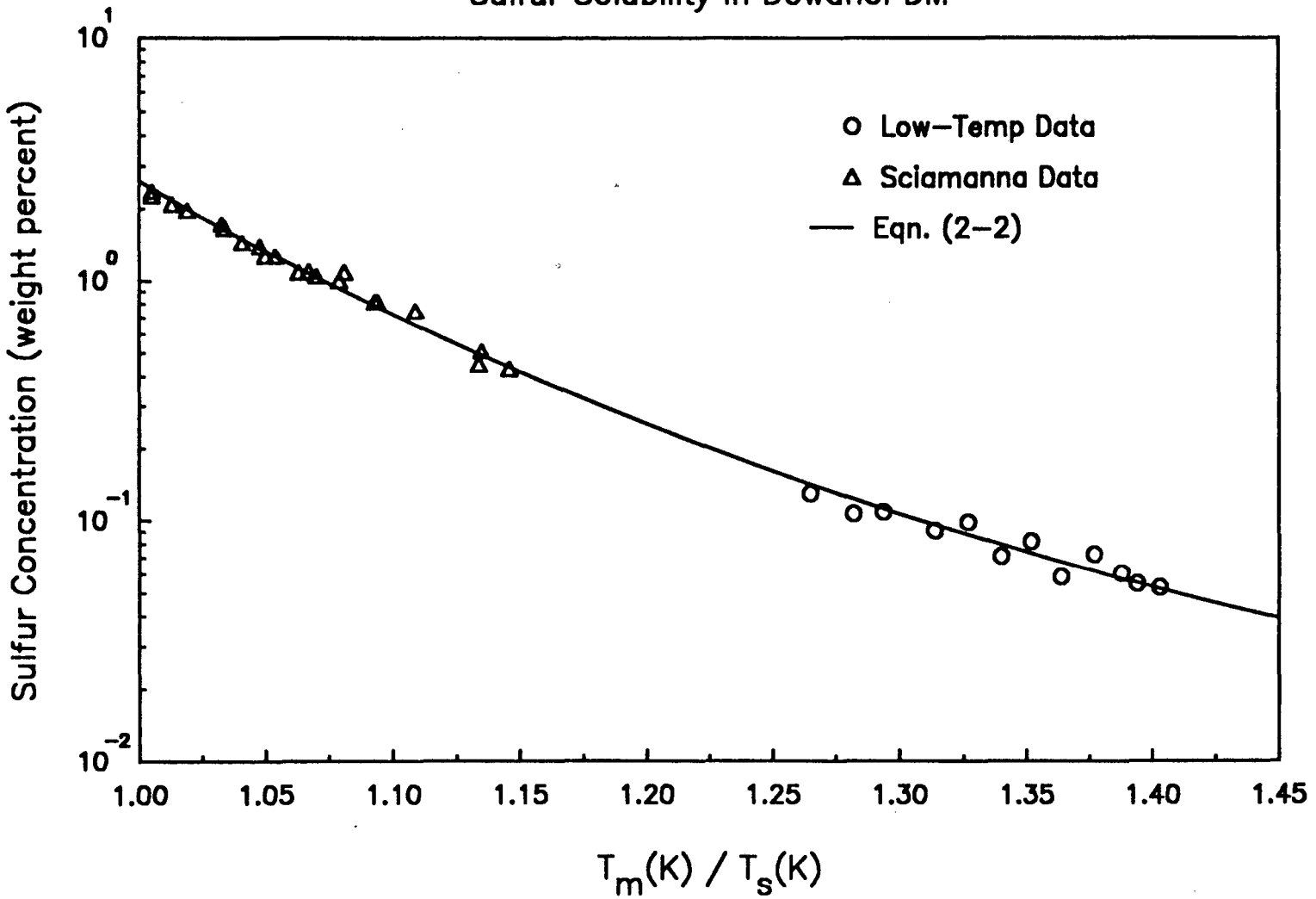

Figure 2.6

Effect of Water on Sulfur Solubility in Diethers

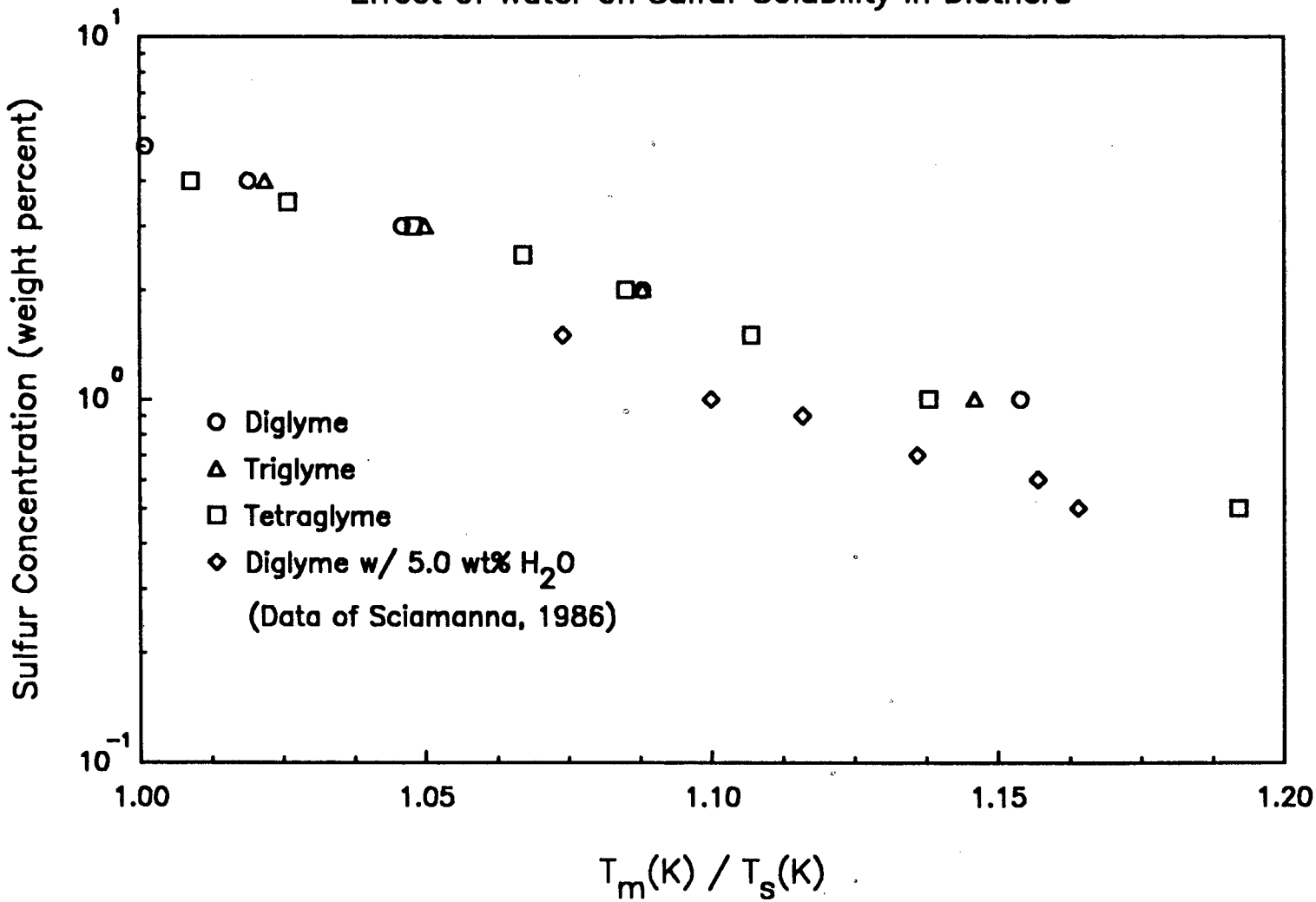

Figure 2.7

Estimated Effect of Water on Sulfur Solubility in Triglyme

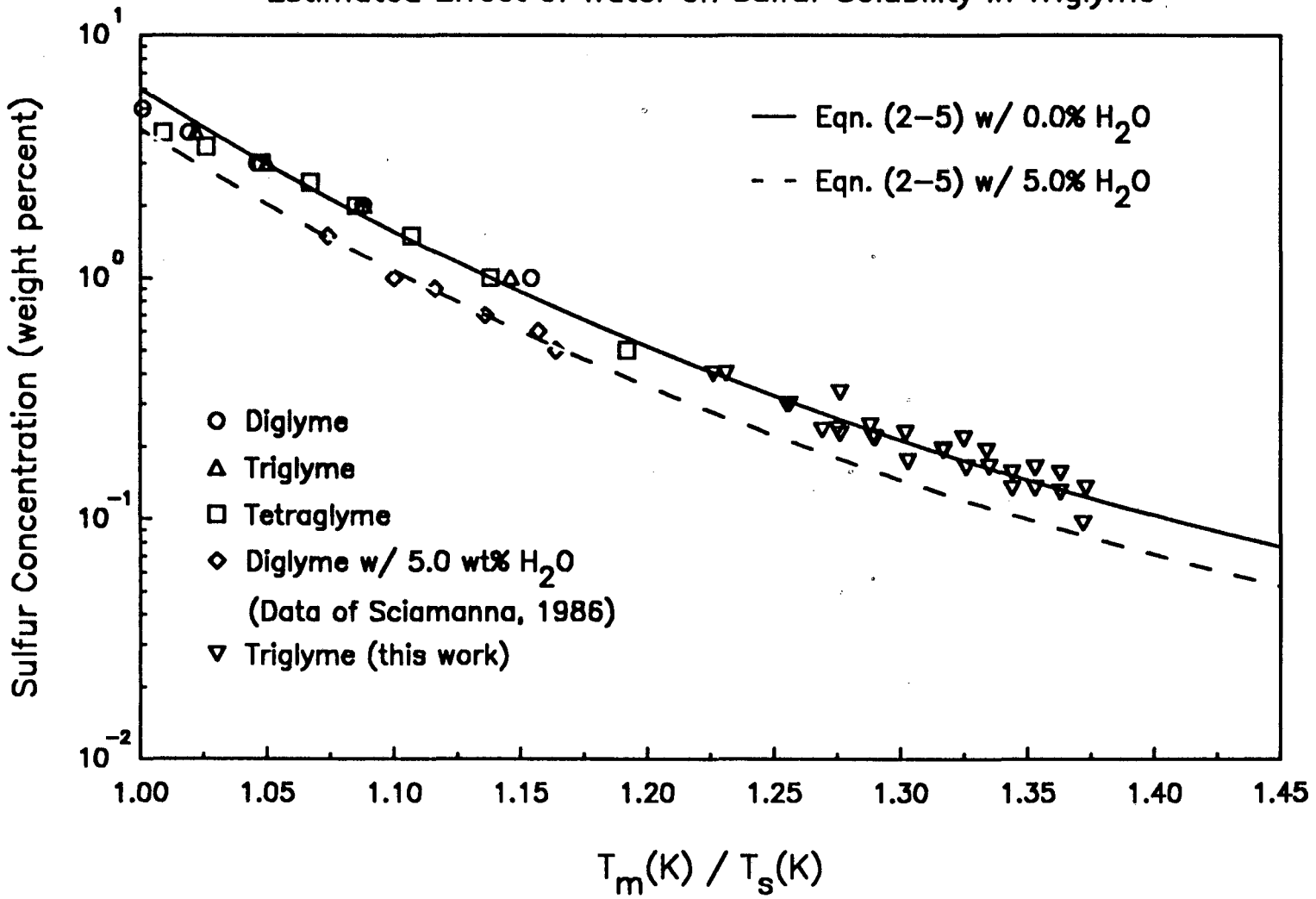

Figure 2.8

Effect of Water on Sulfur Solubility in Dowanol DM

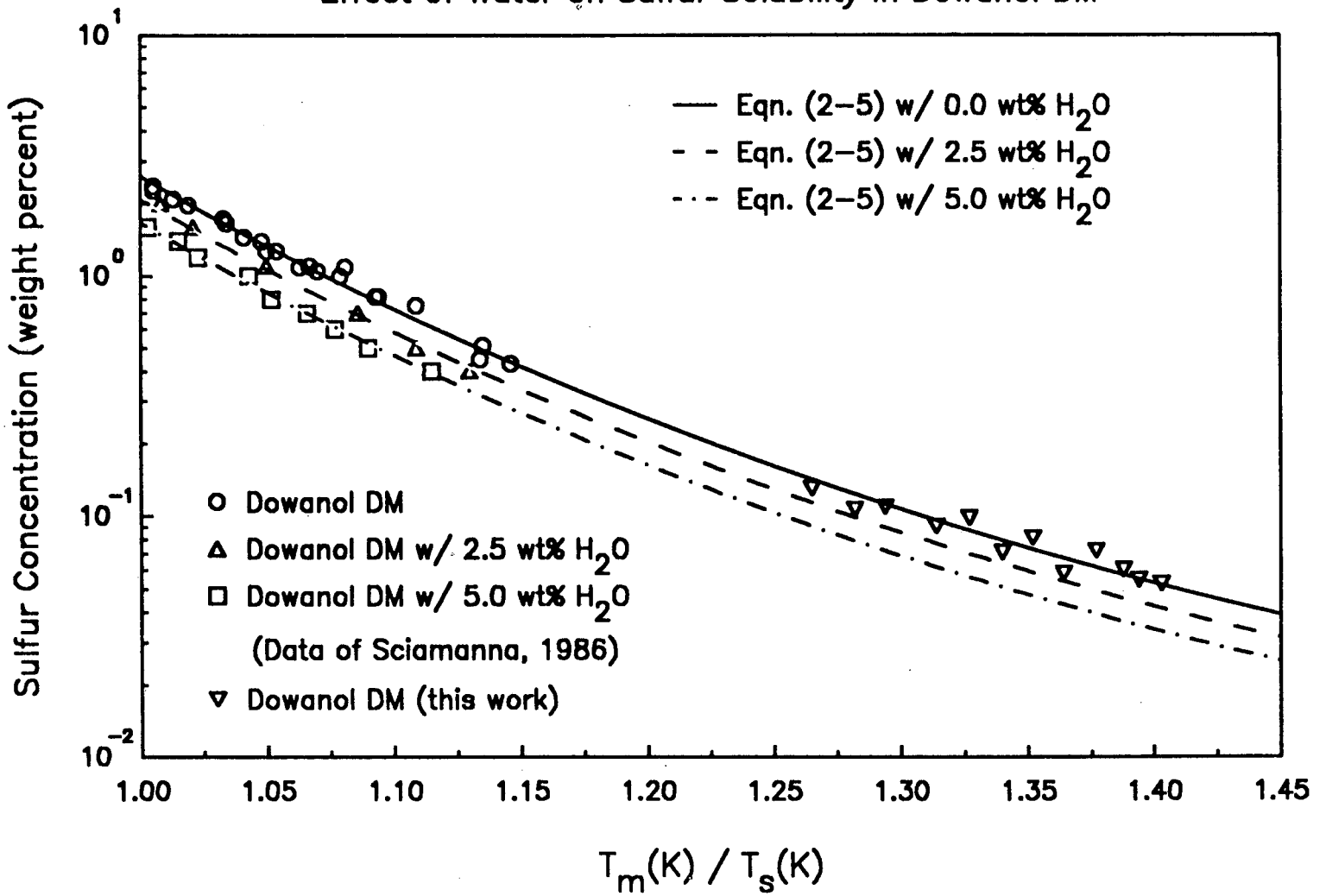

Figure 2.9

Effect of Water on Sulfur Solubility in Polyglycol Ether Solvents

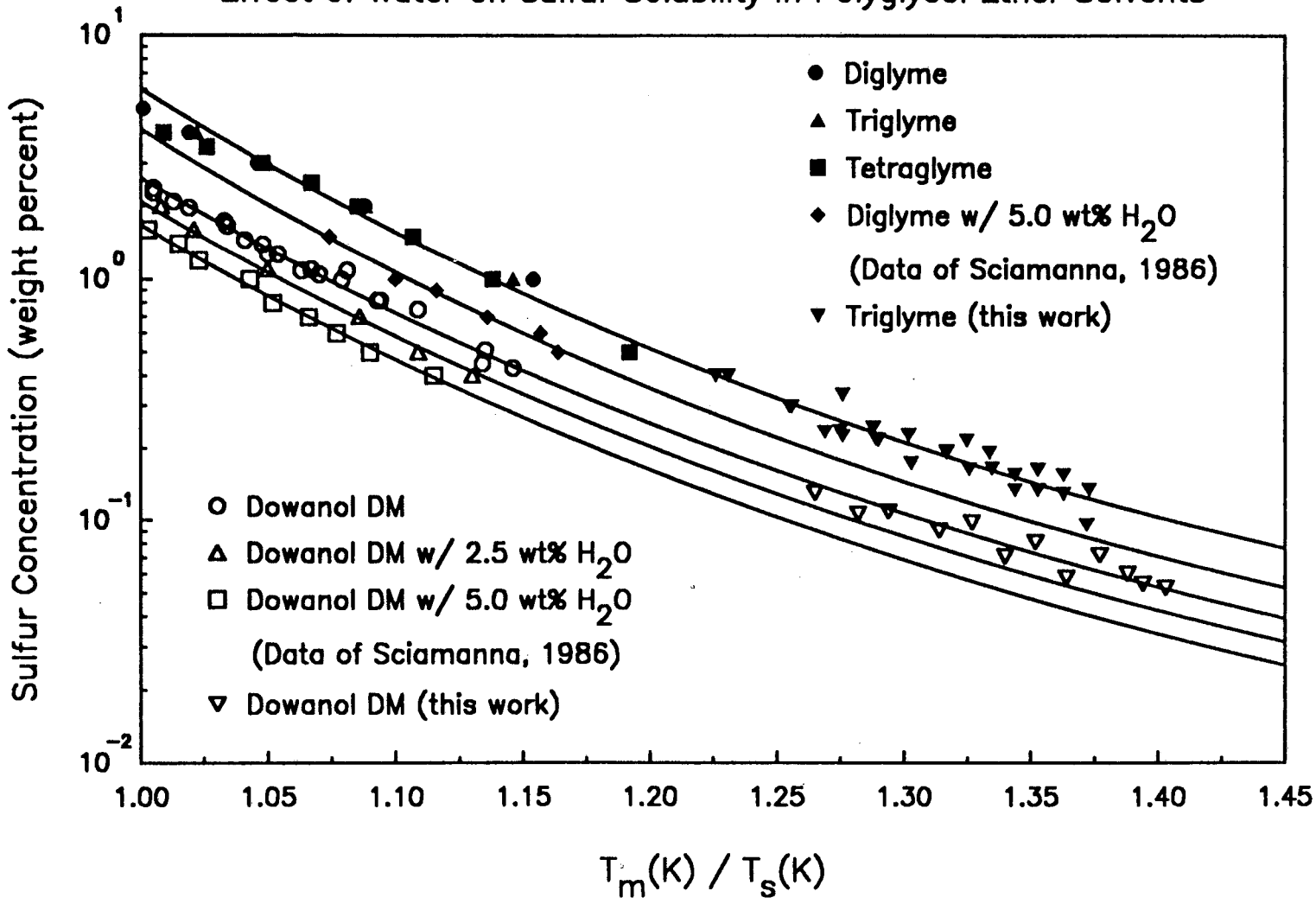

CHAPTER 3

THERMAL CRYSTALLIZATION

3.1 Preface

The crystallization of elemental sulfur is a unit operation in the University of California Berkeley Sulfur Recovery Process (UCBSRP). The sulfur crystals are produced from the process solvent by completing the liquid-phase reaction between H_2S and SO_2 and by reducing the temperature of the bulk solvent. Before an investigation of the reactive crystallization was made, the thermal crystallization of sulfur from solution was studied. In the simpler thermal crystallization case, the dependence of the sulfur crystal-size distribution on the operating conditions in the crystallizer was of primary interest. This information was then used in studying the more complex reactive crystallization case. Also of interest were the purity and morphology of the sulfur crystals produced in the experimental crystallizer. The thermal crystallization study was composed of two programs. First, a theoretical program was performed to develop a crystal-size distribution model which related the crystallization kinetics of the sulfur/solvent system to the data from laboratory crystallization experiments. The model was then formulated as a predictive tool to be used in the design and scale-up of an industrial crystallizer for the UCBSRP. A general crystallizer design equation was formulated that will be applicable not only to the sulfur/solvent system studied in this work, but to many crystallization systems. Second, a laboratory-scale experimental program was executed to study the crystallization kinetics of the sulfur/solvent system in a continuous, back-mixed crystallizer. The dependence of the kinetics on the crystallizer operating parameters was determined. The purity and morphology of the sulfur crystals were also determined. As an extension of the experimental work, a fluidized-bed arrangement was used in an attempt to produce only large, mono-sized sulfur crystals.

The crystallization of elemental sulfur from polyglycol ether solutions poses an interesting problem. The majority of the crystallization operations in industry produce inorganic salts from aqueous solutions, whereas the remainder of the operations produce organic solids from organic solutions. The solid/liquid system in this study is somewhat different in that an inorganic compound (but not an ionic salt) is crystallized from an organic solvent. Several studies have indicated that sulfur crystals with defined morphology may be produced from organic solutions with satisfactory results (Akselrub *et al.*, 1976; Kuster, 1967; Nuffield, 1972). Produced from the crystallizer in the UCBSRP, a crystalline sulfur product is preferred because the crystals produced from a typical crystallization operation are very pure (99+ percent) for a single-stage operation. In addition, producing a product with crystalline morphology enables the growth of large crystals because additional solute may be deposited onto the existing structure at the crystal surface. These large crystals are also preferred because the crystals are easily separated from the mother liquor. This separability contrasts with that of the partly-amorphous sulfur precipitated from aqueous solutions, such as that produced from the Stretford process, where the sulfur solids are small and "sticky". As a result, the sulfur is difficult to recover from the Stretford solution. The fundamental framework of the theoretical crystallization model, used in this study to characterize the processes existing in the crystallization system (as opposed to a precipitation system), is well known and is discussed below.

3.2 Crystal-Size Distribution Theory

Two crystal-size distribution models were developed for a continuous, well-stirred crystallizer. The first is an ideal crystallizer model. The second is an extension of the first model which simulates the physical phenomena observed in the experimental crystallizer. A design equation for each model was derived from a population balance, a mass balance, and a crystallization kinetics expression. The development of the population balance and its use in crystallization systems is discussed in Randolph and

Larson (1988). Only the final results of the population balance are presented here, along with its application to the two crystallization models.

In any system that contains solid particles, a distribution of particle sizes is usually present. In a crystallization system, the distribution of crystals may be characterized by the population density, which is defined as the number of crystals of a given size range present in a unit volume of clear mother liquor. A macroscopic population balance is based on the conservation of the crystal-population density. The population balance is made around the crystallizer and is expressed mathematically as:

$$\frac{\partial n}{\partial t} + \frac{\partial (Gn)}{\partial L} + n\,\frac{d(\ln V)}{dt} = B(L) - D(L) - \sum_k n_k Q_k / V \qquad (3\text{-}1)$$

where: $B(L)$ = crystal birth rate (#/min-μm-cm^3)

$D(L)$ = crystal death rate (#/min-μm-cm^3)

G = linear crystal growth rate (μm/min)

k = integer denoting an inlet or outlet stream

L = crystal size (μm)

n = population density [= $n(L)$] (#/μm-cm^3)

n_k = population density in k^{th} stream (#/μm-cm^3)

Q_k = volumetric flow rate of kth stream (m^3/min) positive for flow in, negative for flow out

t = time (min)

V = suspension volume (m^3)

The terms on the left-hand side of Equation (3-1) represent the internal flux of the population density, whereas the flux of the population density from external sources is represented on the right-hand side of the equation. Several assumptions are required to simplify Equation (3-1) so that it may be of practical utility. First, steady-state operation of the crystallization system is assumed, which enables the first and third terms on the left-hand side to be neglected. The removal of the third term also requires a "thin" suspension in the crystallizer, where negligible change in the solids-

free volume occurs from the inlet to the outlet. Second, the crystallizer feeds are assumed to be particle-free, which allows the terms in the summation relating to the feeds to be zero. These first two assumptions are easily accomplished and verified in an experimental or industrial crystallizer. The next two assumptions are items that can not be constructed or constrained *a priori*, but are results of a particular solute/solvent system. These assumptions can be verified only after the crystallization experiments have been performed. The third assumption is that no crystal breakage or agglomeration occurs in the suspension volume, which allows the first and second terms on the right-hand side of Equation (3-1) to be neglected. This assumption is not only dependent on the system, but also on the conditions within the crystallizer, such as the rate of agitation. Finally, the crystal growth rate is assumed independent of crystal size (the ΔL law -- McCabe, 1929), which permits the growth rate to be placed outside the derivative in the second term on the left-hand side of Equation (3-1). These four assumptions allow Equation (3-1) to be reduced to the following expression:

$$G \frac{dn}{dL} + \sum_k n_k Q_k / V = 0 \tag{3-2}$$

The volumetric flow rates in Equation (3-2) are for crystallizer effluents only, which may have different crystal-size distributions than that inside the crystallizer. This simplified form of the population balance expression was used to develop the two crystallization models below.

3.2.1 Ideal Crystallizer Model

The ideal crystallizer model developed below is the well-known mixed-suspension, mixed-product removal (MSMPR) crystallizer. A schematic diagram of the MSMPR crystallizer is shown in Figure 3.1. Two additional assumptions are required to convert Equation (3-2) to the MSMPR model. These assumptions are that the suspension volume held in the crystallizer is perfectly mixed and that one effluent

stream exits the crystallizer and provides unclassified withdrawal of crystals. These restrictive assumptions require that the crystal-size distributions in any two discrete pockets of fluid in the suspension volume are equal and that the crystal-size distribution in the crystallizer effluent also equals the crystal-size distribution in the suspension volume ($n = n_k$). Integration of Equation (3-2), with only one effluent, for a population density of crystals of size zero to infinity yields:

$$n(L) = n^0 \exp(-L/G\tau) \qquad 0 \le L \le \infty \tag{3-3}$$

where: n^0 = nuclei population density [= n(L=0)] (#/μm-cm^3)

τ = particle residence time in the crystallizer [= V/Q_2] (min)

Equation (3-3) indicates that a semi-log plot of population density versus crystal size gives a negative slope proportional to the inverse of the product of the residence time and the growth rate, and also gives the intercept as the nuclei population density. Along with the population balance, a mass balance of the solute may be constructed around the ideal crystallizer in Figure 3.1 to give:

$$Q_1C_1 - Q_2C_2 = Q_2M_T \tag{3-4}$$

where: C_k = solute concentration (kg/m^3)

M_T = slurry density (kg/m^3)

For many solute/solvent systems, where the only streams are those in Figure 3.1 (no evaporation of solvent), the inlet and outlet volumetric flow rates are approximately equal. Therefore, the slurry density in Equation (3-4) may be calculated from the difference of the inlet and outlet solute concentrations:

$$C_1 - C_2 = M_T \tag{3-5}$$

The slurry density (the total mass of solute per volume of clear mother liquor) may also be calculated from the crystal-size distribution described by Equation (3-3). This is produced from the third moment of the distribution and is expressed as:

$$M_T = \rho_C k_V \int L^3 n(L)dL = 6\rho_C k_V n^0 (G\tau)^4 \tag{3-6}$$

where: k_V = crystal volumetric shape factor (m^3/m^3)

ρ_C = crystal density (kg/m^3)

The mass-average particle size of the crystal-size distribution may also be calculated from the distribution described by Equation (3-3). The mass-average particle size is a characteristic measure of the crystal-size distribution, and its value helps one to visualize the overall size of the crystals in the distribution. The mass-average particle size is derived from the third and fourth moments of the population density:

$$\mathscr{L} = \int L^4 n(L)dL \,/\, \int L^3 n(L)dL = 4G\tau \qquad (3\text{-}7)$$

where $\mathscr{L}$ is the mass-average particle size (μm). The above expressions are a result of the population balance and mass balance around an ideal crystallizer. In addition to these expressions produced from the two balances, a crystallization kinetics expression is needed to complete the development of the ideal crystallizer model.

Two physical phenomena are competing in a crystallizer to produce solid crystals of size L: the nucleation rate and the growth rate. The driving force for these two rates is the supersaturation of the solute in the solution. The dependence of nucleation and growth on supersaturation is not well understood and has been the focus of a great number of investigations (Nývlt *et al.*, 1985). In general, the growth rate has an approximately-linear dependence on supersaturation, whereas the dependence of the nucleation rate on supersaturation is characterized by a power relationship. Because the supersaturation of a Class II system in a back-mixed crystallizer is small and difficult to measure, the two rate expressions are combined to eliminate the supersaturation to give the relation: $B^o = k\, G^i$, where B^o is the nucleation rate, and i and k are constants. In a Class II solute/solvent system, the difference in solute concentration from inlet to outlet is independent of residence time, so the exit concentration approaches the equilibrium concentration and the crystallizer yield is independent of throughput. (Class I systems, on the other hand, reside in a crystallizer with significant supersaturation which is dependent on residence time and degree of mixedness and, as a result, the crystallizer yield is dependent on

throughput.) The slurry density of the solids suspension has been observed to affect the crystallization kinetics through a mechanism known as secondary nucleation (Larson *et al.*, 1968). The power input from the agitator and the hydrodynamics of the crystallizer internals have also been observed to affect the crystallization kinetics (Jancić and Grootscholten, 1984). From the nucleation/growth rate expression and the effects of secondary nucleation and power input, the crystallization kinetics of the solute/mother liquor system are typically characterized by the following semi-empirical expression:

$$B^0 = k_N \, \epsilon^h \, G^i \, M_T^{\,j} \tag{3-8}$$

where: B^0 = crystal nucleation rate [= n^0G] (#/min-cm^3)

ϵ = specific power input (W/kg of solution)

h, i, j, k_N = power law constants

Equations (3-6), (3-7), and (3-8) were consolidated to derive the design equation that is applicable to a continuous MSMPR crystallizer:

$$\tau = \left[\frac{6\rho_C k_V k_N \, \epsilon^h \, M_T^{\,j-1} \, \mathscr{L}^{i+3}}{4^{i+3}} \right]^{1/i-1} \tag{3-9}$$

The residence time (τ) of the crystals in the crystallizer is a fundamental design or operating parameter for the crystallizer. Similarly, the mass-average particle size ($\mathscr{L}$) is a parameter which adequately characterizes the crystal-size distribution and is of great utility when designing or operating downstream solids/liquid processing equipment. The slurry density or solids concentration (M_T) is a measure of the change in solute solubility from the crystallizer feed to the crystallizer effluent, and is useful in determining the yield of solids product from the crystallizer. The specific power input (ϵ) describes the degree of mixedness in the active crystallizer volume, thereby providing a means to calculate the energy dissipated into the solid/liquid suspension from the rotation rate of the stirring device.

The design equation was formulated with these four parameters to aid in the

design or simulation of the crystallizer. The design equation may be used in a design case where the residence time of the crystals in the crystallizer is computed from the slurry density and mass-average particle size desired. The design equation may also be used to simulate an operating crystallizer, where the mass-average particle size is predicted from the residence time and slurry density.

3.2.2 Modified Crystallizer Model

The modified crystallizer model developed below is similar to the mixed-suspension, classified-product removal (MSCPR) crystallizer. A schematic diagram of the MSCPR crystallizer is shown in Figure 3.2. The development of this model parallels that of the MSMPR model in Section 3.2.1. The basis of the modified model is the preferential removal of some particles, those whose size is larger than some critical size (L_c), at a finite rate from the crystallizer suspension volume. Although a cyclone is shown for illustrative purposes as the device removing the larger particles from the crystallizer in Figure 3.2, the mechanism which removes the particles of size L_c or larger is not important. The simplified population balance expression in Equation (3-2) may still be used, but the application of the expression is divided into two parts: one part for the population density of crystal sizes less than L_c and the other part for the population density of crystal sizes greater than L_c. Referring to Figure 3.2, the division of Equation (3-2) into two parts is written as:

$$G\frac{dn}{dL} + \frac{nQ_2}{V} = 0 \qquad 0 \le L \le L_c \qquad (3\text{-}10a)$$

$$G\frac{dn}{dL} + \frac{n(R+Q_2)}{V} = 0 \qquad L_c \le L \le \infty \qquad (3\text{-}10b)$$

where: L_c = critical crystal size where classification is discontinuous (μm)

R = volumetric flow rate through the recycle loop (m^3/min)

The consequence of the preferential removal of larger crystals is that the residence time of the larger crystals is smaller than that of the smaller crystals. The residence time of the under-sized crystals is $\tau_u = V/Q_2$ (as in the MSMPR crystallizer), whereas

the residence time of the over-sized crystals is $\tau_o = V/(R+Q_2)$. An additional parameter (z) is defined for the MSCPR model as the ratio of the two residence times:

$$z = \tau_u / \tau_o = (R+Q_2) / Q_2 \tag{3-11}$$

The value of z is always positive and larger than one. Equations (3-10) are integrated over their size range to give population density expressions for the two regions of crystal size:

$$n(L) = n^o \exp(-L/G\tau) \qquad 0 \le L \le L_c \tag{3-12a}$$

$$n(L) = n^o \exp((z-1)L_c/G\tau) \exp(-zL/G\tau) \qquad L_c \le L \le \infty \tag{3-12b}$$

The residence time in Equations (3-12) is the residence time of the under-sized crystals where the subscript has been dropped for clarity. When the value of z approaches one, the crystal-size distribution characterized by Equations (3-12) reduces to that characterized by Equation (3-3) in the MSMPR crystallizer model. Examination of Equations (3-12) suggests that a semi-log plot of the population density versus crystal size gives two lines where the slopes and intercepts are determined from the MSCPR parameters L_c and z, the nuclei population density, and the product of the growth rate and residence time.

A solute mass balance around the MSCPR crystallizer in Figure 3.2 enables calculation of the slurry density of the solids suspension:

$$Q_1C_1 - Q_2C_2 = Q_2M_T + R\,M_T^+ \tag{3-13}$$

where: M_T = slurry density of all crystals in suspension (kg/m^3)

M_T^+ = slurry density of over-sized crystals (kg/m^3)

As discussed in the development of the MSMPR model, the volumetric flow rates for most solute/solvent systems are approximately equal for the crystallizer set-up in Figure 3.2. As a result, Equation (3-13) may be reduced to:

$$C_1 - C_2 = M_T + (z-1)\,M_T^+ \tag{3-14}$$

The slurry density and the mass-average particle size are computed from the population density expressions and are written in the following form:

$$M_T = [A + Bz^{-4} \exp((z-1)L_c/G\tau))]\, \rho_C k_V n^0 (G\tau)^4 \tag{3-15}$$

$$M_T^+ = [Bz^{-4} \exp((z-1)L_c/G\tau))]\, \rho_C k_V n^0 (G\tau)^4 \tag{3-16}$$

$$\mathscr{L} = \{[C + Dz^{-5} \exp((z-1)L_c/G\tau))] \,/\, [A + Bz^{-4} \exp((z-1)L_c/G\tau))]\}\, G\tau \tag{3-17}$$

where:

$$A = 6 - \exp(-x)\,[x^3 + 3x^2 + 6x + 6]$$

$$B = \exp(-y)\,[y^3 + 3y^2 + 6y + 6]$$

$$C = 24 - \exp(-x)\,[x^4 + 4x^3 + 12x^2 + 24x + 24]$$

$$D = \exp(-y)\,[y^4 + 4y^3 + 12y^2 + 24y + 24]$$

$$x = L_c/G\tau$$

$$y = zL_c/G\tau$$

As the value of z approaches unity, the above expressions in Equations (3-15), (3-16), and (3-17) reduce to the slurry density and mass-average particle size expressions for the MSMPR crystallizer model, Equations (3-6) and (3-7). The kinetics expression used in the MSCPR model is the same as that used in the MSMPR model. Consolidation of Equations (3-15) and (3-17), along with the kinetics expression below (Eqn. (3-18)), yields the design equation for the MSCPR crystallizer:

$$B^0 = k_N\, \epsilon^h\, G^i\, M_T^j \tag{3-18}$$

$$\tau = \left[\frac{f_1 \rho_C k_V k_N\, \epsilon^h\, M_T^{j-1}\, \mathscr{L}^{i+3}}{f_2^{\,i+3}} \right]^{1/i-1} \tag{3-19}$$

where:

$$f_1 = [A + Bz^{-4} \exp((z-1)L_c/G\tau))]$$

$$f_2 = [C + Dz^{-5} \exp((z-1)L_c/G\tau))] \,/\, [A + Bz^{-4} \exp((z-1)L_c/G\tau))]$$

Equation (3-19) is similar in form to Equation (3-9), the MSMPR design equation. The two functions, f_1 and f_2, reduce to the values of 6 and 4, respectively, when the MSCPR parameter (z) is equal to one, thereby reducing the MSCPR design equation to the MSMPR design equation. Although Equation (3-19) is not explicit with respect to residence time (as is Equation (3-9)), the design or simulation of an MSCPR crystallizer may be performed using Equation (3-19). The MSCPR design equation and the equations used to to derive it were used to obtain and verify the crystallization

kinetics of the sulfur/solvent system in this study.

3.2.3 Comparison of Models

The comparison of the MSMPR and MSCPR models was studied thoroughly by Randolph (1965) and Larson and Randolph (1969). Their conclusions are presented below. The major consequence of the preferential removal of oversized particles is the reduction of the slurry density as compared with the mixed-product removal. This is illustrated by comparing the solids-concentration expressions for the MSMPR (mpr) and MSCPR (cpr) models when the same feed conditions prevail:

$$C_1 - C_2 = M_T(\text{mpr}) = M_T(\text{cpr}) + (z-1)\, M_T^{+} \qquad (3\text{-}20)$$

Since the values of all of the slurry densities and z are positive, the solids concentration for mixed-product operation is larger than that for classified-product operation: $M_T(\text{mpr}) > M_T(\text{cpr})$. The reduction in total mass (M_T) may be drastic, since the over-sized particles have more of a contribution to the total mass of the distribution than the under-sized particles. The amount of reduction is dependent on both the critical crystal size (L_c) and the MSCPR parameter (z). The mass-average particle size for the classified case is therefore smaller than that for the mixed-product case. The MSMPR crystal-size distribution is inherently a wide distribution, whereas the MSCPR distribution is narrower. As a result, the total surface area of the crystal-size distribution is typically smaller for the MSCPR crystallizer. To compensate for the reduced surface area, the growth rate for the MSCPR crystallizer is larger than that for the MSMPR crystallizer to produce the same solids production dictated by the left-hand side of Equation (3-20).

3.2.4 Effect of Residence Time on Models

The effect of residence time on the crystallization kinetics of the MSMPR model is easily derived from the framework given in Section 3.2.1. Although the effect of residence time on the kinetics of the MSCPR is much more complicated, the same

trends are expected as from the MSMPR model. Expressions are given below for the MSMPR model only and are derived from Equations (3-6), (3-8), and (3-9). When two crystallizations 1 and 2 are operated with all variables except residence time held constant, the growth rate, the nuclei population density, and the mass-average particle size are dependent on the two different residence times as follows:

$$G_2/G_1 = (\tau_1/\tau_2)^{4/(i+3)} \tag{3-21}$$

$$n^o{}_2/n^o{}_1 = (\tau_1/\tau_2)^{4(i-1)/(i+3)} \tag{3-22}$$

$$\mathscr{L}_2/\mathscr{L}_1 = (\tau_1/\tau_2)^{(1-i)/(i+3)} \tag{3-23}$$

The value of the kinetic order i produces three regimes of interest when the residence time decreases from case 1 to case 2 ($\tau_1 > \tau_2$). When $i < 1$, the growth rate increases, the nuclei population density decreases, and the mass-average particle size increases. For $i = 1$, the nuclei population density and mass-average particle size are independent of holding time. The growth rate increases, but the crystal-size distribution remains the same, since $G_2\tau_2 = G_1\tau_1$. The most commonly observed kinetic order is $i > 1$, where, with increasing residence time, both the growth rate and nuclei population density increase, but the mass-average particle size decreases. Furthermore, as the value of the kinetic order increases past one, the nuclei population density increases faster than the growth rate for a given change in residence time, thereby making it increasingly difficult to produce large crystals. The dependence of the crystallization kinetics on residence time provides a method for the determination of the kinetic order i for Equation (3-8) from the experimental data. The method requires varying the residence time in the crystallizer from run to run, plotting the subsequent growth rates, nuclei population densities, and mass-average particle sizes against the residence times on log-log scales, and using Equations (3-21) through (3-24) to obtain a value of the kinetic order (i).

The MSCPR model has two additional parameters that may be dependent on residence time. The critical size parameter (L_c) is predominantly determined by the

removal mechanism of large particles and is assumed independent of holding time since the theoretical model does not provide any further insight. However, the dependence of z on the crystallizer residence time is characterized by Equation (3-11): $z = (R+Q_2)/Q_2$. When the recycle flow rate (R) is held constant and the throughput (Q) increases (residence time decreases), the value of z decreases. This information may assist in the application of the MSCPR model to the experimental data.

3.2.5 Effect of Slurry Density on Models

The effect of solids concentration on the crystallization kinetics is also determined from the theoretical framework. Again, the complexity of the MSCPR model does not provide clear quantitative expressions, so the trends exhibited from the MSMPR model are developed here and are assumed applicable to the MSCPR model. Because the slurry density is so greatly affected by the preferential removal of large particles, the effect of the solids concentration on the MSCPR crystal-size distribution may deviate significantly from that predicted for the MSMPR crystallizer. The dependence of growth rate, nuclei population density, and mass-average particle size on the solids concentration is illustrated by considering two crystallizers operating at two different slurry densities, M_{T1} and M_{T2}. The following expressions were derived from Equations (3-6), (3-8), and (3-9):

$$G_2/G_1 = (M_{T2}/M_{T1})^{(1-j)/(i+3)} \tag{3-24}$$

$$n^0{}_2/n^0{}_1 = (M_{T2}/M_{T1})^{(i+4j-1)/(i+3)} \tag{3-25}$$

$$\mathcal{L}_2/\mathcal{L}_1 = (M_{T2}/M_{T1})^{(1-j)/(i+3)} \tag{3-26}$$

The secondary nucleation is oftentimes found to be directly proportional to the slurry density, thus j = 1. For this case, the growth rate and mass-average particle size are invariant. The nuclei population density increases proportionately with solids concentration because the total number of crystals increases. As a result, the slope of the crystal-size distribution remains constant and the intercept increases for increasing slurry density. When the value of j is other than one, the nuclei population density

always increases when the solids concentration increases. When $j < 1$, both the growth rate and mass-average particle size increase with increasing slurry density. When $j > 1$, G and $\mathscr{L}$ both decrease with increasing slurry density. The value of j may be determined experimentally by varying the slurry density, while holding all other variables constant, and casting the observed crystal-size distribution data in the form of Equations (3-24) to (2-26).

3.2.6 Effect of Impeller Power Input on Models

The effect of power input on the nucleation rate is expressed in an empirical form in Equation (3-8). The nucleation rate is expected to increase with power input. As more interactions between existing crystals, nuclei embryos, and other solid surfaces are produced from increased agitation, more nuclei are produced. This expectation may be verified by combining Equations (3-6), (3-8), and (3-9) to give the following expressions, where case 1 and case 2 have different impeller power inputs:

$$G_2/G_1 = (\epsilon_2/\epsilon_1)^{-h/(i+3)} \tag{3-27}$$

$$n^0{}_2/n^0{}_1 = (\epsilon_2/\epsilon_1)^{4h/(i+3)} \tag{3-28}$$

$$\mathscr{L}_2/\mathscr{L}_1 = (\epsilon_2/\epsilon_1)^{-h/(i+3)} \tag{3-29}$$

When h is positive, the growth rate and mass-average particle size decrease with increasing power input. The nuclei population density increases with power input. When the value of h is negative, the reverse trends are observed. Since the nuclei population density is expected to increase with power input, the value of h is expected to be positive. The power input may also affect the classification characteristics of the MSCPR model, particularly if the agitation rate is not sufficient to suspend all of the crystals so that stratification of the solids suspension occurs. Although the crystal-size distribution theory does not provide any information in this regard, attention to the full suspension of the resident crystals is required when performing crystallization experiments. The value of h may be determined from crystallization experiments where the impeller rotation is varied, the resulting crystal-size distribution data plotted

versus impeller power input, and Equations (3-27) through (3-29) fitted to the plots.

3.3 Thermal Crystallization Experimental Apparatus

A laboratory-scale continuous crystallization apparatus was used to study the crystallization of elemental sulfur from polyglycol ether solutions. The apparatus was constructed so that the crystallizer vessel was operated in either a back-mixed or fluidized-bed configuration.

3.3.1 Back-Mixed Crystallizer

The experimental apparatus used to study the continuous crystallization in a back-mixed crystallizer was composed of a hot tank and a cold tank, where the solvent and sulfur were continuously recycled. Refer to Figure 3.3 for a schematic diagram of the continuous crystallization apparatus. The overall concept of the apparatus was to pump hot solvent with dissolved sulfur from the solvent holding tank, through an in-line filter, and into the chilled crystallizer where the slurry was then purged back to the solvent holding tank. The variable-speed brass gear pump, carbon-steel in-line filter, and stainless-steel feed lines were electrically heat-traced to eliminate sulfur precipitation in the feed system. The in-line filter cartridge had a five-micron nominal rating. The hot, particle-free feed was introduced into the crystallizer through a double-walled, glass dip tube with its outlet located near the bottom of the crystallizer. The temperature of the feed solution was monitored at the stainless-steel/glass coupling, using a thermocouple. A digital temperature indicator was used for all thermocouple temperature measurements and provided temperature readings within $\pm$ 0.1^{o}C.

The crystallization vessel was a 2-liter jacketed glass reaction flask. All internals that came in contact with the sulfur/solvent slurry were made of glass. The solvent temperature in the crystallizer was maintained at a reduced temperature by pumping cooling water through the outer jacket. The cooling water was chilled using a

refrigerated/heated bath, which controlled the cooling water temperature to within ± 0.1^{o}C. The temperature of the crystallizer was monitored using a thermocouple that was held in a glass dip tube and immersed in the wetted volume. The vessel contents were agitated by a two-blade glass impeller. Figure 3.4 shows the dimensions of the vessel and impeller and the placement of the impeller inside the crystallizer. The impeller was coupled to a flexible shaft drive which was driven by a variable-speed electric motor with two shafts rotating at a maximum of 350 and 4000 RPM, respectively. The volume of the crystallizer slurry was controlled by a photoelectric level controller. The high-intensity lamp and the "electronic eye" were placed opposing each other around the crystallizer. The level controller intermittently actuated a solenoid valve on the exit line of the crystallizer. An emergency level alarm/switch was installed to disable the feed pump in the event of failure to actuate the exit valve or of closure of the valve by large sulfur nodules. The alarm/switch was thrown when a float, normally held above the wetted volume of the crystallizer, was buoyed up from its resting position by the rising liquid level.

Graduations were scribed on the side of the crystallizer to indicate the liquid volume in the vessel. The graduations were calibrated to include the displacement of the dip tubes and impeller located inside the vessel. A small tube, which projected up into the vessel, was fitted into the vertical exit port on the bottom of the crystallizer. A tee was attached to the bottom of the crystallizer exit line and was electrically heated. The solenoid valve was attached to a horizontal leg of the tee and was also electrically heated. A ball valve was attached to the vertical leg of the tee and functioned as the sample port for the crystallizer. The other horizontal leg was fitted with a thermocouple for temperature measurement. The effluent line from the solenoid valve was directed to the solvent holding tank, where the diameter and pitch of the line was such that the intermittently purged slurry drained completely from the line.

The solvent holding tank was a 30-liter cylindrical glass tank outfitted with a polypropylene lid which held auxiliary equipment that was immersed in the solution. The tank was partitioned into two sections by an off-center vertical stainless-steel baffle. The larger section had a port for the crystallizer effluent line from the solenoid valve and was designed to dissolve the sulfur crystals back into the solvent. The large section was stirred using an electric motor with three three-bladed propellers on its shaft, which extended down to the bottom of the tank. The temperature of the solvent holding tank was controlled by an automatic temperature controller and two electric immersion heaters, also located in the stirred section of the tank. The smaller section was designed to clarify the solvent by crystal settling, thereby providing a relatively solids-free solution at the entry of the feed pump suction line. The quiescent section was produced by four perforated aluminum plates oriented at an angle so that sulfur particles disengaged from the decelerating liquid, sloughed down the plates, and traveled back into the well-mixed section. The temperature of the solvent holding tank was measured with a thermocouple, which was placed near the inlet of the feed pump suction line.

3.3.2 Fluidized-Bed Crystallizer

The experimental apparatus used in the back-mixed crystallization work was modified to perform the fluidized-bed experiments. A schematic diagram of the fluidized-bed apparatus is shown in Figure 3.5. The crystallizer feed set-up was the same as in the back-mixed case. Two different zones were required in the crystallizer for the fluidized-bed experiments: a well-mixed zone in the bottom half of the crystallizer where the hot solution was fed into the solids/liquid slurry and a clarified zone in the top half of the crystallizer where the solids disengaged from the slow-moving liquid. These zones were produced by slowly rotating the impeller and by additional crystallizer internals which included four 50-milliliter test tubes, which were suspended into the top portion of the wetted crystallizer volume to reduce the

turbulent eddies in the upper portion of the fluid. A swirl inhibitor was also installed, which reduced the fluid rotation near the exit port of the crystallizer. An overhead siphon line, which was submerged in the upper portion of the wetted crystallizer volume, was connected to a 250-milliliter flask. The flask had ports leading to the solvent holding tank, to a purge valve, and to a pump that pumped solution to the bottom of the crystallizer. The fluid pumped back to the crystallizer was heated slightly by a heat-traced line to prevent sulfur deposition in the small stainless-steel gear pump. The temperature of the heated stream before it entered the pump was monitored using a thermocouple. An elutriation leg was attached to the bottom of the crystallizer, where the geometry of the leg produced a uniform velocity profile up to the crystallizer exit port. A separatory funnel was attached to the bottom of the elutriation leg that allowed removal of sulfur crystals during operation of the crystallizer.

3.3.3 Apparatus for Analyzing the Crystal-Size Distribution

The analysis of the size and distribution of sulfur crystals produced from the crystallizer was performed using a particle-size analyzer that is based on a light-blockage technique. The analyzer was a HIAC PSA-720 (Pacific Scientific) with a HIAC JS-600 sensor composed of sapphire windows and a 600-micron (μm) aperture. The analyzer and sensor were capable of measuring particles from 12 to 540 μm (1:45) in a maximum of 23 channels. The size of each channel increased geometrically by a factor of $\sqrt[23]{45}$. The analyzer also had the capability to subtract a background particle count, to average up to five samples, and to report the data as a differential distribution on both a number and volume basis. A personal computer was connected to the analyzer for the acquisition of the particle-size distribution data. An oscilloscope was also connected to the analyzer to monitor the performance of the sensor. Refer to Figure 3.6 for a schematic diagram of the analyzer set-up. The crystallizer slurry was fed through the sensor from an overhead vessel and emptied

into a waste flask. The 1-liter feed vessel had a Teflon stopcock and also had graduations every 10 milliliters. The vessel contents were stirred using a two-blade impeller driven by an electric motor. The analyzer was calibrated using mono-sized polystyrene microspheres of sizes 19.73 and 42.79 μm (Coulter Electronics) and mono-sized glass microspheres of sizes 31.2, 49.3, 102, 204, and 402 μm (Duke Scientific) . The calibration was verified by preparing and analyzing a known distribution of silica gel particles.

The construction of the HIAC analyzer and sensor is quite simple. The sensor has a rectangular passageway through which suspended particles flow. A collimated-light beam passes through a solvent-resistant window, traverses the passageway, and then passes through another window. The light falls on a photoelectric detector, whose output is an electrical current that is proportional to the incident light. The current is converted to a voltage, which is monitored by the analyzer. A base-line voltage is maintained from the light passing through the fluid in the absence of particles. As a particle passes through the light beam, a voltage pulse is generated whose size is proportional to the size of the particle. Using analog/digital circuitry, the analyzer counts the pulses and sorts them into the 23 channels. The sorting is executed by comparing the height of a voltage pulse to the threshold voltage for each of the channels. These threshold voltages are adjustable to aid in calibrating the sensor/analyzer combination.

The calibration of the sensor and analyzer was made using spherical particles. As a result, the analysis of the sulfur crystals yielded crystal-size distribution data which inherently assumes spherical sulfur crystals. To compensate for the non-spherical sulfur crystals, a volumetric shape factor (k_V) was used. See Section 3.4.4 for a discussion of the data reduction and analysis using k_V. The sensor is also highly sensitive to the flow rate of the fluid passing through it. The constriction of the sensor passageway allowed the flow rate to vary only two percent as the height of the

fluid in the feed vessel dropped from its maximum to its minimum. The flow rate used for the calibration of the HIAC sensor/analyzer combination was used in the sulfur crystal-size distribution analysis.

3.4 Experimental Method

The solvent used in all of the crystallization experiments was triethylene glycol dimethyl ether or Triglyme (SpecialtyChem Products Ansul E-161). This solvent was chosen from a list of preferred solvents for the UCBSRP (Sciamanna, 1986 & 1988) because it dissolves more sulfur than the monoethers and because there is kinetic data for the catalyzed liquid-phase reaction of H_2S and SO_2 in this solvent (Neumann, 1986), which was required in the subsequent reactive crystallization work. With the exception of water, no additives were used in the crystallization of sulfur from solution. The sulfur (Mallinckrodt Sublimed Sulfur) used in this study was assumed to be the cyclo-octa (S_8-ring) allotropic form.

3.4.1 Back-mixed Crystallizer Operation

The crystallizer operating temperature was always 30°C. The cooling water temperature was manually controlled to maintain the crystallizer temperature. The lowest temperature of the cooling water was approximately 5°C (corresponding to the smallest liquid residence time in the crystallizer or largest throughput) so that the temperature difference across the glass heat-transfer wall was relatively small. Other than several sulfur nodules which grew on the scratches or pits on the glass heat-transfer surface, no crystalline fouling was observed inside the crystallizer. The temperature of the solvent in the solvent holding tank was nominally 50°C, but was varied to achieve different sulfur concentrations in the crystallizer feed. The feed solution, heated in the feed lines, entered the crystallizer at a temperature of approximately 54°C, or roughly four degrees higher than the temperature of the solvent in the solvent holding tank. The level controller intermittently purged five

percent of the total wetted crystallizer volume back to the solvent holding tank. The total wetted volume in the crystallizer was measured from the graduations on the side of the crystallizer vessel and was set by the variable on/off delay times for the level controller.

When starting up the apparatus, the solvent in the feed lines and solvent holding tank were brought up to temperature before pumping solution into the crystallizer. The crystallizer was seeded with sulfur crystals taken from the previous run to reduce the time required to achieve steady-state operation with respect to the crystal-size distribution. Samples of the crystallizer slurry were taken and analyzed to watch the progression to a steady-state crystal-size distribution. The time required to reach a steady-state crystal-size distribution was approximately six residence times after the flow rates and temperatures became invariant. When shutting down the apparatus, the crystallizer and solvent holding tank were cooled simultaneously while continuing to pump solution to the crystallizer to prevent sulfur precipitation in the feed lines.

As mentioned in Section 3.3.1, the internals of the crystallizer were all made of glass. Initial crystallization runs with metal or plastic components in contact with the sulfur/solvent slurry exhibited gross sulfur encrustation on the non-glass surfaces. For example, four stainless-steel baffles were suspended into the wetted volume around the perimeter of the vessel, with a small clearance between the baffles and the wall, in an attempt to reduce the vortex of the stirred solution. During a crystallization run, the stainless-steel baffles were encrusted to the point that all of the sulfur grew solely on the baffles to produce a clear mother liquor. A draft-tube baffle was also installed to try to improve the mixing in the vessel. The Teflon baffles also produced the encrustation observed with the metal baffles. This susceptibility of materials of construction to sulfur encrustation may pose a problem when operating an industrial crystallizer.

As also mentioned in Section 3.3.1, a small glass tube was fitted into the vertical

exit port of the experimental crystallizer. This was done to reduce the amount of solid sulfur leaving the crystallizer through the exit port on the bottom of the crystallizer. Both solids and liquid were purged through the port when the level controller actuated the solenoid valve. When the solenoid valve was turned off, the liquid flow stopped. However, large sulfur crystals were observed settling down the exit port and into the tee when the valve was closed. Although the sulfur crystals were fully suspended in the wetted crystallizer volume, some sulfur crystals disengaged from the liquid and settled down the port. These large sulfur crystals were few in number, but had a large contribution to the total weight of the solids. The addition of the small glass tube in the port reduced (but did not eliminate) the amount of sulfur leaving the crystallizer. The small glass tube also allowed long-time operation of the crystallizer because sulfur nodules, which grew on the few scratches on the glass, would eventually fall off and swirl around the bottom and break into small fragments. Without the small tube, these nodules would fall through the exit port and plug the solenoid valve.

3.4.2 Fluidized-Bed Crystallizer Operation

The operation of the fluidized-bed crystallizer was very similar to that of the back-mixed crystallizer. To start a run, the crystallizer and the 250-milliliter flask were filled with solvent to provide the liquid needed to form the siphon in the overhead tube. Once the siphon was made, the height of the small flask (its solvent holding tank return leg) was adjusted to set the crystallizer volume. Solvent was then pumped to the elutriation leg. The upward fluid flow in the elutriation leg suspended the crystals in the well-mixed zone of the crystallizer. The crystallizer was seeded with sulfur crystals to reduce the initial surge of nucleation. As the size of the crystals grew with time, the height of the fluidized-bed zone was reduced as the mixing remained constant. Once the size of the crystals was large enough that the settling velocity was larger than the upward flow of solvent in the elutriation leg, the crystals settled down into the lower separatory funnel. The funnel was periodically isolated by

closing the upper stopcock and then removed to recover the large sulfur particles.

3.4.3 Crystal-Size Distribution Analysis

The crystal-size distribution of the crystallizer effluent was determined by sampling the crystallizer contents and analyzing the sample using the HIAC PSA-720 apparatus. A sampling method was developed to ensure that the actual crystal-size distribution residing in the crystallizer was analyzed by the particle-size analyzer. The method required that the crystallizer slurry be sampled without affecting the crystal-size distribution and that the crystal-size distribution not be altered during analysis. Wash-out experiments were performed where a known distribution of particles was charged into the crystallizer and then sampled for analysis. The observed distribution from the analyzer was compared to the distribution put into the crystallizer. The geometry of the crystallizer, with its exit port on the bottom, allowed the larger particles of the known distribution to settle out of the well-mixed region. Since these settled particles accumulated in the tee below the crystallizer, they were removed by purging the sample valve before a sample was taken so that the sample accurately represented the distribution residing the crystallizer. Of course, the crystal-size distribution of the crystallizer contents became increasingly more skewed to the smaller particles with increasing time since the settling of large particles removed them from the well-mixed zone. The method described below provided good agreement between the two distributions.

The volume of the sample taken from the crystallizer was approximately 100 milliliters, about the same size as the volume of slurry purged from the crystallizer by the level controller. The sample was diluted with 900 milliliters of diluent because the sample particle density was too high for the sensor to resolve individual particles. The oscilloscope was used to verify that the sensor was not saturated with too many particles. Process solvent was used as diluent, where it was chilled to 5°C, vacuum-filtered to remove sulfur crystals, and heated to 32°C. Some of the warm diluent was

put in an Erlenmeyer flask and forced up the analysis flow tube to displace the air in the flow tube with clean solvent. The rest of the warm diluent was charged into the analyzer feed vessel, stirred vigorously to remove air bubbles from the submerged surfaces, and then allowed to sit still so that the bubbles came to the surface. The stopcock was opened and diluent allowed to flow through the sensor so that a background particle count was taken. The volume of the diluent analyzed for the background was the same as the volume of the sample analyzed. A 250-milliliter separatory funnel was heated to 35°C and used to hold the crystallizer sample while being transported from the crystallizer to the analysis apparatus. The crystallizer sample port was purged so that sulfur residing in the tee was washed away and then a 100-milliliter crystallizer sample was drained into the warm funnel. The sample was mixed with the diluent, while care was taken to make sure all the sulfur crystals were emptied into the analyzer feed vessel and that no air bubbles were entrained in the feed vessel. The stopcock was opened and the slurry allowed to drain through the sensor. At least two repetitions of 10,000 particles each were counted and averaged for each sample taken from the crystallizer. The background was subtracted from the averaged count, where the background was typically less than one percent of the averaged count. Steady-state operation with respect to the crystal-size distribution was assumed when three distributions gave reproducible results over a period spanning nine residence times.

3.4.4 Data Reduction

The data taken from the particle-size analyzer were reduced to a form applicable to the crystal-size distribution models discussed in Section 3.2. The particle-size analyzer produced a particle count Δ_i per size range ΔL for the 23 channels and also calculated average distribution values. A sample of the HIAC PSA-720 output is listed in Appendix B. The population density was calculated from the particle-count data using the following expression:

$$\frac{n\rho_C k_V}{M_T} = \frac{\Delta_i}{\Sigma(\Delta_i L_i^3)\Delta L} \tag{3-30}$$

where: n = population density [= n(L)] (#/μm-cm^3)

ρ_C = crystal density (kg/m^3)

k_V = crystal shape factor (m^3/m^3)

M_T = slurry density (kg/m^3)

Δ_i = particle count in channel i

L_i = mean particle size of channel i (μm)

ΔL = width of channel i (μm)

The left-hand side of Equation (3-30) is called the specific population density. The data from the experimental crystallization runs were kept in this specific form because the values of the crystal density (ρ_C), the volume shape factor (k_V), and the slurry density (M_T) were not known for all of the runs. The crystal density is of course tabulated, but the density of the crystals produced from the crystallization experiments was probably different than the literature value. The crystal density was also difficult to measure accurately since solvent was expected to adhere to the crystals' surfaces and to be occluded inside the crystals. The shape factor may be estimated by assuming spherical crystals: $k_V = \pi/6$ (which is a good assumption for most crystals), but no attempt was made to measure the sulfur crystal shape factor. As discussed later, the slurry density was also very difficult to measure accurately. As a resolution to these problems, the application of both of the crystallizer models was made to the specific population density data instead of estimated population density data. The application is easily performed because the specific population density may be computed from the theoretical models by rearranging Equations (3-6) and (3-15). An error analysis was also formulated which took errors produced from the particle-size analyzer and converted them, using Equation (3-30), to specific population density errors. The computer program used to reduce the raw data from the particle-size analyzer is listed

in Appendix B, along with a description of its algorithm and a sample output.

3.4.5 Operating Parameters for the Experimental Crystallizer

3.4.5.1 Variable Residence Time

The residence time (τ) of the solid sulfur crystals was assumed to be equal to the residence time of the liquid. The residence time of the liquid was varied from run to run by changing the flow rate of the feed solution. The graduations scribed on the crystallizer vessel were used to measure the residence time of the liquid in the following manner. As the level controller intermittently purged slurry from the crystallizer, the liquid level cycled up and down at the same height as the range of graduations. The time elapsed for the liquid level to travel from the lower mark to the upper mark was measured to determine the average flow rate of incoming solution at the temperature of the crystallizer. The active crystallizer volume was calculated from the average of the upper and lower graduation values. The active crystallizer volume was typically 1850 milliliters. The residence time was then computed from the flow rate and the active crystallizer volume. The residence time was varied from 4 to 70 minutes.

3.4.5.2 Variable Slurry Density

The slurry density (M_T) of the crystallizer effluent was varied by manipulating the temperature of the feed solution. The feed solution temperature was controlled at the solvent holding tank and was held constant for each run. The temperature of the solvent holding tank was operated at either 40°, 50°, or 60^oC, while keeping the temperature of the crystallizer constant at 30^oC. The actual feed temperature was slightly higher so that the stream was superheated with respect to the sulfur saturation temperature, which was the temperature of the solvent holding tank. The slurry density of the crystallizer contents was measured by taking a large sample from the crystallizer. The sample port was first purged to remove any solid sulfur residing in

the tee. Approximately 500 milliliters of slurry was then taken from the crystallizer and quickly vacuum-filtered to separate the sulfur crystals from the mother liquor. This procedure was performed only once at the end of each run because taking this large a sample upset the system so badly that many residence times were required to reach a steady-state crystal-size distribution again. The large volume of slurry was required because the slurry density produced from the sulfur/solvent system and the operating temperatures was small (1 to 10 kg/m^3). The sulfur crystals were washed with a chilled water/ethanol mixture to remove residual solvent from the crystals and then air-dried. The volume of clear mother liquor and the mass of filtered crystals were measured and the slurry density computed from the ratio of the mass and volume. Comparison of the measured and predicted values of the slurry density is discussed in Section 3.6.3.

3.4.5.3 Variable Impeller Power Input

The specific power input (ϵ) for mixing the crystallizer contents was varied by changing the speed of rotation of the impeller shaft. The speed of rotation was measured using a stroboscope, which was calibrated against the alternating-current line frequency from the electric power receptacle. The speed of rotation was made at three values: 215, 350, and 680 revolutions per minute (RPM). The type of impeller and the location of the impeller remained constant throughout the thermal crystallization study. The impeller shaft was rotated in a clockwise direction, which forced fluid downward since the two impeller blades were pitched (1:1). No baffles were present inside the crystallizer. The impeller shaft was located on the center-line of the crystallizer.

3.4.5.4 Variable Water Concentration in the Solvent

The concentration of water in the process solvent was varied by adding distilled water to, or stripping water from, the solution. Since the solvent is hygroscopic, it

absorbed water from the atmosphere during the experiments. Although the crystallization apparatus was a closed system, the solvent was frequently handled outside of the apparatus to determine slurry density and crystal-size distribution. The water concentration was monitored between each run to hold in check the effect of water concentration when other parameters were being studied. When the effect of water concentration on the crystallization kinetics was studied, the range of water concentration was varied from 0.29 to 5.0 weight percent. The water concentration was determined using gas chromatography, where heptane was added as a tracer component to achieve better accuracy. Heptane was used as the tracer because it was not present in the crystallization apparatus. Heptane has a boiling point near that of water so that it eluted from the gas chromatograph near the water peak. Standard solutions of "clean" Triglyme, heptane, and water were made, in which the amount of water was varied but the amount of heptane remained constant. These solutions were injected in the gas chromatograph to construct a calibration curve. The "clean" Triglyme used in the calibration standards was produced by pretreating the purchased Triglyme, which had absorbed water during manufacture and handling. The Triglyme was pretreated to remove the water by heating it to approximately 100°C and sparging dry nitrogen through it for at least one hour. Once the calibration was made, the water concentration in the solvent used in the apparatus was determined. A known amount of heptane was added to each solvent sample taken from the apparatus and the water concentration in the sample computed from the gas chromatograph output and the calibration curve.

3.5 Computational Method and Data Analysis

Four analyses were made of the crystal-size distributions produced from the crystallization apparatus. Two of these analyses were for the ideal or MSMPR crystallizer model and the remaining two analyses were for the modified or MSCPR crystallizer model. A description of these four analyses is provided here. In addition

to the analyses, the computational methods for the effects of residence time, slurry density, impeller power input, and water concentration are described below.

3.5.1 Ideal Crystallizer Model

The first analysis, the simple MSMPR, was performed by fitting the following equation to the experimental data:

$$n(L)\rho_C k_V/M_T = (n^0\rho_C k_V/M_T)\exp(-L/G\tau) \tag{3-31}$$

Equation (3-31) was produced by multiplying Equation (3-3) by $\rho_C k_V/M_T$ to accommodate the form of the experimental data produced from Equation (3-30). A semi-log plot of specific population density versus particle size was made and the slope and intercept computed from a least-squares regression. The specific nuclei population density and growth rate were then calculated from the fitted constants and from the residence time observed during the experiment. An equation similar to the form of Equation (3-31) was written for the definition of the specific nucleation rate:

$$B^0\rho_C k_V/M_T = (n^0\rho_C k_V/M_T)\,G \tag{3-32}$$

The specific nucleation rate (Equation (3-32)) and mass-average particle size (Equation (3-7)) were also calculated for the simple MSMPR model.

The second analysis, the constrained MSMPR, was made by first rearranging Equation (3-6):

$$n^0\rho_C k_V/M_T = 1/6(G\tau)^4 \tag{3-33}$$

The log of Equation (3-31) was combined with Equation (3-33) to eliminate the specific nuclei population density:

$$\ln(n(L)\rho_C k_V/M_T) = -\ln(6) - 4\ln(G\tau) - L/G\tau \tag{3-34}$$

A one-parameter optimization was used to find the value of G which best fit the experimental crystal-size distribution. An objective function, composed from Equation (3-34), was derived using a least-squares criterion. The objective function was reduced to a recursion relation, where an initial guess for the growth rate was provided from the simple MSMPR analysis. This type of analysis was suggested by

White and Randolph (1987). The benefit of the constrained MSMPR analysis is that it requires the fitted crystal-size distribution parameters ($n^0\rho_C k_V/M_T$ and G) to satisfy both the population balance and mass balance expressions. Therefore, the constrained MSMPR model gives the best estimates of $n^0\rho_C k_V/M_T$ and G. Values for the specific nuclei population density, specific nucleation rate, and the mass-average particle size were computed from Equations (3-33), (3-32), and (3-7), respectively. A comparison of the experimental data and the results from the two MSMPR analyses was made for each run to identify errors in the data acquisition and reduction and to provide clues as to how to more accurately model the experimental crystallizer. The computer program used for the MSMPR analysis, the description of its algorithm, and a sample output is listed in Appendix B.

3.5.2 Modified Crystallizer Model

The two analyses for the MSCPR model were similar to those for the MSMPR model. First, the MSCPR analysis required a value for the critical particle size (L_c). This value was produced by observing the distributions produced from the MSMPR analyses. When comparing the fitted MSMPR model to the experimental data, the data exhibited a sharp "knee" in the distribution at approximately 250 μm for all of the crystallization runs performed. An in-depth discussion of the method of determining the value of L_c is located in Section 3.6.1.

The first analysis, the simple MSCPR, was based on Equations (3-12), which were multiplied by $\rho_C k_V/M_T$ so that the form of the distribution expressions were compatible with the experimental data produced from Equation (3-30):

$$n(L)\rho_C k_V/M_T = (n^0\rho_C k_V/M_T)\exp(-L/G\tau) \qquad 0 \le L \le L_c \qquad (3\text{-}35a)$$

$$n(L)\rho_C k_V/M_T = (n^0\rho_C k_V/M_T)\exp((z-1)L_c/G\tau)\exp(-zL/G\tau) \qquad L_c \le L \le \infty \qquad (3\text{-}35b)$$

Equation (3-35a) was fit to a semi-log plot of specific population density versus particle size for sizes less than L_c, and the resulting slope and intercept used to determine values for the growth rate and specific nuclei population density.

Equation (3-35b) was then fit to the data for sizes greater than L_c and the subsequent slope used to determine the value of z. The values for the specific nucleation rate and mass-average particle size were computed for the simple MSCPR model using Equations (3-32) and (3-17), respectively.

In the second analysis, the constrained MSCPR, the mass balance was used as an additional constraint on the population balance expression. The slurry-density expression in Equation (3-15) was rearranged to give:

$$n^0 \rho_C k_V / M_T = 1/f_1 (G\tau)^4 \tag{3-36}$$

Equation (3-36) was substituted into the log of Equations (3-35) to eliminate the specific nuclei population density, and gave the following expressions:

$$\ln(n(L)\rho_C k_V/M_T) = -\ln(f_1) - 4\ln(G\tau) - L/G\tau \qquad 0 \le L \le L_c \tag{3-37a}$$

$$\ln(n(L)\rho_C k_V/M_T) = -\ln(f_1) - 4\ln(G\tau) + (z-1)L_c/G\tau - zL/G\tau \qquad L_c \le L \le \infty \tag{3-37b}$$

A two-parameter optimization was used to find the value of G and z which best fit the experimental crystal-size distribution. As in the MSMPR analysis, an objective function was constructed from a least-squares criterion. Instead of deriving a recursion relation, however, the complexity of the objective function required a simple marching technique, where the values of G and z were found for the global minimum of the objective function. Initial values of G and z were taken from the results of the simple MSCPR analysis. Values for the specific nuclei population density ($n^0 \rho_C k_V / M_T$), specific nucleation rate ($B^0 \rho_C k_V / M_T$), and the mass-average particle size ($\mathscr{L}$) were then computed for the constrained MSCPR analysis from Equations (3-36), (3-32), and (3-17), respectively. The computer program for the MSCPR analysis, the description of its algorithm, and a sample output is listed in Appendix B.

3.5.3 Effect of Operating Parameters on Models

The methods of using the two theoretical models to determine the dependence of the crystallization kinetics on the operating parameters are discussed below. After the effect of each parameter on the kinetics was found, the models were then used to

predict and ultimately verify the experimental results.

3.5.3.1 Variable Residence Time

To determine the kinetic order of the sulfur/solvent system, an analysis was made on the data from the crystallization runs where the residence time was varied but where the slurry density, impeller power input, and the concentration of water in the solvent were held constant. The kinetics expression, Equation (3-8), was multiplied by $\rho_C k_V / M_T$ so that the specific nucleation rate from the experimental data could be used. The dependence of specific nucleation rate on impeller power input and slurry density was neglected for the variable residence time study (h = 0; j = 1), so Equation (3-8) was converted to the following expression:

$$B^0 \rho_C k_V / M_T = k_N \rho_C k_V \, G^i \tag{3-38}$$

A least-squares regression was made on a log-log plot of specific nucleation rate versus growth rate to produce values for the kinetic order (i) and the kinetic constant ($k_N \rho_C k_V$). The value of k_N was computed assuming ρ_C = 2070 kg/m^3 and $k_V = \pi/6$. The regression was performed on the results from the application of the constrained MSMPR and MSCPR models on the experimental data. The value of i was also determined from the dependence of growth rate, nuclei population density, and mass-average particle size on residence time, as described by Equations (3-21), (3-22), and (3-23). These values of i were compared to that obtained from the regression of specific nucleation rate versus growth rate.

The value of the critical particle size (L_C), used in the MSCPR model, was initially determined by observing the location of the "knee" in the crystal-size distributions which were produced from the experimental crystallization runs. An L_C sensitivity analysis was performed on the constrained MSCPR model, where the predicted mass-average particle size for each run was compared to that observed from each experimental run. A quantitative comparison was made by summing the squares of the differences between the observed and predicted values of the mass-average particle

size for all of the runs for each critical particle size chosen. The computer program discussed in Section 3.5.2 and listed in Appendix B was well-suited to perform the sensitivity analysis, since L_c is one of the input variables.

The dependence of the MSCPR parameter z on residence time was also determined. An average value of z was computed from all of the experimental runs which was then used to reconstruct the fitted crystal-size distributions. Equations (3-37) were again used, but instead of minimizing the objective function for both z and G, z was held constant at the average value and the value of G found that minimized the objective function. The new value of G, along with the average z and L_c, were used to compute the specific nuclei population density. These z-constrained values were used to reconstruct the crystal-size distributions for each run and compare them to the experimental specific population density versus particle size data.

The design equations for the two models, Equations (3-9) and (3-19), were used to calculate the residence time required to produce a certain mass-average particle size. These calculated values were then compared to the observed values from the experiments. The dependence of residence time on slurry density and impeller power input was neglected in Equations (3-9) and (3-19). The values of the kinetic order and kinetic constant, produced from the application of Equation (3-38) to the experimental data, were used in the design equations. In addition, the average z and L_c were used in the MSCPR model. The calculation for the residence time from the MSMPR model was straightfoward since Equation (3-9) is explicit with respect to residence time. However, the calculation for the residence time from the MSCPR model was more complex since Equation (3-19) is implicit with respect to residence time. Combining Equations (3-19) and (3-17), the value of the residence time was solved iteratively, along with the growth rate. A computer program and its algorithm, used to compute the residence time for a desired mass-average particle size (a design case), are listed in Appendix B. From these calculations, two curves of residence time

versus mass-average particle size were generated for the MSMPR and MSCPR models and then compared to the experimental data. As an extension of this comparison, a sensitivity analysis of the MSCPR design model on the value of z was also performed. Curves were generated for different values of z using the same method of computation as outlined above for the MSCPR model. The resulting curves were compared to the experimental data of residence time and mass-average particle size to substantiate the use of the average value of z for the MSCPR design model.

Finally, the crystal-size distributions for the experimental runs were predicted from the MSCPR design equation, the average value of z, the critical particle size, and the fitted constants from Equation (3-38). The residence times from the runs were used as inputs to the design equation, where the dependence on solids concentration and power input was ignored. The design equation and the mass-average particle size equation were again combined to compute the growth rate, using an iterative technique. An initial guess of the growth rate was calculated from the MSMPR model. The computer program and its algorithm, used to predict the crystal-size distributions (an operating case), are listed in Appendix B. The specific nuclei population density was then calculated from the inverse of the slurry density expression, Equation (3-36). From the growth rate and specific nuclei population density, the crystal-size distribution was plotted and then compared to the distribution observed from the experimental runs.

3.5.3.2 Variable Slurry Density

The dependence of the crystallization kinetics on the slurry density was determined from crystallization runs where both solids concentration and residence time were varied. The values of the slurry density measured from the experimental runs were compared to that calculated from the MSMPR and MSCPR models. The slurry density for the MSMPR model was calculated from Equation (3-5):

$$M_T(mpr) = C_1 - C_2 \tag{3-39}$$

The values for the concentration of sulfur in the inlet and outlet streams were computed from the sulfur solubility expression presented in Chapter 2. The slurry density for the MSCPR model was calculated by combining Equations (3-14) and (3-16) to give:

$$M_T(cpr) = (C_1 - C_2)/[1 + B(z-1)\exp((z-1)L_c/G\tau))(n^0\rho_C k_V/M_T)(G\tau/z)^4] \quad (3\text{-}40)$$

The results from these calculations were used to compute the reduction of solids concentration as a result of the preferential removal of over-sized crystals. The results from these calculations were also used as inputs for the determination of the constants in the crystallization kinetics expression. The kinetics expression used was the product of $\rho_C k_V/M_T$ and Equation (3-8):

$$B^0\rho_C k_V/M_T = k_N\rho_C k_V\, G^i\, M_T^{j-1} \quad (3\text{-}41)$$

In Equation (3-41), the variables are in the same form as the experimental data. The dependence on impeller power input was neglected since the impeller rotation remained constant. After Equation (3-41) was linearized by taking the log of both sides, a multiple variable least-squares regression was performed to determine the values of i, j-1, and $k_N\rho_C k_V$. The value of k_N was computed assuming ρ_C = 2070 kg/m^3 and $k_V = \pi/6$. Three regressions were made, corresponding to the three values of the solids concentration: M_T(observed), M_T(mpr), and M_T(cpr). The value of j was also computed from the expressions derived from the theoretical framework relating the effect of slurry density on the crystallization parameters. Equations (3-24), (3-25), and (3-26) were used to compute the value of j from the dependence of growth rate, nuclei population density, and observed mass-average particle size on slurry density.

The values of residence time and mass-average particle size, observed from the experimental runs, were plotted in groups according to their solids concentration. The design equation for the MSCPR model was used, with the constants produced from the multiple variable regression, to generate curves which were plotted with the experimental data. The average value of z and the critical crystal size, L_c, produced

from the variable residence time study were also used. The design equation (3-19), mass-average particle size equation (3-17), and the two slurry density equations (3-15) and (3-40) were combined to find the residence time required to produce a desired mass-average particle size and slurry density (a design case). Refer to Appendix B for the computer program and algorithm used to determine the residence time. The curves and experimental data were compared to ascertain the ability of the design equation to predict the residence time required to produce a desired mass-average particle size and slurry density.

Finally, the crystal-size distributions for the experimental runs were predicted from the MSCPR design equation, the fitted constants from Equation (3-41), and the average value of z and L_c. The residence times from the experimental runs were used as inputs to the design equation, where the dependence of the impeller power input was ignored. The design equation (3-19), the mass-average particle size equation (3-17), and the solids concentration equations (3-15) and (3-40) were combined to compute the growth rate. The complexity of these equations required an iterative solution. An initial guess of the growth rate was calculated from the MSMPR model. A listing of the computer program and its algorithm, used to predict the crystal-size distribution (an operating case), are located in Appendix B. The specific nuclei population density was then calculated from the inverse of the solids concentration expression, Equation (3-36). From the growth rate and specific nuclei population density, the crystal-size distribution was plotted and then compared to the distribution observed from the experimental runs.

3.5.3.3 Variable Impeller Power Input

The dependence of the crystallization kinetics on the impeller power input was determined from crystallization runs where the rotation rate of the impeller shaft was varied. The values for the impeller power input were computed using the method presented by Rushton *et al.* (1950). The method is based on the relationship of three

dimensionless groups (power, Reynolds, and Froude) to the geometry of the impeller and the tank holding the mixed solution. The working equations, which were used to calculate the specific power input, are shown here :

$$\epsilon = P/V\rho_L = \Phi\ Fr^m\ (N^3 D_i^5/V) \tag{3-42}$$

$$\Phi = \Phi\ (\mathbf{Re}, \text{ system geometry, \# baffles, etc.}) \tag{3-43}$$

$$m = (a - \log(\mathbf{Re}))/b \tag{3-44}$$

where: a, b = fitted constants [= fxn (geometry, baffles)]

D_i = impeller diameter (m)

Fr = Froude number [= $N^2 D_i/g$]

g = gravitational constant (m/sec^2)

m = Froude number exponent

N = rotation rate of impeller (sec^{-1})

P = power input to impeller (W = N-m/sec)

Re = Reynolds number [= $ND_i^2\rho_L/\mu$]

V = suspension volume (m^3)

ϵ = specific power input (W/kg of solution)

μ = viscosity of liquid (kg/m-sec)

ρ_L = density of liquid (kg/m^3)

Φ = power function

The constants a and b were assigned values (2.3 and 18, respectively) which were reported by Rushton *et al.* that corresponded to a three-blade, propeller-type impeller in a flat-bottom tank, where the pitch of the impeller blades was 1:1. The tank-to-impeller diameter ratio was 2.7, and the impeller clearance-to-impeller diameter and the height of liquid-to-tank diameter ratios were both 1.0. This particular impeller/tank geometry was the most similar of those studied by Rushton *et al.* to that of the experimental crystallizer in this study. The pitch and geometry ratios for the experimental crystallizer used in this study were slightly different: 1:1, 1.69, 0.50, and

2.46, respectively. Two additional differences between the two systems were that the crystallizer had a curved bottom and was outfitted with a two-blade paddle-type impeller. Despite these discrepancies in geometries, the value of the power function was determined from the Reynolds number and a graph given by Rushton *et al.* The specific power input was then calculated using Equations (3-42) through (3-44).

An estimate of the minimum impeller rotation rate that was required to completely suspend the sulfur crystals was made by using an equation from Zwietering (1958):

$$N_m = S\,\nu^{0.1}\,L_m^{0.2}\,W^{0.13}\,(g(\rho_S - \rho_L)/\rho_L)^{0.45} \,/\, D_i^{0.85} \qquad (3\text{-}45)$$

where: L_m = maximum size of suspended particles (m)

N_m = minimum rotation rate of impeller to just suspend particles (sec^{-1})

S = complete suspension parameter [= fxn (geometry)]

W = weight percent solids in solution

ν = kinematic viscosity of liquid (m^2/sec)

ρ_S = density of solid particles (kg/m^3)

As was the case for the computations to calculate the impeller power input, the geometry of the experimental apparatus used in this study was different than that used by Zwietering. The major difference between the two studies is the geometry of the bottom of the tanks: Zwietering used a flat-bottom tank while the tank used in this study had a curved bottom. The value of the complete suspension parameter (S) was computed from the geometry of the experimental crystallizer and a figure in Zwietering's work. The value of the complete suspension parameter was S = 4.2. The calculation of the minimum impeller rotation rate, required to completely suspend the crystals of size L_m in a solids concentration of W, was performed and used as a guide for the impeller speeds in the experimental runs.

The results from the impeller power input calculations were used as inputs for the determination of the constants in the crystallization kinetics expression. The kinetics expression used to study the effect of power input was the product of $\rho_C k_V/M_T$ and

Equation (3-8), where the dependence on slurry density was neglected (j = 1):

$$(B^0 \rho_C k_V / M_T)/G^i = k_N \rho_C k_V \, \epsilon^h \tag{3-46}$$

The variables in Equation (3-46) are in the same form as the data produced from the experimental runs, namely the specific nucleation rate. The specific nucleation rate and growth rate were combined and placed on the left-hand side of Equation (3-46) because the residence time was not varied. The value of i used in Equation (3-46) was obtained from the previous studies where residence time was varied. A least-squares regression was performed on the log of Equation (3-46) to determine the values of h and $k_N \rho_C k_V$. The value of k_N was computed assuming ρ_C = 2070 kg/m^3 and $k_V = \pi/6$. The value of h from the regression was compared to the values of h obtained from Equations (3-27), (3-28), and (3-29).

3.5.3.4 Variable Water Concentration in the Solvent

The dependence of the crystallization kinetics on the water concentration in the solvent was determined from crystallization runs where both water concentration in the solvent and residence time were varied. A method was required to determine the water concentration in the process solvent because the slurry density is dependent on water concentration. Since the solvent, Triglyme, is hygroscopic and very hard to dry free of water, the calibration curve that was constructed to determine the relationship between the measured water/heptane weight ratios and the gas chromatograph water/heptane peak area ratios was also used to determine the initial water concentration in the "clean" Triglyme used in the calibration standards. The calibration was formulated by assuming the measured water/heptane weight percent ratio was directly proportional with the gas chromatograph water/heptane peak area ratios:

$$w_w/w_h = R\,(A_w/A_h) \tag{3-47}$$

where: A_h = heptane peak area from gas chromatograph

A_w = water peak area from gas chromatograph

R = ratio multiplier between measured values and gas chromatograph

w_h = weight percent heptane in sample

w_w = weight percent water in sample

The water residing in the calibration standards originated from two sources: the "clean" Triglyme and the water added to the Triglyme. The two sources were expressed as:

$$w_w = w_t + w_a \tag{3-48}$$

where: w_a = weight percent water in sample which was added

w_t = weight percent water in sample from clean Triglyme

Equation (3-48) was substituted into Equation (3-47) and the result rearranged to give an expression which was explicit with respect to the weight percent water added:

$$w_a = R\,(A_w w_h / A_h) - w_t \tag{3-49}$$

The data produced from the calibration standards was cast in the form of Equation (3-49). Equation (3-49) was fit to the data using a least-squares regression to compute the slope and intercept. The slope was equated to the ratio multiplier (R) and the intercept to the negative of the weight percent water residing in the "clean" Triglyme (w_t). Equation (3-49) was then used to compute the water concentration in the unknown, the process solvent, where no water was added:

$$w_t = R\,(A_w w_h / A_h) \tag{3-50}$$

The Triglyme used to prepare the calibration standards was dried of water to the extent that the water concentration was far less (< ten percent) than that anticipated, and subsequently computed, for the process solvent.

Using the data of water concentration in the process solvent, the concentration of sulfur in the inlet and outlet streams was computed from the sulfur solubility expression presented in Chapter 2. The slurry density for the MSCPR model was calculated from Equation (3-40). The results from the slurry density calculations were then used as inputs for the determination of the constants in the crystallization kinetics expression. The kinetics expression used was Equation (3-41), the same as that used

for the variable slurry density study. After Equation (3-41) was linearized by taking the log of both sides, a multiple variable least-squares regression was performed to determine the values of i, j-1, and $k_N \rho_C k_V$. The value of k_N was computed assuming ρ_C = 2070 kg/m^3 and $k_V = \pi/6$. The values of i, j, and k_N and the log-log plot of the experimental specific nucleation rate and growth rate from the variable water concentration runs were compared to that from the variable slurry density runs to ascertain any effect the water concentration had on the crystallization kinetics.

The residence time and mass-average particle size data, observed from the experimental runs, were plotted in groups according to their water concentration. The design equation for the MSCPR model was used in the manner discussed in Section 3.5.3.2, along with the constants produced from the above multiple variable regression, to generate curves which were plotted with the experimental data. The curves and experimental data were compared to check the design equation's ability to predict the residence time needed to produce a desired mass-average particle size and slurry density (a design case). The curves and experimental data from the variable water concentration runs were also compared to that for the variable slurry density runs.

Finally, the crystal-size distributions for the experimental runs were predicted from the MSCPR design equation and from the fitted constants for variable water concentration from Equation (3-41). The residence time was used as an input to the design equation, where the dependence of the impeller power input was ignored. The growth rate and specific nuclei population density were calculated in the manner discussed in Section 3.5.3.2 (an operating case). From the growth rate and specific nuclei population density, the crystal-size distribution was plotted and then compared to the distribution observed from the experimental runs.

3.6 Back-Mixed Crystallizer Results and Discussion

The results of the thermal crystallization of elemental sulfur from Triglyme in a

back-mixed experimental crystallizer are discussed below. The discussion is divided into five sections. First, the applicability of the two crystallizer models, namely the MSMPR and MSCPR models, to the experimental results is analyzed. The four subsequent sections discuss the dependence of the crystal-size distribution on residence time, slurry density, impeller power input, and water concentration. The ultimate determination of the crystallization kinetics of the sulfur/Triglyme system is also presented in each section.

3.6.1 Experimental Crystal-Size Distribution

3.6.1.1 Application of the Ideal Crystallizer Model

A typical crystal-size distribution of the sulfur produced from the experimental crystallizer is shown with the unconstrained and constrained MSMPR models in Figure 3.7. The unconstrained MSMPR model, Equation (3-31), was fitted using a least-squares regression to the experimental data in Figure 3.7 to yield the specific nuclei population density and growth rate. These values satisfy only the population balance. The constrained MSMPR model, Equation (3-34), was then fitted to the data. An objective function, composed from Equation (3-34), was derived using a least-squares criterion. The objective function was reduced to a recursion relation, where an initial guess for the growth rate was provided from the unconstrained MSMPR model. The benefit of the constrained MSMPR analysis is that it requires the fitted crystal-size distribution parameters ($n^0\rho_C k_V/M_T$ and G) to satisfy both the population balance and mass balance expressions, and therefore yields the best estimates of $n^0\rho_C k_V/M_T$ and G for the MSMPR crystallizer model.

The comparison of the constrained MSMPR model with the experimental crystal-size distribution in Figure 3.7 shows that the data exhibit the general semi-log trend predicted by this idealized model. However, a distinct "knee" in the experimental distribution is present, which divides the distribution into two regions. The unconstrained MSMPR model lies well below the constrained MSMPR model,

indicating that the observed crystal-size distribution from the experimental run does not satisfy the total mass expression for the MSMPR model (Equation (3-33)). This disparity is attributed to the systematic deviation of the experimental data from the MSMPR model, where fewer of the large crystals are observed than the MSMPR model estimates. This disparity is also observed when comparing the mass-average particle size measured by the particle-size analyzer to that calculated from the MSMPR model using Equation (3-7), both listed in Table 3.1. The MSMPR model overestimates the observed mass-average particle size by 33 percent. Again, this overestimation is the result of the presence of the "knee" in the crystal-size distribution, where fewer large crystals are present than the MSMPR model estimates.

3.6.1.2 Application of the Modified Crystallizer Model

Since the sulfur crystals were observed settling out of the active volume of the experimental crystallizer, a mechanism was identified which explained the deviation of the observed crystal-size distributions from the simple MSMPR crystallizer model. The preferential removal of the larger crystals from the experimental crystallizer is similar to the operation of the MSCPR crystallizer, shown schematically in Figure 3.2. In both the experimental and MSCPR crystallizers, crystals whose size is larger than some critical size (L_c) are removed at a finite rate from the active volume of the crystallizer. For the MSCPR crystallizer shown in Figure 3.2, the over-sized crystals (those larger than L_c) are removed by a cyclone. The value of L_c is determined by manipulating the performance of the cyclone and is independent of the operation of the crystallizer. In the experimental crystallizer, the larger crystals settled out of the flow near the exit port. Unlike the cyclone, the value of L_c for the experimental crystallizer was determined by the hydrodynamics within the crystallizer and the settling velocity of the sulfur crystals in the mother liquor. Therefore, the value of L_c could not be independently controlled. The value of the MSCPR parameter z is defined as the ratio of the residence times of the under-sized and over-sized crystals

(Equation (3-11)). Again, z is controlled independently for the crystallizer in Figure 3.2 but was determined from the hydrodynamics within the experimental crystallizer.

Figure 3.8 shows the MSCPR model with the same crystal-size distribution as in Figure 3.7. The unconstrained MSCPR model, Equations (3-35), was fitted to the data to yield values of the specific nuclei population density, growth rate, and z. The constrained MSCPR model, Equations (3-37), was then fitted to the data. An objective function was formulated from Equations (3-37) and a least-squares criterion. The objective function was minimized, where initial guesses for the growth rate and z were provided from the unconstrained MSCPR model. In Figure 3.8, the unconstrained MSCPR model is very close to the constrained MSCPR model, indicating that the observed crystal-size distribution from the experimental run nearly satisfies the total mass expression for the MSCPR model (Equation (3-36)). Comparing the MSCPR model with the experimental data in Figure 3.8, this more complex model fits the data much better than the idealized model. The location of the "knee," the critical particle size (L_c), was assigned a value of 250 μm. The location of the "knee" at approximately 250 μm was invariant for all of the runs performed in this study.

The growth rate for the MSCPR model in Table 3.1 is markedly larger than that for the MSMPR model, as predicted in Section 3.2.3, because of the preferential removal of larger crystals. Comparing Figures 3.7 and 3.8, the slope of the distribution of the under-sized crystals (those smaller than L_c) for the MSCPR model is less than the slope of the distribution of the full range of crystal sizes for the MSMPR model. Since the growth rate is inversely proportional to the slope, the growth rate is larger for the smaller slope exhibited by the MSCPR plot. Comparing the calculated mass-average particle sizes from the two models to the measured mass-average particle size produced from the experimental crystallizer, the MSMPR value grossly overestimates the observed mass-average particle size, whereas the MSCPR

value is 1.5 percent less the observed mass-average particle size. Discussed later in Section 3.6.3, the agreement between the experimentally observed slurry density and that predicted from the MSCPR model is poor. The disparity between these slurry densities is attributed to several experimental factors and is not a result of a deficiency in the MSCPR model. The conclusion from these results is that the MSCPR model is superior to the MSMPR model in simulating the experimental crystallization runs.

In the more complex MSCPR model, the internal classification (the preferential removal of large crystals from the crystallizer) was isolated from the crystallization kinetics of the sulfur/solvent system by mathematically expressing the classification mechanism in the population balance. Furthermore, the additional parameters used in the MSCPR model (z and L_c) had physical identities for the experimental crystallizer. For the MSCPR crystallizer model, the slope and intercept of the distribution of the under-sized crystals are indicative of the true crystallization kinetics of the system, whereas the slope of the distribution of the over-sized crystals combines the effects of the crystallization kinetics and the classification mechanism. In comparison, applying the MSMPR model to the full range of crystal sizes yields a slope and intercept that represent the interaction of the crystallization kinetics and the classification mechanism and are unique to the experimental crystallizer. As a result, the true kinetic behavior of the sulfur/solvent system is not isolated from the internal classification mechanism. Therefore, the MSCPR crystallizer model was used to interpret the data and to determine the dependence of the crystallization kinetics on the operating parameters of the experimental crystallizer. The subsequent crystallization kinetics are independent of the experimental crystallizer. The decoupling of the crystallization kinetics from the particular internal classification observed in the experimental crystallizer will enable the use of the kinetic expression for a crystallizer designed with any type of internal and external flow configuration. The use of the true crystallization kinetics is important in the scale-up to an industrial-size crystallizer because the larger vessel

may have a drastically different external flow configuration and different internal hydrodynamics.

3.6.1.3 Verification of the Crystallizer Model Assumptions

The fact that the location of the "knee" in the crystal-size distribution remained constant from run to run lends credence to the assumptions made to formulate the MSCPR model, and to its subsequent application to the experimental crystallizer where large crystals were observed to settle out of the active crystallizer volume through its exit port. Another assumption that is verified from the observed crystal-size distribution is that no significant agglomeration or breakage of crystals occurred in the crystallizer since the distribution does not exhibit any peaks or modes which would represent the presence of agglomerates or fragments. In addition, no adverse effects on the crystal-size distribution (such as classification, breakage, or agglomeration) appear to arise from the crystallizer sampling technique. The assumption of size-independent growth is also verified since the crystal-size distribution does not show any appreciable non-linear trends in the semi-log plots, such as those observed for solute/solvent systems which exhibit size-dependent growth (Abegg *et al.*, 1968; Canning and Randolph, 1967). No instabilities or continuous oscillations were observed while operating the experimental crystallizer. Such behavior is oftentimes seen in a classified-product removal crystallizer operating under certain conditions (Randolph *et al.*, 1977).

3.6.2 Dependence of Crystal-Size Distribution on Residence Time

The effect of residence time on the crystallization kinetics and the subsequent crystal-size distribution was studied using eighteen experimental runs where the residence time in the crystallizer was varied from 4.00 to 67.3 minutes. The crystallizer volume and crystallizer feed temperatures were held constant at 30° and $50^{o}C$, respectively, to provide a change in sulfur solubility in the process solvent of

2.99 kg/m^3. The sulfur solubilities in the crystallizer volume and crystallizer feed were estimated using the sulfur solubility correlation in Chapter 2. Three typical crystal-size distributions of different residence times and their corresponding constrained MSCPR plots are illustrated in Figure 3.9. The MSCPR plots, produced by fitting Equations (3-37) to the experimental data and obtaining the values of the specific nuclei population density, growth rate, and z, agree well with the experimental distributions. The specific nuclei population density increases and the mass-average particle size decreases with decreasing residence time, satisfying the trends suggested in Section 3.2.4 for a kinetic order (i) greater than one. The crystal-size distributions for runs with residence times larger than 40 minutes showed concave-downward deviations from the linear distribution of crystal sizes less than L_C. This deviation is not thought to be a size-dependent growth phenomenon since the larger particles in the distribution were not affected. The deviation may be a further complication of the internal classification of the experimental crystallizer.

The results of the constrained MSCPR analysis of the experimental data are tabulated in Appendix B. The fitted parameters for the MSCPR model, specific nuclei population density ($n^0\rho_C k_V/M_T$), growth rate (G), and z were used to calculate the specific nucleation rate ($B^0\rho_C k_V/M_T$) and the mass-average particle size ($\mathscr{L}$) using Equations (3-32) and (3-17), respectively. The two "specific" variables ($n^0\rho_C k_V/M_T$ and $B^0\rho_C k_V/M_T$) were calculated in this form because of the manner in which the crystal-size distribution data were produced from Equation (3-30). No measurement or calculation of the slurry density (M_T) was made to compute the "specific" variables from the "raw" variables (n^0 and B^0). The calculated values of the mass-average particle size from Equation (3-17) deviated no more than seven percent from those values measured by the particle-size analyzer.

3.6.2.1 Determination of the Kinetic Constants

The specific nucleation rate and growth rate data from the constrained MSCPR

model were cast in the form of Equation (3-38) to determine the kinetic constants for the crystallization of sulfur from the process solvent. The results of the regression of Equation (3-38) are shown in Figure 3.10 and tabulated in Table 3.2. In Figure 3.10, the specific nucleation rate and growth rate both increase with decreasing residence time. The data correlate well for Equation (3-38) over a large range in residence time. Of the two kinetic constants in Equation (3-38), the kinetic order (i) is of most interest because it determines the ultimate dependence of the mass-average particle size on residence time, as indicated by Equation (3-19). Since the value of i is greater than one, the mass-average particle size increases with increasing residence time (see Equation (3-23)). This was indeed observed in the experiments and is illustrated in Figure 3.11, where the mass-average particle size measured by the particle-size analyzer is plotted against residence time. The mass-average particle size data lie between 200 and 300 μm and show that a large increase in residence time is required to produce a significant increase in mass-average particle size. The data in Figure 3.11 are cast in the form of Equation (3-23), providing another method to calculate the kinetic order. The application of Equation (3-23) to the mass-average particle size versus residence time data, measured during the experiments, yielded a value of i = 1.36. Although Equation (3-23) was derived from the MSMPR model, the value of i produced from it agrees well with that obtained using Equation (3-41), which is 1.42. The agreement in the values of i, derived from both experimentally observed variables ($\mathscr{L}$ and τ) and fitted parameters from the crystal-size distribution ($B^0\rho_C k_V/M_T$ and G), lends confidence to the value of the kinetic order.

3.6.2.2 Dependence of Model Parameters on Residence Time

The location of the "knee" at approximately 250 μm was invariant for all of the runs performed in this study. The best estimate of the critical particle size, L_C, was quantitatively determined by comparing the measured mass-average particle size values from the experimental crystallizer to those calculated values from the MSCPR model.

Minimizing the sum of the squares of the differences in average size for all of the experimental runs yielded a value for L_c of 275 μm. Although this value was mathematically the best fit of the data, the value was not compatible with the location of the "knee" observed in the crystal-size distributions. Since the location of the "knee" was close to 250 μm for each experimental run, that value was selected for L_c for the rest of the study.

The dependence of the MSCPR parameter z on residence time was investigated so that it may be incorporated into the design equation. Figure 3.12 shows the effect of residence time on z, where no clear trend is observed. The MSCPR parameter was therefore assumed independent of residence time and an average value of z computed: $z = 3.13 \pm 0.14$. The ramification of the independence of z on residence time is illustrated by examining Equation (3-11): $R = (z-1)\ Q_2$. Finding a constant value of z means that the effective recycle flow rate (R) is directly proportional to the throughput flow rate (Q_2). For the experimental crystallizer, R is the mathematical analog of the settling of large crystals through the exit port. The rate of large crystals being removed from the active volume of the crystallizer was determined by the frequency of actuating the valve. As a result, the fictitious recycle rate was not controlled independently and must have varied with residence time. Although the dependence of R on Q_2 cannot be predicted from what was observed during the experiments or from the framework of the MSCPR model, the value of R is certainly dependent on residence time. Since the value of z showed no clear trend over the range of residence times studied and since the value of L_c was invariant, the MSCPR model has two variable parameters (G and $n^0\rho_C k_V/M_T$) and two constant parameters ($z = 3.13$ and $L_c = 250$).

The value of z from the preceding analysis is a result of the particular geometry of the experimental crystallizer used in this study. When scaling the crystallizer to a larger size, to pilot-plant scale for example, the larger crystallizer may also exhibit

internal classification. The MSCPR model may be used to obtain the crystallization kinetics of the sulfur/solvent system, but the value of z is not required to be 3.13. The effect of scale on z may be determined from experimental runs in the larger crystallizer. If the crystallizer has no classification, then the value of z is unity and the idealized crystallizer model may be used to study the crystallization kinetics.

3.6.2.3 Application of the Crystallizer Model with Constant Z

To test the MSCPR model with constant z, the average value of z was used to reconstruct the MSCPR plots for the eighteen runs. The constrained MSCPR model (Equations (3-37)) with constant z and L_c were fitted to the crystal-size distributions from the experimental runs to produce new values of $n^o \rho_c k_v / M_T$ and G. The plots produced from the average z and those produced from the fitted z were compared and gave satisfactory results. Figure 3.13 shows a typical crystal-size distribution with the MSCPR plot for constant z equal to 3.13 and with the MSCPR plot for fitted z. The disparity between the fitted-z plot and the average-z plot increased as the value of fitted z was farther removed from the average value of z. Figure 3.13 shows the run where the fitted z was farthest from the average value of z (4.49 versus 3.13). The other runs had plots from the constant-z analysis which fit the crystal-size distribution data much better than the fit exhibited in Figure 3.13. The specific nucleation rate and growth rate data from the constant-z MSCPR analysis were plotted in the form of Equation (3-38) to determine the effect of the use of the average value of z on the kinetic constants (i and k_N). The result of plotting the kinetic rates derived from the average value of z, shown in Figure 3.10, was to smooth the data and shift the position of the regressed line slightly. The kinetic constants for average z, listed in Table 3.2, are comparable to the previously determined values. The kinetic order (i) increased by ten percent from the value derived from the fitted-z analysis. From the scatter of the data in Figure 3.10 and from the small change in the values of the kinetic constants, the use of the average value of z for the determination of the kinetic constants has

little effect on interpreting the data. Thus, the average value of z proved to be acceptable in characterizing the experimental distributions for the range of residence times studied. The benefit of using a constant value of z is realized in using the design equation to predict the residence time or mass-average particle size.

3.6.2.4 Sensitivity of the Design Equation to the Critical Particle Size and Z

The residence time of the crystals in the crystallizer is a fundamental design or operating parameter for the crystallizer. Similarly, the mass-average particle size is a parameter derived from the crystal-size distribution which is easy to conceptualize, adequately characterizes the crystal-size distribution, and is of great utility when designing or operating downstream solids/liquid processing equipment. As a result, the design equation was formulated with these two variables to aid in the design or simulation of the crystallizer. The values of the kinetic order (i), kinetic constant (k_N), average z, and L_c were used in the design equation, Equation (3-19), to ascertain the ability of the model to predict the residence time required to produce a desired mass-average particle size. The experimental data and design curve are plotted as mass-average particle size versus residence time to provide ease of use in calculating the mass-average particle size produced from a crystallizer with a residence time of τ or in calculating the residence time required to produce sulfur crystals with a mass-average particle size of $\mathscr{L}$. Figure 3.14 shows the results from the design equation where i = 1.54, k_N = 0.562, z = 3.13, and L_c = 250. The MSCPR design equation adequately predicts the data from the experimental crystallizer when comparing its curve to the experimental data. The design curve in Figure 3.14 also shows that there is a decreasing incremental payoff in mass-average particle size for increasing the residence time.

An analysis of the sensitivity of the MSCPR design equation to the value of z is shown in Figure 3.15. The ability of the design equation to accurately predict the experimental data is highly dependent on the value of the MSCPR parameter z. The

use of the average value of z in the design equation is warranted when comparing its curve to the curves generated from other values of z. The same type of sensitivity analysis was also made for the value of the critical particle size (L_c) for values ranging from 230 to 290 μm. The results of the analysis indicated that the design curves from the design equation were relatively insensitive to L_c. Finally, the values of i, k_N, average z, and L_c were used to predict plots of the crystal-size distributions for the eighteen runs and then compare them to the experimental crystal-size distribution data. The agreement between the predicted plots and the experimental data was similar to that shown in Figure 3.13. The error between the predicted and measured mass-average particle sizes was no more than six percent for the eighteen runs studied. As a result, the MSCPR model appears acceptable for characterizing the crystallization of sulfur in the experimental crystallizer and was therefore used to obtain the crystallization kinetics from the variable residence time data.

3.6.3 Dependence of Crystal-Size Distribution on Slurry Density

The effect of slurry density on the crystallization kinetics was determined from nine experimental runs where the temperatures of the sulfur-saturated crystallizer feed solution were 40°, 50° and 60^oC with residence times of 4, 16, and 45 minutes. The temperature of the crystallizer remained constant at 30^oC. The drop in temperature from the feed stream to the temperature in the crystallizer volume reduced the sulfur solubility in the process solvent to produce sulfur crystals. The change in sulfur solubility is expressed by Equation (3-39) and calculated from the temperatures of the crystallizer and feed using the sulfur solubility correlation in Chapter 2. The change in sulfur solubilities were 1.23, 2.99, and 5.52 kg/m^3, corresponding to the feed temperatures of 40°, 50°, and 60^oC, respectively. The crystal-size distributions and their corresponding MSCPR plots are shown in Figure 3.16, where the distributions are grouped by residence time to show the effect of variable solids concentration. The specific nuclei population density is observed to decrease with increasing slurry

density. In addition, the slope of the distributions of the under-sized crystals decreases with increasing slurry density, indicating that the growth rate increases with increasing slurry density. These trends are in line with those suggested in Section 3.2.5 for a value of the slurry density exponent (j) that is less than one. The distributions of the smallest particles were slightly different than those of previous runs because the sensor lamp for the particle-size analyzer burned out and had to be replaced. Since the smallest mono-sized microspheres that were used to recalibrate the particle-size analyzer were 31.2 μm (instead of the 19.73 μm spheres used for the previous runs), the specific population densities of the crystals of sizes less than 31.2 μm (the first two points) are suspected of larger error than those of sizes within the range of the calibration standards.

The results of the constrained MSCPR analysis on the variable slurry density data are listed in Appendix B. The three fitted parameters for the MSCPR model, specific nuclei population density, growth rate, and z, were used to compute the specific nucleation rate and the mass-average particle size using Equations (3-32) and (3-17). The two "specific" variables ($n^0\rho_C k_V/M_T$ and $B^0\rho_C k_V/M_T$) were calculated in this form because of the manner in which the crystal-size distribution data were produced from Equation (3-30). No measurement or calculation of the slurry density (M_T) was made to compute the "specific" variables from the "raw" variables (n^0 and B^0). The calculated values of the mass-average particle size from Equation (3-17) deviated no more than seven percent from those values measured by the particle-size analyzer.

In the previous variable residence time study, the slurry densities were neither measured nor calculated. In this variable slurry density study, the slurry densities measured from the experiments and those calculated from the MSCPR analysis using Equation (3-40) are tabulated in Table 3.3. The values of the variables required to calculate the slurry density using Equation (3-40) were taken from the data in Appendix B. The maximum slurry density was calculated from the difference in

sulfur solubilities in the crystallizer feed and crystallizer effluent using the correlation in Chapter 2 and Equation (3-39). This maximum slurry density was compared to the slurry density measured from each experimental run and to the slurry density calculated from the MSCPR model using Equation (3-40). The consequence of the preferential removal of large particles is very apparent. The internal classification mechanism produced a fifty-percent reduction in the solids concentration from the maximum value. The experimentally observed slurry densities show no general trends and are not in good agreement with the calculated values from the MSCPR model.

The discrepancies between the calculated and observed slurry densities are a result of the inability to accurately measure the slurry density in the active volume of the crystallizer. The measurement of the slurry density from the experimental crystallizer was very difficult for such small solids concentrations because the solids were removed from the mother liquor by vacuum filtration and the weight of the solids determined by difference with the weight of the filter paper. Since large filter papers were required to provide rapid filtration, the weight of the paper was the same order of magnitude as the solids collected. Once the sulfur crystals were separated from the mother liquor, the crystals and paper was dried so that the total weight did not include any residual mother liquor or washing fluid. The drying of the sulfur was difficult because the solvent is relatively nonvolatile (*b.p.* = 216°C) and the sulfur has a low melting point (*m.p.* = 113°C). As the temperature was increased to remove the solvent, the vapor pressure of the sulfur also increased. Consequently, some of the sulfur may have been lost while ridding the sample of residual solvent. When larger slurry densities were measured from the high-temperature feed runs, the sulfur cake was extremely difficult to dry free of solvent and washing fluid. As a result, the observed slurry densities are larger than those predicted from the MSCPR model.

The disparity between the calculated and observed solids concentrations may also be a result of the crystallizer feed solution not being fully saturated with sulfur at the

temperature of the solvent holding tank. If the process solvent leaving the solvent holding tank was not saturated with sulfur, then the sulfur solubility correlation from Chapter 2 would overestimate the sulfur concentration (based on the temperature of the feed stream leaving the solvent holding tank). The spectroscopic method used in Chapter 2 to determine the sulfur concentration in the solvent was not used here because impurities in the process solvent interfered with the absorbance peak of the dissolved sulfur. In addition, the maximum solids concentration produced in the experimental crystallizer would be less than if the process solvent left the solvent holding tank saturated with sulfur. As a result, the maximum solids concentration calculated from the the estimated sulfur solubilities in the crystallizer feed and effluent streams would be greater than the actual value. The disparity between the calculated and observed values of the slurry density would be most severe for the lower-temperature feed runs. A difference in 1°C between the feed temperature and the sulfur saturation temperature would contribute a large error relative to the 10°C temperature change of the solvent in the crystallizer for the 40°C feed. For the higher-temperature feed runs, a 1°C temperature difference would have a smaller error relative to the 30°C temperature change for the 60°C feed.

3.6.3.1 Determination of the Kinetic Constants

The constrained MSCPR specific nucleation rate and growth rate data were plotted in groups of constant crystallizer feed temperature, as shown in Figure 3.17, to determine the kinetic constant (i). The slopes for each solids concentration should be the same, as predicted by Equation (3-41), but the scatter of the data yielded slightly different slopes. As in the previous variable residence time study, the rates of nucleation and growth both increase with decreasing residence time while the slurry density is constant. Using Equation (3-41) and the slopes of the three curves, the average value of i was computed to be 1.65, whereas the value of i for the MSCPR model (with variable z) from the previous variable residence time study was 1.42. The

value of i was also estimated from the effect of residence time on the crystallization kinetics by using Equations (3-21) through (3-23). Table 3.4 lists the results of computing i, where the value produced from the two experimentally measured variables ($\mathscr{L}$ and τ) is 1.31. The values of i computed from the fitted MSCPR variables are significantly different from 1.31 because of the scatter of the raw data and because Equations (3-21) through (3-23) were derived from the MSMPR model. Therefore, the value of i provided from the plot of mass-average particle size versus residence time is the most reliable.

The value of the slurry density exponent (j) in the kinetics expression was estimated from the dependence of the crystallization kinetics on slurry density as described by Equations (3-24) through (3-26), assuming i = 1.31. Again, Equations (3-24) through (3-26) were derived from the MSMPR model and are therefore used only to lend support to the value of j computed from the MSCPR model. Equation (3-26) is illustrated graphically in Figure 3.18, where the two experimentally measured variables, mass-average particle size and slurry density are grouped by residence time to show the effect of residence time also. The slopes of the curves decrease with decreasing residence time, indicating that the mass-average particle size increases with increasing slurry density for large residence times, but that the mass-average particle size decreases with increasing slurry density for small residence times. Since the MSCPR model does not predict this behavior , the slopes of the three curves were averaged to compute the value of j in Equation (3-26). The precision of the calculated value of j is poor because the slopes of the lines in Figure 3.18 vary significantly. In addition, the precision of the value of j computed from Equations (3-24) through (3-26) is compromised by the small range of slurry densities studied and the corresponding small change in the MSCPR model variables (G, $n^0\rho_C k_V/M_T$, and $\mathscr{L}$). Hence, the estimated values of j, listed in Table 3.5, are scattered over a large range. However, the value of j from the plot of mass-average particle size versus

slurry density is in line with what is usually observed from secondary nucleation kinetics -- a value near unity.

3.6.3.2 Dependence of Model Parameter Z on Slurry Density

The dependence of z on residence time and solids concentration is shown in Figure 3.19, where the abscissa and ordinate are the same as those in Figure 3.12. Although the average value of z is 1.98 ± 0.18 for the nine experimental runs, some unexpected trends are observed. The value of z is dependent on residence time and is also dependent on the solids concentration. The change in value of z from 3.13, observed in the previous variable residence time study, to a value of 1.98 in this study may be a result of the different fines' distributions produced from the change in the particle-size analyzer calibration. However, the cause of the smaller average value of z is probably the result of so little solids residing in the crystallizer for the runs made with the 40°C feed temperature. As indicated in Table 3.3, the slurry densities were abnormally low for the 40°C runs and may be a result of the feed not being fully saturated at the feed temperature (discussed earlier) or of unrelieved supersaturation in the crystallizer volume (Class I behavior). The values of z for the runs with higher feed temperatures (50° and 60°C feeds) are more in line with the scatter of data observed from the previous variable residence time runs shown in Figure 3.12. The agreement of these values of z from the higher feed temperature runs supports the argument that the results from the runs with 40°C feeds are somewhat erroneous.

3.6.3.3 Application of the Crystallizer Model with Constant Z

The new average value of z was used to investigate the viability of the MSCPR model to represent the experimental data. The crystal-size distribution data from the variable slurry density runs were re-analyzed using the constrained MSCPR model and the average value of z = 1.98. Values of i and j were again determined for z = 1.98 (using Equations (3-21) through (3-26)) and are listed in Tables 3.4 and 3.5. Using

the data produced from the average value of z reduced the scatter of the values of i and j. The resulting specific nucleation rate and growth rate data ($B^o\rho_C k_V/M_T$ and G) were combined with the solids concentration values observed from the experiments (M_T(obs)) to determine the kinetic constants (i, j, k_N) in Equation (3-41). The results of the multiple variable regression are listed in Table 3.6. The value of i (1.55) is close to the values provided from the average of the slopes of the curves in Figure 3.16 (i = 1.65) and from the variable residence time study when z = 3.13 shown in Figure 3.10 (i = 1.54). The value of j (0.943) is close to the value produced from the dependence of the mass-average particle size on slurry density shown in Figure 3.18 (j = 0.938). The agreement of the values of i, which were produced from both experimentally observed parameters and from fitted variables, and the agreement of the values of j which were similarly produced lends confidence to the values of these variables. The value of j determined from this study is very close to unity, which is observed for many crystallization systems (Garside and Shah, 1980).

3.6.3.4 Prediction of the Experimental Data from the Design Equation

The values of i, j, k_N, average z, and L_C were used in the MSCPR design equation to predict the residence time required to produce a desired mass-average particle size from a change in the solute solubility in the crystallizer feed and effluent streams. The experimental data of mass-average particle size versus residence time are shown in Figure 3.20, along with the predicted curves for each temperature of the crystallizer feed. The experimental data for the 40°C-feed runs show a trend much different than those of the 50°- and 60°C-feed runs. This difference is attributed to deficiencies of the experimental apparatus, which are discussed in Section 3.6.3. The MSCPR design equation exhibits the overall trend of the experimental data, but slightly overestimates the mass-average particle size for a given residence time. Judging from the effect of z on the design equation in Figure 3.15, a higher z is required. The average value of z was computed for the 50°- and 60°C-feed data only and yielded a value of 2.25.

This value was also used in the MSCPR design equation to try to compensate for the erroneous effects of the $40^{o}C$-feed data. The curves produced from the MSCPR design equation with z = 2.25 fit the data much better than that with z = 1.98. The MSCPR design equation curve also shows that little change in mass-average particle size occurs when the slurry density is changed.

Finally, the crystal-size distributions were predicted, using the values of i, j, k_N, average z, and L_c, from the residence times and change in sulfur solubilities (maximum solids concentrations) of the experimental runs. Refer to Table 3.7 for a summary of the predicted slurry densities and mass-average particle sizes and their comparison to the observed data. In general, the predicted plots and the predicted mass-average particle sizes compared well with the observed crystal-size distributions, except where the observed value of z deviated far from the value of 2.25. The maximum error observed between the predicted and measured values of the mass-average particle size for the nine runs was nine percent. When considering only the 50°- and $60^{o}C$-feed runs, the maximum error was much better (four percent), because of the better agreement between the constant-z value and the runs' fitted z values.

3.6.4 Dependence of Crystal-Size Distribution on Impeller Power Input

The effect of impeller power input on the crystallization kinetics was studied from three experimental runs where the crystallizer impeller was rotated at three rates: 215, 350, and 680 RPM. The residence time for all three of the runs was approximately 12.3 minutes, and the crystallizer feed and crystallizer temperatures were 50° and $30^{o}C$, respectively. These temperatures provided a maximum slurry density equal to those of the runs in the variable residence time study, *i.e.* 2.99 kg/m^3. The impeller was rotated clockwise to provide downward flow from the impeller in the first two runs but was rotated counter clockwise to give upward flow in the last run. The minimum and maximum rotation rates for a particular crystallizer are usually dictated by the physical attributes of the apparatus and the solute/solvent system. The

minimum rotation rate is that necessary to completely suspend all of the crystals in the crystallizer volume and to maintain a well-mixed suspension throughout the volume. Failure to completely suspend the crystals produces stratification where only small crystals reside in the upper portion of the crystallizer, thereby reducing the crystal surface area needed for crystal growth. The determination of the minimum rotation rate for the experimental crystallizer is discussed below. The maximum rotation rate is typically set by the need to eliminate vortex formation and air entrainment. The experimental crystallizer had no baffles to aid in mixing because of sulfur encrustation problems. As a result, bulk rotation of the fluid persisted in the crystallizer. A sizable vortex (~2.5 cm) was present at the top of the fluid interface when the impeller was rotated at 680 RPM, but there was no entrainment of air. Only a small vortex (~3 mm) was observed when the impeller was rotated at 215 RPM.

3.6.4.1 Minimum Impeller Rotation Rate

The minimum impeller rotation rate (215 RPM) was experimentally determined to be the minimum rotation rate required to completely suspend the sulfur crystals in the mother liquor. The criterion for this minimum rotation was the same as that used by Zwietering (1958), where complete suspension was defined as crystals residing on the bottom of the crystallizer for no more than two seconds before being whisked back into the active crystallizer volume. In addition, the minimum rotation rate was required to provide a homogeneous slurry throughout the active volume. The homogeneity of the active volume was determined visually, where dead zones or areas with few particles were nonexistent in the upper portion of the tall, slender experimental crystallizer. The minimum impeller rotation rate for complete suspension was also calculated from Zwietering's correlation, Equation (3-45). The calculated rotation was 525 RPM for 600-μm crystals, the largest crystals to reside in the crystallizer, and 420 RPM for 200-μm crystals, the approximate dominant crystal size of the experimental crystal-size distributions. These calculated minimum impeller

rotation rates are much larger than that measured from the experimental crystallizer (215 RPM). Although Zwietering stated that the minimum rate of rotation was independent of the type of tank bottom, the rounded bottom of the crystallizer in this study certainly reduced the minimum rotation rate required to completely suspend the sulfur crystals.

3.6.4.2 Effect of Impeller Rotation Rate on Crystal-Size Distribution

The effect of the specific power input on the crystal-size distributions is shown in Figure 3.21. Other than the decrease in specific nuclei population density with increasing power, no clear trend is observed in the change of the distributions for the change in power. The trend of decreasing specific nuclei population density with increasing power is opposite of that prescribed in Section 3.2.6, where a positive value of the exponent of the impeller power input (h) is predicted. From this contradiction in trends, the change in impeller rotation rate is thought to have an effect on the internal classification mechanism in the experimental crystallizer as well as on the nucleation rate of the crystals. The internal classification is altered with changing impeller rotation rate because the flow characteristics near the exit port change with impeller rotation rate. Increasing the agitation increases the momentum of the fluid and crystals flowing around the crystallizer. Although the frequency with which a single crystal comes in contact with the exit port increases, the increased momentum reduces the probability of the crystal settling down the exit port. Referring to Figure 3.21, the location of the "knee" in the crystal-size distributions is invariant (L_c = 250 μm) over the range in rotation rates. Since L_c is constant, the value of z (the ratio of the slopes of the over-sized and under-sized crystals) must change. However, Figure 3.21 shows no clear trend for the value of z.

3.6.4.3 Determination of Impeller Power Input Exponent

The constrained MSCPR model was applied to the experimental crystal-size

distribution data to compute the crystallization kinetics of the three runs. The specific nuclei population density, growth rate, and z were fitted to the crystal-size distribution data using Equations (3-37) and the specific nucleation rate and mass-average particle size were subsequently calculated using Equation (3-32) and Equation (3-17), respectively. The results of the analysis are listed in Appendix B. The value of z for the three runs shows no systematic trend, but shows the same scatter that was observed from previous experimental runs where residence time and slurry density were varied.

The impeller power input was computed from Equations (3-42) through (3-44), as prescribed by Rushton *et al.* (1950). The power input was based on the active volume of the crystallizer and was therefore named the specific power input (watts per kg of solution). The values of the specific power input ranged from 0.0064 to 0.14 W/kg and are listed in Table 3.8. These values were computed from the measured rotation rate of the impeller and from the dimensions of the impeller and crystallizer. The Reynolds numbers for the three rotation rates, calculated from the diameter of the impeller ($ND_i^2\rho_L/\mu$), are also listed in Table 3.8. The values indicate that the flows inside the crystallizer are in the fully turbulent regime. Some of the dimensionless groups calculated for the experimental crystallizer (such as the aspect ratio) were out of the range of those studied by Rushton *et al.* As a result, the calculated values of the specific power input are of uncertain validity. However, the magnitude of the calculated values are in agreement with those reported by Rushton *et al.* and others for the range of impeller rotation rates in this study.

The value of the exponent of the specific power input (h) was estimated from the data produced from the constrained MSCPR analysis and Equations (3-27) through (3-29). The estimates are listed in Table 3.9. The estimates are all less than zero, indicating that the nucleation rate, calculated from the kinetics expression in Equation (3-18), decreases with increasing power input. This trend is illustrated in Figure 3.22, where the dependence of both mass-average particle size and specific

nucleation rate on the specific power input are shown. These data also indicate that the mass-average particle size increases with increasing power, which contradicts the usual trend for most crystallization systems. The specific nucleation rate and growth rate data were also combined with the calculated values of specific power input to determine the value of h. The data were cast in the form of Equation (3-46) and the resulting value of h was -0.170. This value is in agreement with the values computed above from Equations (3-27) through (3-29).

The decrease in nucleation rate with increasing impeller power input is believed to be a result of a change in the internal classification mechanism rather than a direct result of the nucleation rate's dependence on the power input. The nucleation rate typically increases proportionally with increasing power input because more supersaturated clusters or nuclei embryos are exposed to existing crystals and solid surfaces (Clontz and McCabe, 1971). However, in the present experiments the nucleation rate decreases and the growth rate increases with increasing agitation. This dependence of growth rate on power input would usually indicate that crystallization in the solute/solvent system is mass-transfer limited. The crystal growth rate is typically independent of power input for well-mixed vessels (such as the experimental crystallizer used in this study) because the resistance to mass transfer is low. Rao *et al.* (1988) showed that the power number ($P/N^3D_i^5\rho_L$) gradually increases with increasing impeller rotation rate (N) as more and more solids are suspended. The increase of power number with rotation ceases when the suspension of solids is complete, *i.e.*, when the minimum impeller rotation rate to suspend the solids (N_m) is reached. If the impeller rotation rate is increased above the minimum, the additional energy input is not dissipated into suspending more solids but is dissipated by increasing the degree of turbulence in the fluid. Furthermore, once the crystals are completely suspended, the mass-transfer rate increases only slightly with increasing agitation (Kneule, 1956). Since the sulfur crystals were observed to be fully suspended

in the well-mixed experimental crystallizer, the mass-transfer rate is independent of power input.

With the mass-transfer limitation aside, the only explanation for the erroneous effect of impeller power input on nucleation rate is from the change in the classification mechanism. The internal classification in the experimental crystallizer does not allow the separation of the effects of variable impeller rotation rate on the crystallizer hydrodynamics and on the nucleation rate. Since the effect of specific power input on the nucleation rate cannot be isolated from its effect on the crystallizer hydrodynamics, the effect of impeller power input was neglected in the kinetics expression by assigning $h = 0$. To better determine the effect of impeller power input on the crystallization kinetics of the sulfur/Triglyme system, similar experiments should be conducted in a mixed-product removal crystallizer.

3.6.5 Dependence of Crystal-Size Distribution on Water Concentration

The effect of water concentration in the process solvent on the crystallization kinetics was studied from nine experimental runs where the water concentration in the process solvent was varied from zero to five weight percent with residence times of 4, 16, and 45 minutes. The crystallizer feed and crystallizer volume temperatures were held constant at 50° and $30^{o}C$, respectively. The upper limit of the water concentration in the solvent used in the experiments was chosen as five percent because the process solvent in the UCBSRP has this approximate water concentration. As shown in Chapter 2, an increase in water concentration decreases the sulfur solubility in the solvent. As a result, an increase in water concentration in the solvent used in the experimental crystallizer reduces the maximum slurry density produced from the crystallizer. This effect of water concentration on the crystallization kinetics by the change in slurry density is well characterized and is discussed in Section 3.6.3. However, the water concentration may also have an effect on the crystallization kinetics by acting as an impurity.

The presence of an impurity in the mother liquor typically increases the nucleation rate by decreasing the metastable zone for supersaturation. The presence of an impurity also retards the growth rate by increasing the interfacial energy at the crystal surface and by blocking active growth sites (Nývlt *et al.*, 1985). The effect of the impurity is usually observed by the change in the kinetic constant k_N for the kinetics expression (Equation (3-18) but not in the kinetic order i, which is also in the kinetics expression (Garside and Shah, 1980). Since the molecular weights of Triglyme (178.22) and water (18.015) are quite different, the five weight percent water concentration translates to a much larger mole percent, roughly thirty four percent. This large molar water concentration may impede the diffusion of sulfur in the solvent because the sulfur is essentially insoluble in water. No attempt was made to estimate or measure the diffusivity of sulfur in solutions of water and Triglyme because the two liquids are so physically different than the solute, assumed to be in solution as an S_8-ring.

The constrained MSCPR model was applied to the crystal-size distribution data produced from the experimental runs where water concentration and residence time were varied. The constrained MSCPR analysis yielded values for the three fitted parameters: specific nuclei population density, growth rate, and z. From these three parameters, the specific nucleation rate and the mass-average particle size were calculated using Equations (3-21) and (3-17). The results of the constrained MSCPR analysis are listed in Appendix B. The trends in the fitted and calculated parameters with increasing residence time are in line with those observed from the variable residence time study. Specifically, both the nucleation and growth rates decreased with residence time while the mass-average particle size increased. However, the trends in the parameters with decreasing slurry density (increasing water concentration) are not as clear as those observed for the variable slurry density study. This may be a result of the slurry density not being varied over a large enough range. As illustrated

in Table 3.10, the maximum slurry density does not change significantly over the range of water concentration. The maximum slurry densities were computed from Equation (3-39) and from the sulfur solubility correlation in Chapter 2. Table 3.10 also lists the calculated values of the MSCPR slurry density from Equation (3-40). The range of water concentration (0.5 - 5.0 wt. %) changes the maximum slurry density from 2.993 to 1.998 kg/m^3.

3.6.5.1 Determination of Kinetic Constants

The specific nucleation and growth rate data from the constrained MSCPR analysis were plotted as prescribed by Equation (3-41) to determine the effect of the water concentration on the kinetic constants (k_N and i). Figure 3.23 shows the variable water concentration data along with the variable slurry density data from Section 3.6.3. The water concentration data are expected to lie between the data from the 40°- and 50^oC-feed runs since the slurry densities for the runs with higher water concentration are between those of the 40°- and 50^oC-feed runs. This is indeed observed in Figure 3.23. The slope of the variable water concentration data is slightly less than the slopes of the 40°- and 50^oC-feed runs, but is almost the same as the 60^oC-feed runs. Judging from the scatter of the data, it was determined that the water concentration in the process solvent had no effect on the crystallization kinetics of the system other than to change the sulfur solubility in the solvent. As a result, the effect of water in the process solvent is accommodated by computing the sulfur solubility in the solvent from the correlation in Chapter 2, computing the maximum slurry density from Equation (3-41), and plugging the results into the MSCPR design equation (Equation (3-19)).

3.6.3.4 Prediction of the Experimental Data from the Design Equation

The values of i, j, k_N, average z, and L_c were used in the MSCPR design equation to predict the mass-average particle size produced from a given residence time and a

given change in the solute solubility in the crystallizer feed and effluent streams. The values of i, j, k_N, average z, and L_c used were those derived from the variable slurry density study (Section 3.6.3) and are listed in Table 3.6. The measured residence time and calculated change in solids concentration (maximum slurry density) were used as inputs for Equation (3-19) to calculate the mass-average particle size for each of the nine runs in this study. A comparison of the mass-average particle size measured for each run with that calculated from Equation (3-19) gave a maximum error of eleven percent. The error between values increased as the difference between the fitted z and average z (2.25) increased. From these results, the kinetics expression and the kinetic constants derived from previous sections yielded acceptable agreement between the observed mass-average particle size and that calculated from the MSCPR design equation. Better agreement could be obtained by fine tuning the design equation by altering the value of the MSCPR parameter z.

Finally, the crystal-size distributions for the nine variable water concentration runs were predicted, using the same values of i, j, k_N, average z, and L_c as above. Figure 3.24 shows a typical run where the crystal-size distribution is predicted well by the MSCPR design equation. The location of the "knee" is correct, as is the location of the intercept if the under-sized data are extrapolated to zero size. The slopes of the plots on both sides of the "knee" agree very well with the experimental crystal-size distribution data. In general, the predicted plot for each run compared well with the observed crystal-size distribution, except where the observed value of z deviated far from the value of 2.25.

3.7 Fluidized-Bed Crystallizer Results and Discussion

The experimental crystallizer was operated in a fluidized-bed configuration in an attempt to produce large, mono-sized sulfur crystals. Refer to Section 3.3.2 for a thorough description of the fluidized-bed crystallization apparatus. The fluidized-bed crystallizer was constructed from the back-mixed crystallization vessel and from an

elutriation leg attached to the vessel's exit port, located on the bottom of the vessel (see Figure 3.5). The sulfur-saturated feed solution was fed into the crystallizer as in the back-mixed crystallization runs. The mother liquor was removed from the crystallizer via an overhead tube and was either returned to the solvent holding tank or pumped up the elutriation leg. The fluid velocity up the elutriation leg dictated the size of sulfur crystals that dropped out of the active crystallizer volume, since the crystals' settling velocity had to overcome the fluid velocity.

The production of individual sulfur crystals from the bottom of the elutriation leg was difficult, since most of the sulfur crystals were agglomerates. The agglomerates were formed in the lower fluidized zone in the crystallizer, where the degree of mixedness was low compared to the mixedness in the back-mixed crystallization runs. As the mixedness was increased to reduce the agglomeration, the upper clarified zone in the crystallizer was less effective in separating the crystals from the mother liquor. As a result, more sulfur crystals were carried over the overhead tube and the inventory of sulfur crystals in the fluidized zone was reduced. Therefore, the fluidized-bed crystallization apparatus proved to be inadequate in producing large individual sulfur crystals. The agglomerates that were collected from the bottom of the elutriation leg were too large to measure using the HIAC particle-size analyzer because they plugged the sensor. Since the apparatus did not produce the desired sulfur product and the sulfur crystals that were produced were not analyzed, the results from the fluidized-bed crystallization experiments are inconclusive.

3.8 Sulfur Purity and Morphology

The quality of the elemental sulfur crystallized from the process solvent in the UCBSRP must be high so that it may be a marketable product. The purity of the sulfur crystals must be high (99+ percent) to eliminate further processing. The shape and morphology of the crystalline product must be conducive to rapid and complete separation of the mother liquor from the product. The sulfur crystals must also be

hard and resilient from fracture.

3.8.1 Sulfur Purity Analysis

3.8.1.1 Method of the Sulfur Purity Analysis

The purity of the sulfur crystals produced from the thermal crystallization runs was determined by a technique that combines gas-chromatography and gravimetry. The analysis was based on the following procedures. A small amount of solid sulfur (0.30 grams) was dissolved in a minimal amount of carbon disulfide. The equilibrium solubility of sulfur in carbon disulfide is approximately thirty weight percent at room temperature (Tuller, 1954). The carbon disulfide (1.0 grams) dissolved all of the sulfur and also dissolved (or it was assumed to dissolve) the impurities in the sulfur. The only impurity anticipated to be in the sulfur crystals was the solvent from which the sulfur was crystallized, namely Triglyme. Since the Triglyme concentration in the sulfur was expected to be of the order of one percent, quinoline was added as a third component to serve as a tracer. Quinoline was used as the tracer because it was not present in the crystallization apparatus. In addition, quinoline has a boiling point (237°C) near that of Triglyme (216°C) so that it elutes from the gas chromatograph near the Triglyme peak. The amount of quinoline added was equal to the amount of Triglyme thought to be present (0.01 grams) in the sulfur sample. The addition of the tracer component in a quantity about equal to that of Triglyme provided a reference peak on the chromatogram equal in magnitude to the Triglyme peak for accurately estimating the Triglyme concentration. The weight of each compound was noted to enable back-calculation of the amount of Triglyme present. Careful handling of the carbon disulfide solutions was required because carbon disulfide is extremely volatile. Erroneous gravimetric readings would result if any of the carbon disulfide was allowed to escape.

A calibration curve was produced from a series of standard solutions made with variable Triglyme concentration, but with constant quinoline concentration. Observed

gas chromatograph Triglyme/quinoline area ratios were plotted versus measured Triglyme/quinoline mass ratios. Sulfur crystals produced from crystallization runs were dissolved in carbon disulfide, quinoline was added, and the solution was injected into the gas chromatograph. The Triglyme concentrations in the sulfur samples were determined from the gas chromatograph output, the calibration curve, and the gravimetric data produced from making the solutions. The results from this sulfur purity study are shown in Table 3.11. In general, the sulfur purity is roughly 99.8 percent sulfur on a weight basis.

3.8.1.2 Results and Discussion of the Sulfur Purity Analysis

An interesting trend is exhibited by the sulfur purity data. Referring to Table 3.11, the sulfur purity increases with decreasing residence time (Runs 48, 43, and 46). Since the crystal growth rate is higher and the mass-average particle size is smaller at lower residence times, perhaps the increase in growth rate or the smaller crystal size reduces the occlusion of solvent in the sulfur crystal lattice. The amount of residual solvent residing on the crystal surface is believed to be small because the sulfur used in this analysis was washed with an ethanol/water mixture after the mother liquor was vacuum-filtered from the crystals. The sulfur purity data are encouraging for the prospect of producing a marketable sulfur product.

3.8.2 Sulfur Morphology Analysis

A melting-point analysis was also performed on the sulfur crystals produced from the thermal crystallization runs. All of the sulfur samples from the runs listed in Table 3.11 gave melting points between 112° to 119°C. This temperature range indicates that the crystalline morphology of the sulfur is a mixture of orthorhombic sulfur (*m.p.* = 113°C) and monoclinic sulfur (*m.p.* = 119°C). The relative amount of each form is unknown and is difficult to determine. This difficulty arises from the slow phase transition of orthorhombic to monoclinic sulfur at 95.5^{o}C and from the

melting-point depression caused by the two phases (Thackray, 1965). Such a determination requires more sophisticated equipment than was used for the above melting-point analysis and is beyond the scope of this work.

A visual inspection of the sulfur crystals produced from both the back-mixed and fluidized-bed experiments yielded further encouragement for the production of a marketable sulfur product. Figure 3.25 shows a photomicrograph of sulfur crystals produced from Run 43, a back-mixed crystallization run. The crystals exhibit the basic orthorhombic geometry. Very little of the dendritic, needle-like crystals are observed. Figure 3.26 shows a photomicrograph of sulfur crystals and agglomerates produced from Run 57, a fluidized-bed crystallization run. The orthorhombic shape is still visible, but the absence of individual crystals is evident. The individual crystals and the agglomerates from Runs 43 and 57, respectively, were relatively hard and were resilient to fracture under normal handling conditions.

The orthorhombic geometry of the sulfur crystals yields a volumetric shape factor (k_V) very close to that assumed in the analysis of the crystallization kinetics. The assumed shape factor corresponds to assuming spherical crystals, where $k_V = \pi/6$ or 0.5236. For the orthorhombic crystals, the shape factor is $k_V = 2/3$ or 0.6667. The orthorhombic shape factor was computed by assuming the base of the rhombus lies diagonally in the unit cell. The agreement of the two shape factors lends credence to the values reported in the crystallization kinetics expression.

3.9 Summary

The thermal crystallization of elemental sulfur from Triglyme, a polyglycol ether solvent, was successfully performed in a laboratory-scale crystallizer. The high-quality sulfur crystals produced from the experimental crystallizer were 99.7+ percent pure and exhibited defined crystalline morphology. The sulfur crystals were large enough to allow their easy separation from the mother liquor. The mass-average particle size of the sulfur crystals produced from all of the experimental runs was

between 200 and 300 μm. After recovering the crystals from the mother liquor and washing them with water to remove any residual liquor, the marketable sulfur product would require no further processing.

The crystallization kinetics of the sulfur/Triglyme system were obtained and are similar to the kinetics exhibited by inorganic salts crystallized from aqueous solutions. The thermal crystallization study yielded the following kinetics expression:

$$B^o = 1.04\ G^{1.55}\ M_T^{0.943} \tag{3-51}$$

The kinetics were derived from the mixed-suspension classified-product removal (MSCPR) crystallizer model, which is based on the well-known population balance theory. The internal classification that was observed in the experimental crystallizer required the application of the MSCPR model so that the true crystallization kinetics were isolated from the classification mechanism. The crystallizer operating parameters varied in the laboratory-scale experiments were residence time, slurry density, impeller power input, and water concentration in the solvent. These parameters had the following ranges:

Residence Time	4.0 - 67.	minutes
Slurry Density	1.2 - 5.5	kg solute/m^3 clear liquor
Impeller Power Input	0.0064 - 0.14	watts/kg solution
Water Concentration	0.5 - 5.0	weight percent

The dependence of the crystallization kinetics on the residence time and slurry density was used to determine the constants in Equation (3-51). The effect of impeller power input on the kinetics was not determined because the power effect was not isolated from the internal classification of the experimental crystallizer. The effect of variable water concentration in the process solvent on the crystallization kinetics was determined as the same effect of variable slurry density, since the solubility of sulfur in the process solvent is dependent on water concentration.

The MSCPR model was used to determine the dependence of the crystallization

kinetics on the crystallizer operating variables. The values of the MSCPR parameters, z and L_c, are dependent on the geometry of the crystallizer and are unique to the experimental crystallizer used in this study. These parameters were used to isolate the true crystallization kinetics from the internal classification of the experimental crystallizer. As a result, the dependence of the crystallization kinetics on the operating parameters derived from this study is applicable not only to crystallizers with classified-product removal (as was the case for the experimental crystallizer), but to any crystallizer configuration. Depending on the application, the sulfur crystallizer may be a simple MSMPR crystallizer or may have additional fines-destruction and external-classification equipment to produce a narrow crystal-size distribution. For the simple MSMPR crystallizer, the parameters z and L_c are not required. For the more complex crystallizer, the values of z and L_c are determined by the design of that crystallizer and are independent of the values of z and L_c observed in this study. In any case, the crystallization kinetics produced from this study may be used to design either crystallizer. The crystallization kinetics can be used in a design equation to scale-up an industrial-sized crystallizer or to predict the sulfur crystal-size distribution from an existing crystallizer.

3.10 Nomenclature

3.10.1 Variables for Crystallization Kinetics

B^o = crystal nucleation rate [= n^oG] (#/min-cm^3)

$B(L)$ = crystal birth rate (#/min-μm-cm^3)

C_k = solute concentration in k^{th} stream (kg/m^3)

$D(L)$ = crystal death rate (#/min-μm-cm^3)

G = linear crystal growth rate (μm/min)

h = specific power input exponent

i = kinetic order

j = secondary nucleation kinetic order

k_N = kinetics expression constant

k_V = crystal volumetric shape factor (m^3/m^3)

L = crystal size (μm)

L_c = critical crystal size [= location of knee in distribution (μm)

M_T = slurry density of all crystals in suspension (kg/m^3)

M_T^+ = slurry density of over-sized crystals (kg/m^3)

n = population density [= $n(L)$] (#/μm-cm^3)

n^o = nuclei population density [= $n(L=0)$] (#/μm-cm^3)

n_k = population density in k^{th} stream (#/μm-cm^3)

Q_k = volumetric flow rate of kth stream (m^3/min)
positive for flow in, negative for flow out

R = volumetric flow rate through the recycle loop (m^3/min)

t = time (min)

V = suspension volume (m^3)

ϵ = specific power input (W/kg of solution)

ρ_C = crystal density (kg/m^3)

τ = crystal residence time in the crystallizer [= V/Q_2] (min)

3.10.2 Variables for HIAC Particle-Size Analyzer

L_i = mean particle size of HIAC channel i (μm)

Δ_i = particle count in HIAC channel i

ΔL = width of HIAC channel i (μm)

3.10.3 Variables for Impeller Power and Rotation Rate Correlations

a, b = fitted constants [= fxn (geometry, baffles)]

D_i = impeller diameter (m)

Fr = Froude number [= $N^2 D_i / g$]

g = gravitational constant (m/sec^2)

L_m = maximum size of suspended particles (m)

m = Froude number exponent

N = rotation rate of impeller (sec^{-1})

N_m = minimum rotation rate of impeller to just suspend particles (sec^{-1})

P = power input to impeller (W = N-m/sec)

Re = Reynolds number [= $N D_i^2 \rho_L / \mu$]

S = complete suspension parameter [= fxn (geometry)]

V = suspension volume (m^3)

W = weight percent solids in solution

ϵ = specific power input (W/kg of solution)

μ = viscosity of liquid (kg/m-sec)

ν = kinematic viscosity of liquid (m^2/sec)

ρ_L = density of liquid (kg/m^3)

ρ_S = density of solid particles (kg/m^3)

Φ = power function

3.10.4 Variables for Water Concentration Determination

A_h = heptane peak area from gas chromatograph

A_w = water peak area from gas chromatograph

R = ratio multiplier between measured values and gas chromatograph

w_a = weight percent water in sample which was added

w_h = weight percent heptane in sample

w_t = weight percent water in sample from "clean" Triglyme

w_w = weight percent water in sample

List of Tables for Chapter 3

3.1 Measured and Calculated Kinetic Variables for Run 38-1

3.2 Kinetic Constants Derived from Equation (3-38) and the Variable Residence Time Data

3.3 Computed and Measured Slurry Densities for the Variable Slurry Density Study

3.4 Kinetic Order (i) Derived from Equations (3-21), (3-22), & (3-23) and the Variable Slurry Density Data

3.5 Secondary Nucleation Order (j) Derived from Equations (3-24), (3-25), & (3-26) and the Variable Slurry Density Data

3.6 Kinetic Constants Derived from Equation (3-41) and the Variable Slurry Density Data

3.7 Results of Predictions from Design Equation for the Runs in the Variable Slurry Density Study

3.8 Specific Power Input Values from Equation (3-42) for the Runs in the Variable Impeller Power Input Study

3.9 Specific Power Input Exponent (h) Derived from Equations (3-24), (3-25), & (3-26) and the Variable Impeller Power Input Data

3.10 Computed Slurry Densities for the Variable Water Concentration Study

3.11 Results from Sulfur Purity Analysis using Gas Chromatography

List of Figures for Chapter 3

3.1 Schematic Representation of MSMPR Crystallizer

3.2 Schematic Representation of MSCPR Crystallizer

3.3 Thermal Crystallization Apparatus: Back-Mixed Crystallizer

3.4 Crystallizer Dimensions

3.5 Thermal Crystallization Apparatus: Fluidized-Bed Crystallizer

3.6 Crystal-Size Distribution Analysis Apparatus

3.7 Typical Crystal-Size Distribution with MSMPR Model

3.8 Typical Crystal-Size Distribution with MSCPR Model

3.9 Effect of Residence Time on Crystal-Size Distribution and MSCPR Model

3.10 Dependence of Crystallization Kinetics on Residence Time

3.11 Dependence of Mass-Average Particle Size on Residence Time

3.12 Effect of Residence Time on MSCPR Parameter Z

3.13 Comparison of MSCPR Models with Fitted and Average Z

3.14 Comparison of Design Equation and Experimental Data

3.15 Effect of Z on MSCPR Design Equation

3.16 Effect of Slurry Density on Crystal-Size Distribution

3.17 Dependence of Crystallization Kinetics on Slurry Density

3.18 Dependence of Mass-Average Particle Size on Slurry Density

3.19 Effect of Residence and Slurry Density on Z

3.20 Comparison of Design Equation and Experimental Data

3.21 Effect of Power Input on Crystal-Size Distribution

3.22 Effect of Impeller Power Input on Crystallization Parameters

3.23 Effect of Water Concentration on Crystallization Kinetics

3.24 Predicted Crystal-Size Distribution from MSCPR Design Equation

3.25 Photomicrograph of Sulfur Crystals from Back-Mixed Crystallization Run

3.26 Photomicrograph of Sulfur Crystals from Fluidized-Bed Crystallization Run

Table 3.1

Measured and Calculated Kinetic Variables for Run 38-1

Variable	Units	Observed	constrained MSMPR	constrained MSCPR
τ	(min)	9.54	9.54	9.54
$n^o \rho_C k_V / M_T$	(#/μm-cm^3)	-	2910.	1730.
G	(μm/min)	-	9.12	16.8
$B^o \rho_C k_V / M_T$	(#/min-cm^3)	-	26500.	29200.
$\mathscr{L}$	(μm)	261.	348.	257.

Table 3.2

Kinetic Constants Derived from Equation (3-38) and the Variable Residence Time Data

Kinetic Constant	MSCPR z = fitted	MSCPR z = 3.13
i	1.42	1.54
k_N	0.703	0.562

$$B^o \rho_C k_V / M_T = k_N \rho_C k_V \, G^i$$

$$\rho_C = 2070.$$

$$k_V = \pi/6$$

Table 3.3

Computed and Measured Slurry Densities for the Variable Slurry Density Study

Feed Temp. (deg C)	Res. Time (min)	M_T(max) (kg/m^3)	M_T(cpr) (kg/m^3)	M_T(obs) (kg/m^3)
40	45	1.23	0.87	0.390
	16	1.23	1.00	0.35
	4	1.23	1.21	0.0809
50	45	2.99	1.71	1.26
	16	2.99	2.06	1.94
	4	2.99	2.27	1.85
60	45	5.52	3.18	2.50
	16	5.52	3.29	3.81
	4	5.52	3.28	5.04

$$M_T(\max) = C_1 - C_2$$

$$M_T(\mathrm{cpr}) = (C_1 - C_2)/[1 + B(z-1)\exp((z-1)L_c/G\tau))(n^0\rho_C k_V/M_T)(G\tau/z)^4]$$

$$C_i \simeq \rho_{solvent} w_{sulfur}$$

w_{sulfur} = fxn (temperature, water concentration in solvent) [see Chapter 2]

Table 3.4

Kinetic Order (i) Derived from Equations (3-21), (3-22), & (3-23) and the Variable Slurry Density Data

Plot	Value of i: MSCPR z = fitted	Value of i: MSCPR z = 1.98
$\mathscr{L}$(exp.) -vs- τ	1.31	1.31
G -vs- τ	1.92	1.80
$n^o \rho_C k_V / M_T$ -vs- τ	1.60	1.51
$B^o \rho_C k_V / M_T$ -vs- τ	1.50	1.46

Table 3.5

Secondary Nucleation Order (j) Derived from Equations (3-24), (3-25), & (3-26) and the Variable Slurry Density Data

Plot	Value of j: MSCPR z = fitted	Value of j: MSCPR z = 1.98
Assumed:	i = 1.31	i = 1.31
$\mathscr{L}$(obs) -vs- M_T(obs)	0.938	0.938
G -vs- M_T(obs)	0.361	0.798
$n^o \rho_C k_V / M_T$ -vs- M_T(obs)	0.683	0.858
$B^o \rho_C k_V / M_T$ -vs- M_T(obs)	0.791	0.880

Table 3.6

Kinetic Constants Derived from Equation (3-41) and the Variable Slurry Density Data

Kinetic Constant	MSCPR Model
i	1.55
j	0.943
k_N	1.04
z	1.98 -----> 2.25
L_c	250.

$$B^o \rho_C k_V / M_T = k_N \rho_C k_V \, G^i \, M_T^{j-1}$$

$$\rho_C = 2070.$$

$$k_V = \pi/6$$

Table 3.7

Results of Predictions from Design Equation for the Runs in the Variable Slurry Density Study

Run #	Residence Time (min)	Slurry Density (kg/m^3)		Mass-Average Crystal Size (μm)	
	Obs.	Calc.	Obs.	Calc.	Obs.
40^oC Feed					
45	46.2	0.726	0.390	277	260
44	16.7	0.782	0.350	249	248
48.1	4.01	0.871	0.0809	219	240
50^oC Feed					
46	43.8	1.77	1.26	278	279
43	15.9	1.90	1.94	250	245
48.2	4.05	2.11	1.85	221	230
60^oC Feed					
47	46.5	3.23	2.50	282	285
42	16.8	3.47	3.81	253	258
50	4.08	3.86	5.04	222	221

Kinetic constants:

$i = 1.55$
$j = 0.943$
$k_N = 1.04$

MSCPR model constants:

$z = 2.25$
$L_c = 250.$

Table 3.8

Specific Power Input Values from Equation (3-42) for the Runs in the Variable Impeller Power Input Study

Rotation Rate (RPM)	Reynolds Number	Specific Power Input (Watts/kg)
215	3180	0.0064
350	5180	0.024
680	10000	0.14

Equations (3-42) to (3-44)
a = 2.3
b = 18.
See Rushton *et al.*, (1950)

Table 3.9

Specific Power Input Exponent (h) Derived from Equations (3-24), (3-25), & (3-26) and the Variable Impeller Power Input Data

Plot	Value of h: MSCPR z = fitted
$\mathscr{L}$(exp.) -vs- ϵ	-0.0455
G -vs- ϵ	-0.153
$n^o \rho_C k_V / M_T$ -vs- ϵ	-0.296
$B^o \rho_C k_V / M_T$ -vs- ϵ	-0.105

Table 3.10

Computed Slurry Densities for the Variable Water Concentration Study

Water Conc. (wt. %)	Res. Time (min)	M_T(max) (kg/m^3)	M_T(cpr) (kg/m^3)
0.5	45	2.99	1.71
	16	2.99	2.06
	4	2.99	2.27
2.6	45	2.34	1.52
	16	2.34	1.36
	4	2.34	1.65
5.0	45	2.00	1.18
	16	2.00	1.22
	4	2.00	1.45

$$M_T(\max) = C_1 - C_2$$

$$M_T(\mathrm{cpr}) = (C_1 - C_2)/[1 + B(z-1)\exp((z-1)L_C/G\tau))(n^0\rho_C k_V/M_T)(G\tau/z)^4]$$

$$C_i \simeq \rho_{solvent} w_{sulfur}$$

w_{sulfur} = fxn (temperature, water concentration in solvent) [see Chapter 2]

Table 3.11

Results from Sulfur Purity Analysis using Gas Chromatography

Run #	Residence Time (min)	Type of Run	Wt. % Triglyme in Solid Sulfur
48	4	back-mixed	0.149 ± 0.020
43	16	back-mixed	0.198 ± 0.026
46	45	back-mixed	0.230 ± 0.034
57	-	fluidized-bed	0.162 ± 0.021

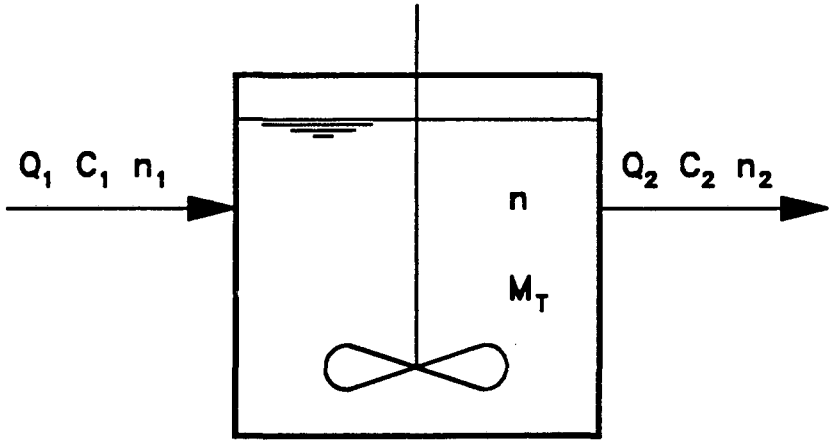

Figure 3.1 Schematic Representation of MSMPR Crystallizer

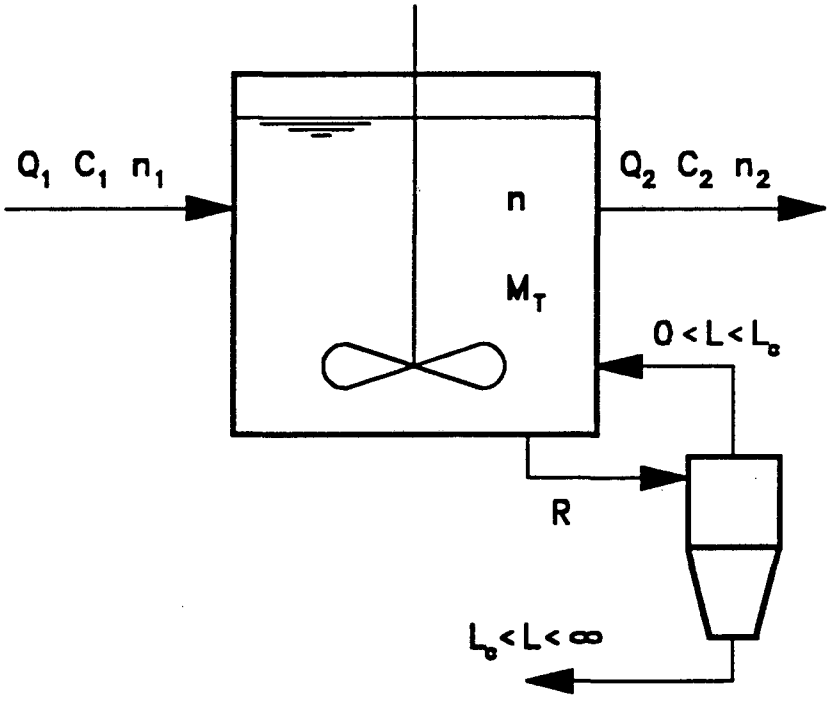

Figure 3.2 Schematic Representation of MSCPR Crystallizer

Figure 3.3
Thermal Crystallization Apparatus
Back–Mixed Crystallizer

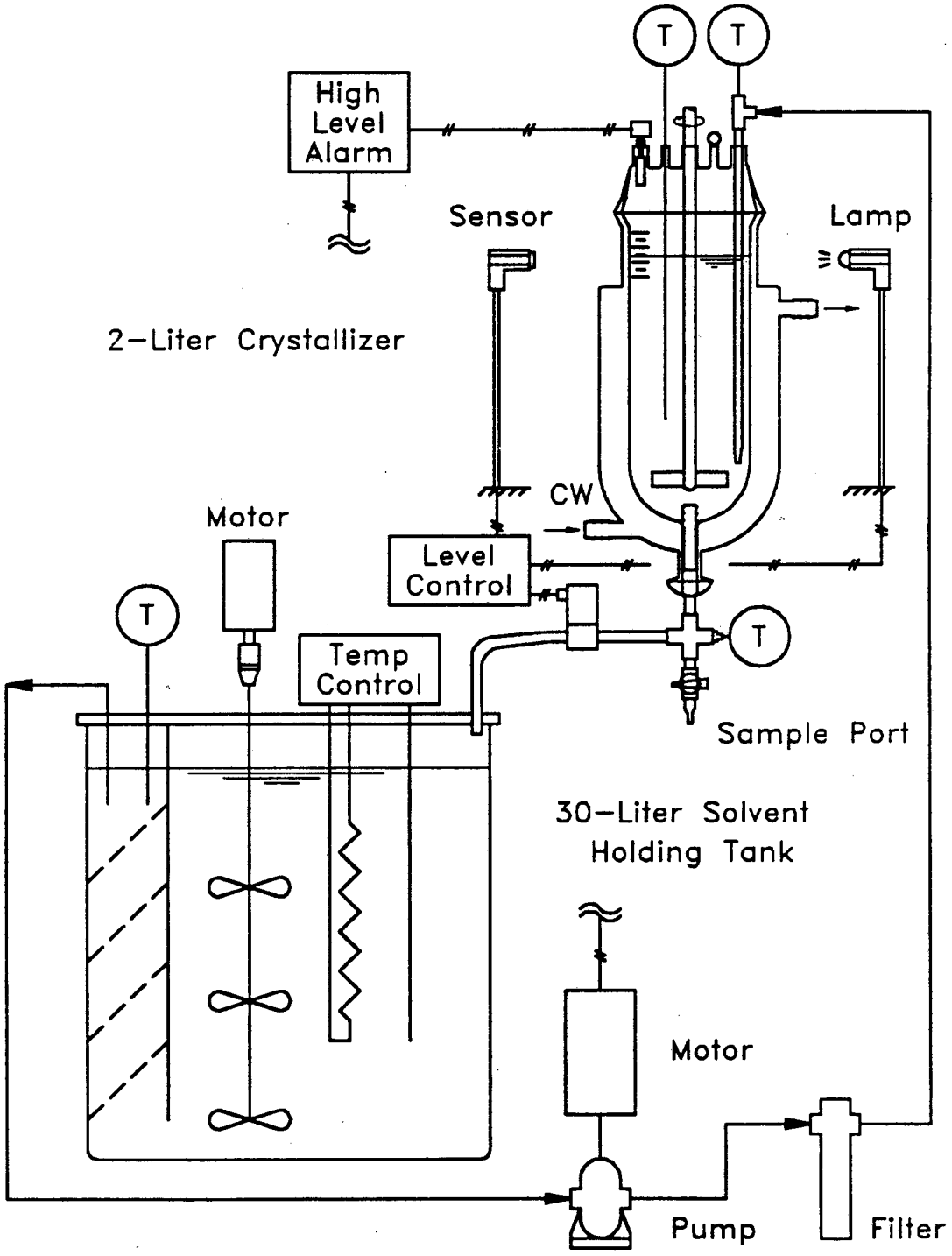

Figure 3.4
Crystallizer Dimensions

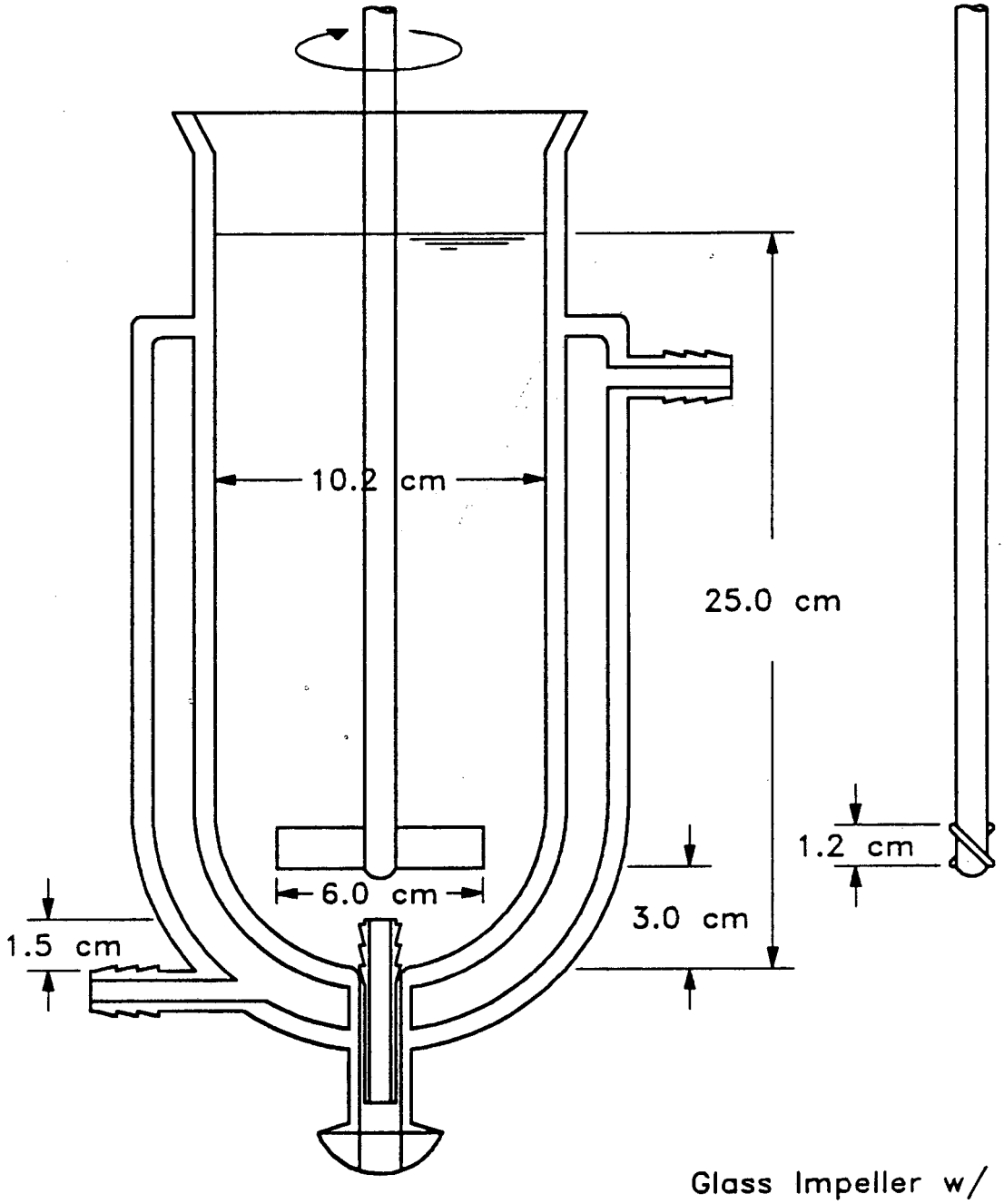

Glass Jacketed Flask

Glass Impeller w/
2 Blades @ 45°

Figure 3.5
Thermal Crystallization Apparatus
Fluidized-Bed Crystallizer

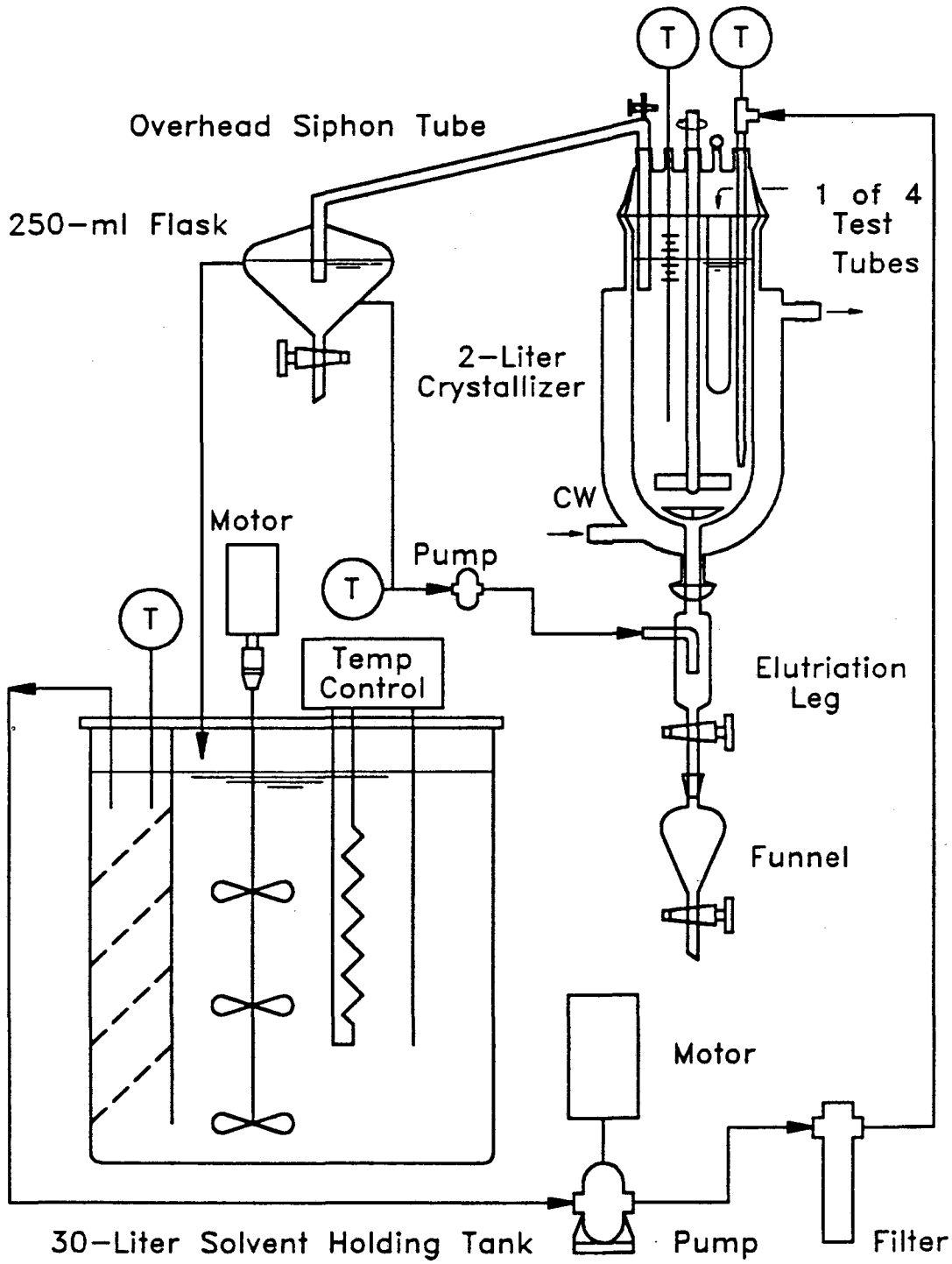

Figure 3.6
Crystal–Size Distribution Analysis Apparatus

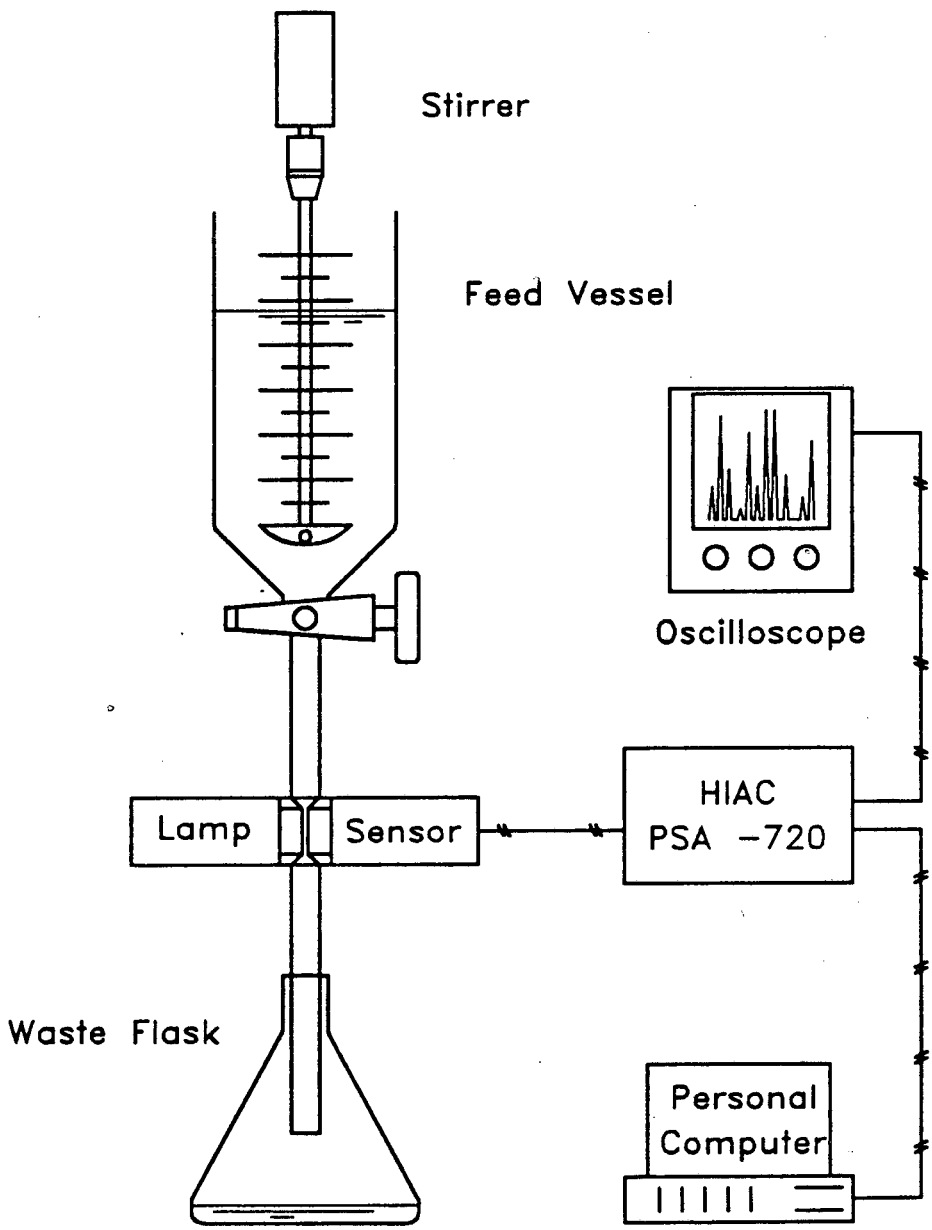

Figure 3.7

Typical CSD with MSMPR Model

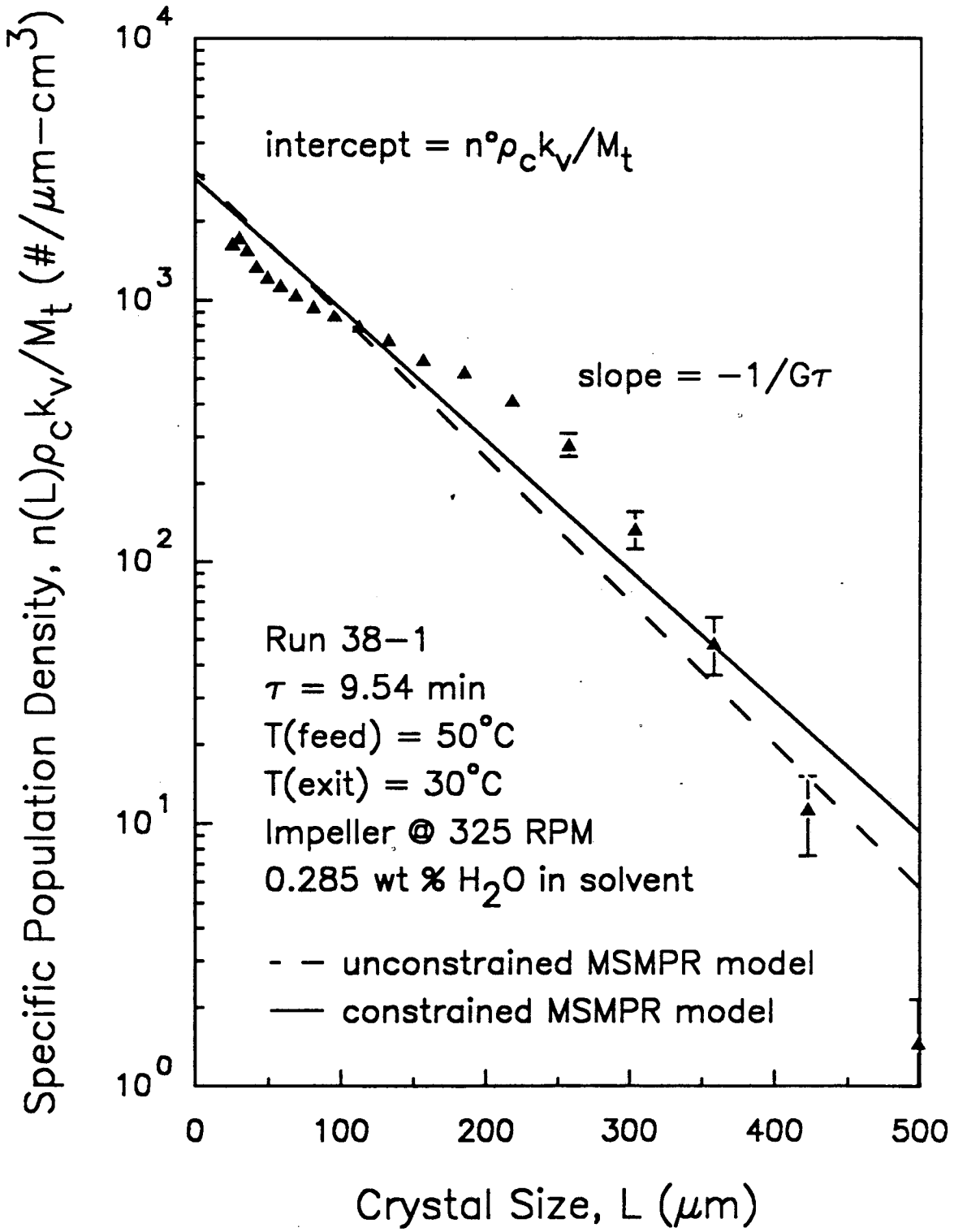

Figure 3.8

Typical CSD with MSCPR Model

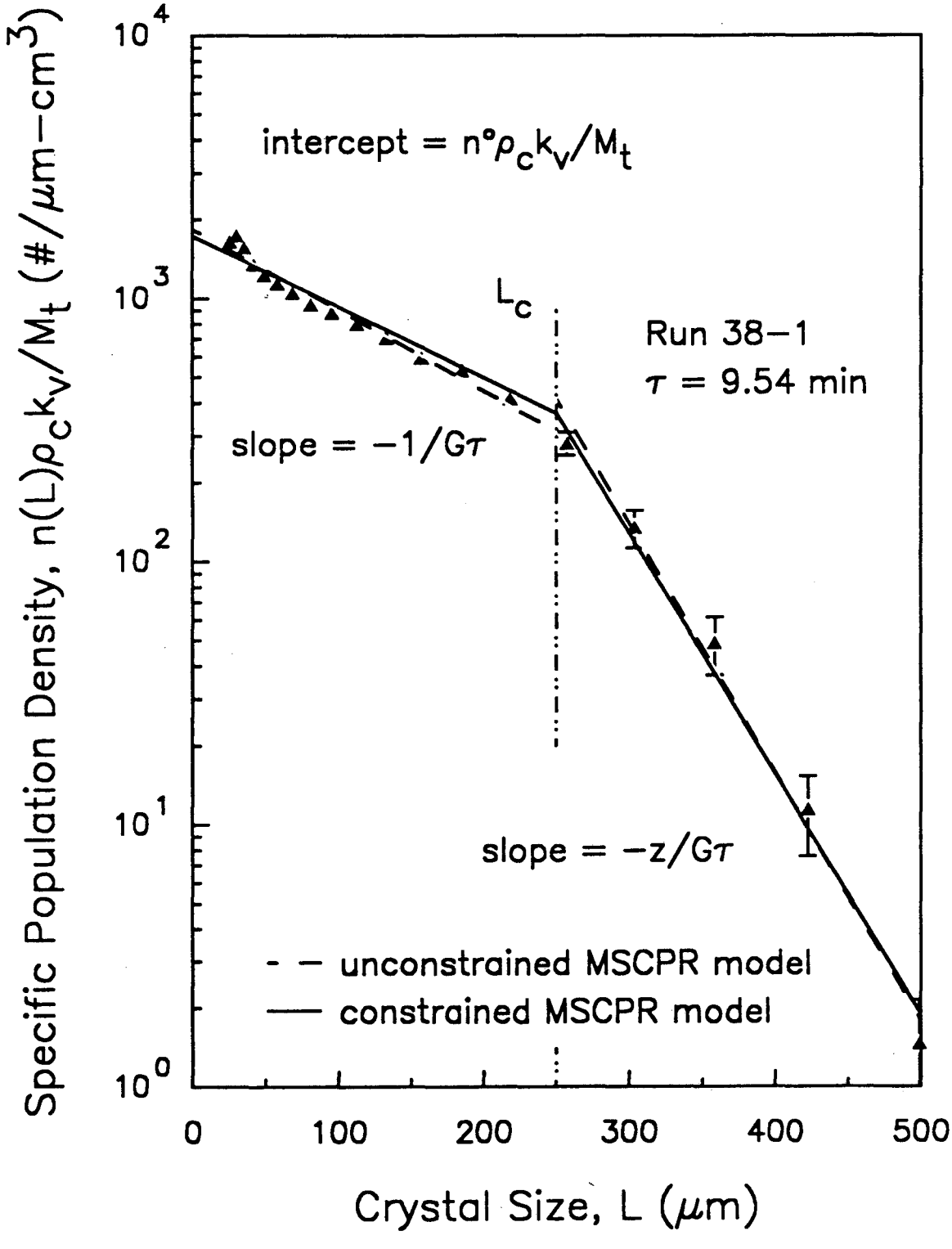

Figure 3.9

Effect of Residence Time on CSD and MSCPR Model

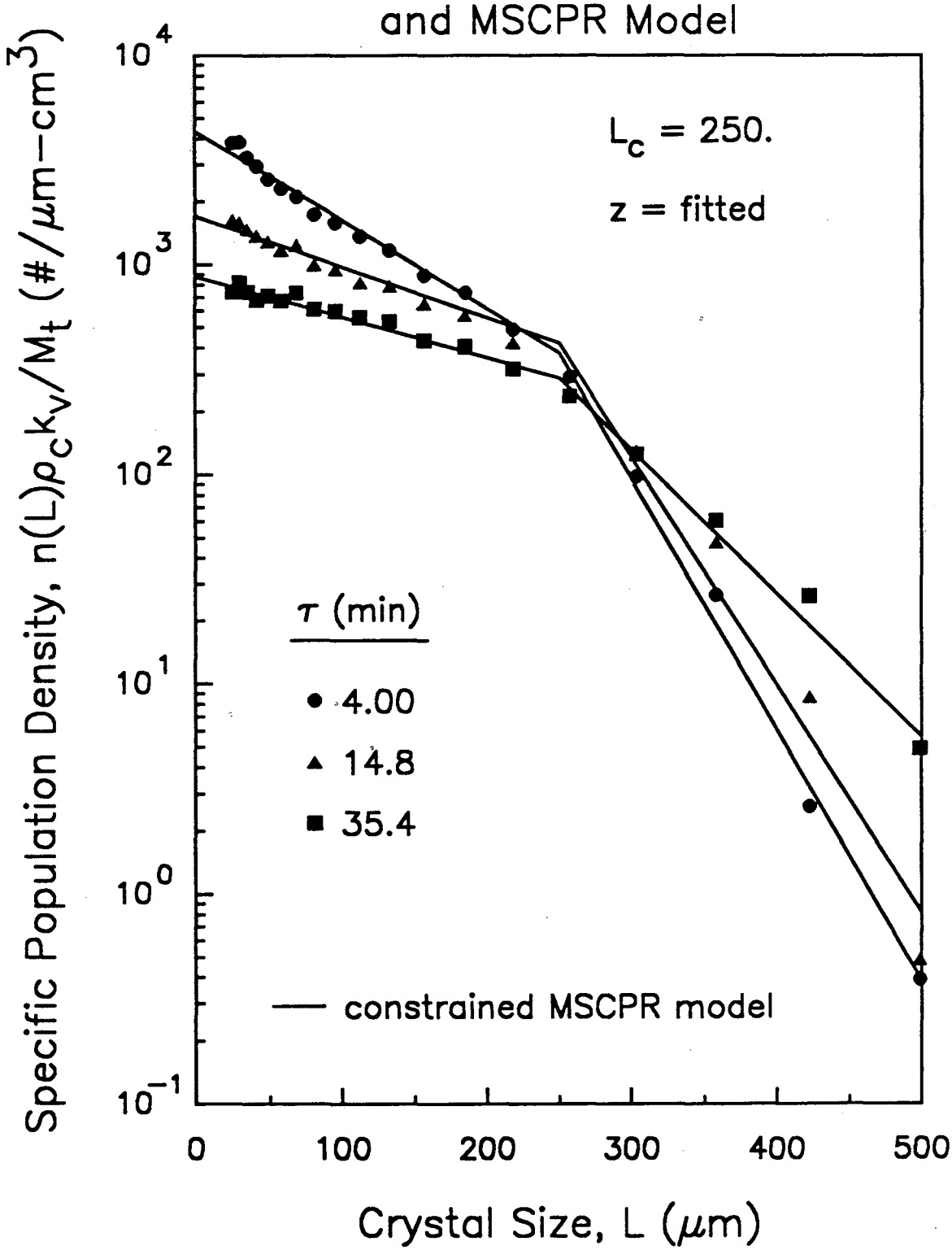

Figure 3.10

Dependence of Crystallization Kinetics on Residence Time

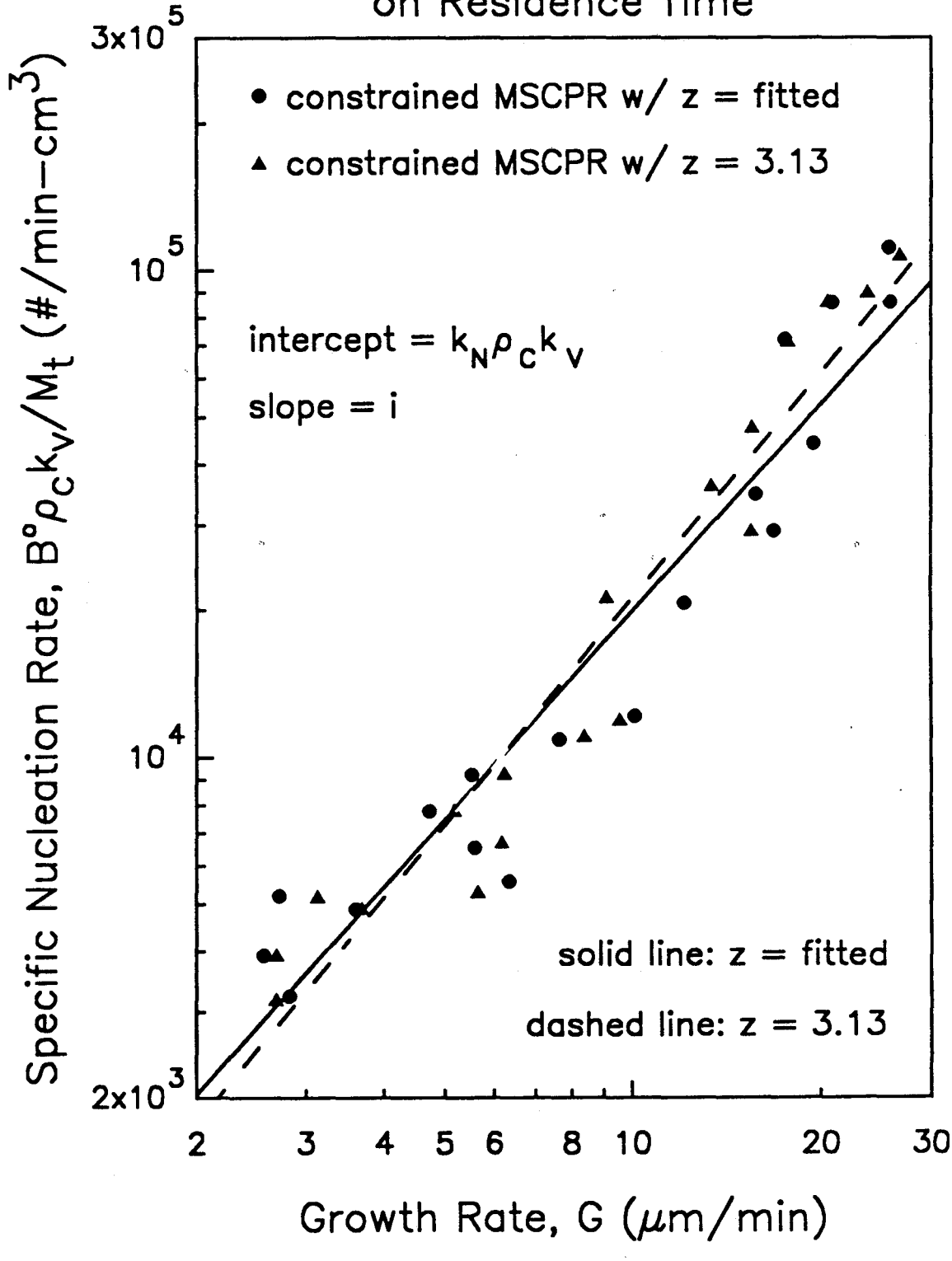

Figure 3.11

Dependence of Mass–Average Particle Size on Residence Time

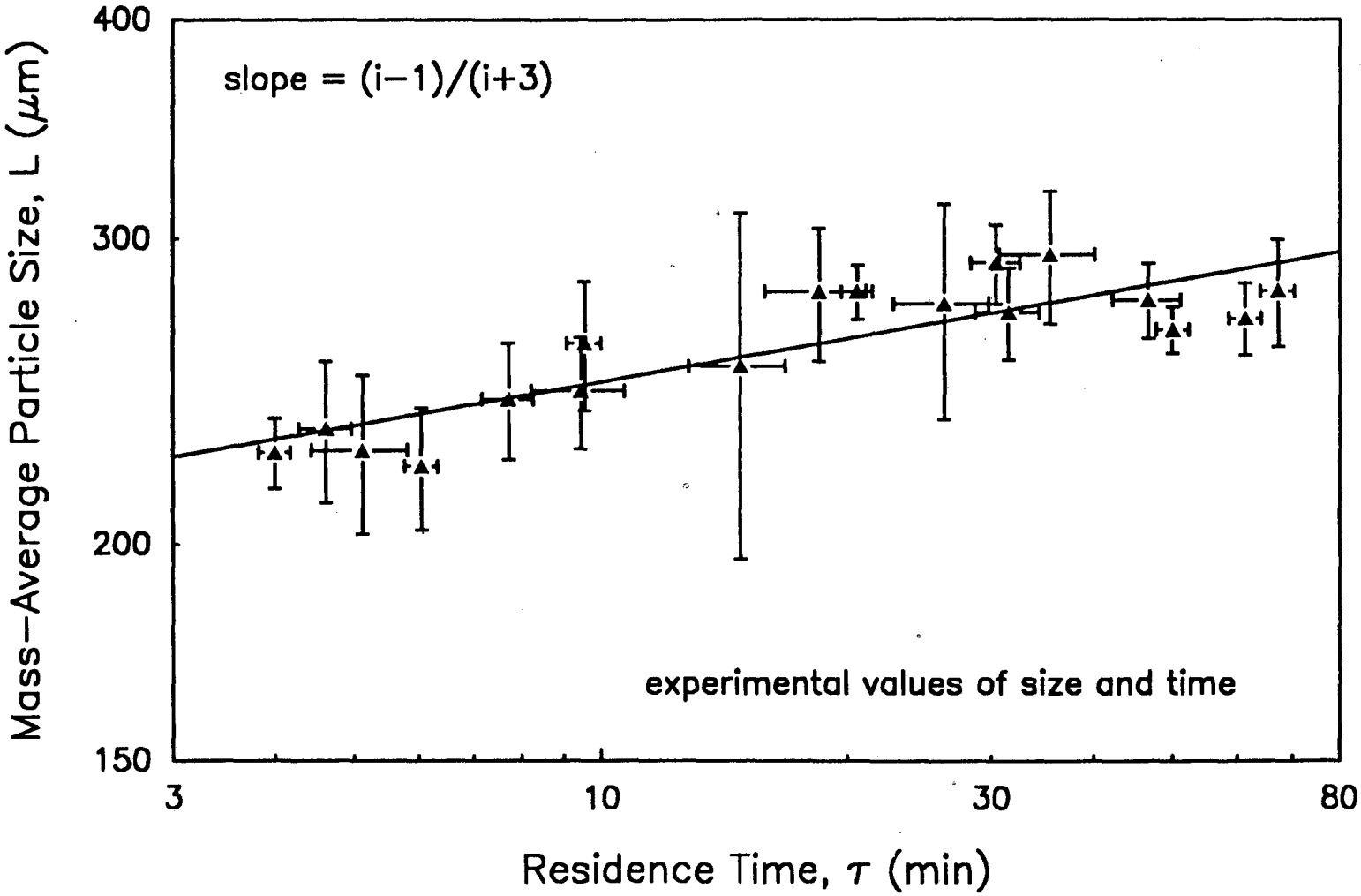

Figure 3.12

Effect of Residence Time on MSCPR Parameter Z

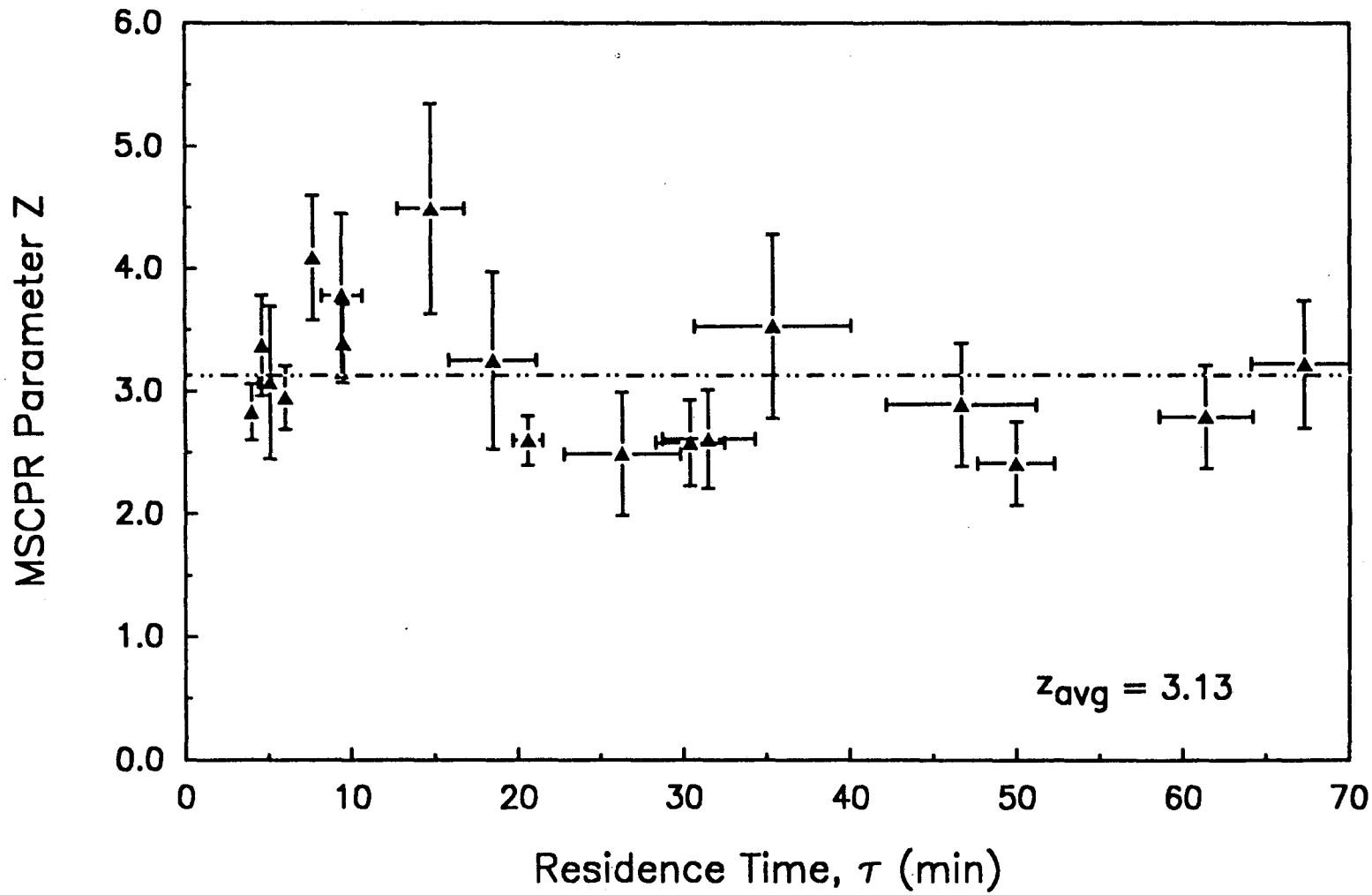

Figure 3.13

Comparison of MSCPR Models with Fitted and Average Z

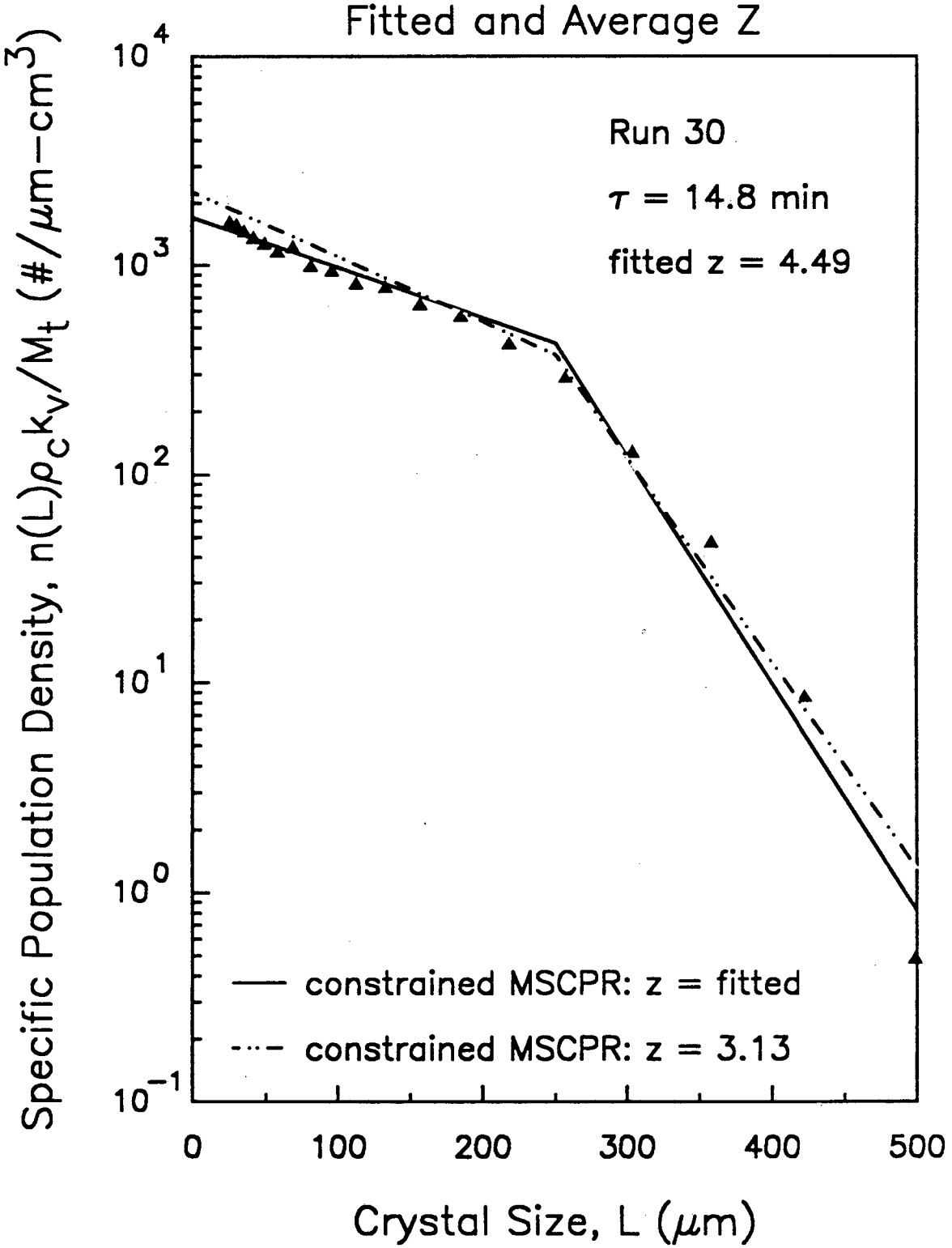

Figure 3.14

Comparison of Design Equation and Experimental Data

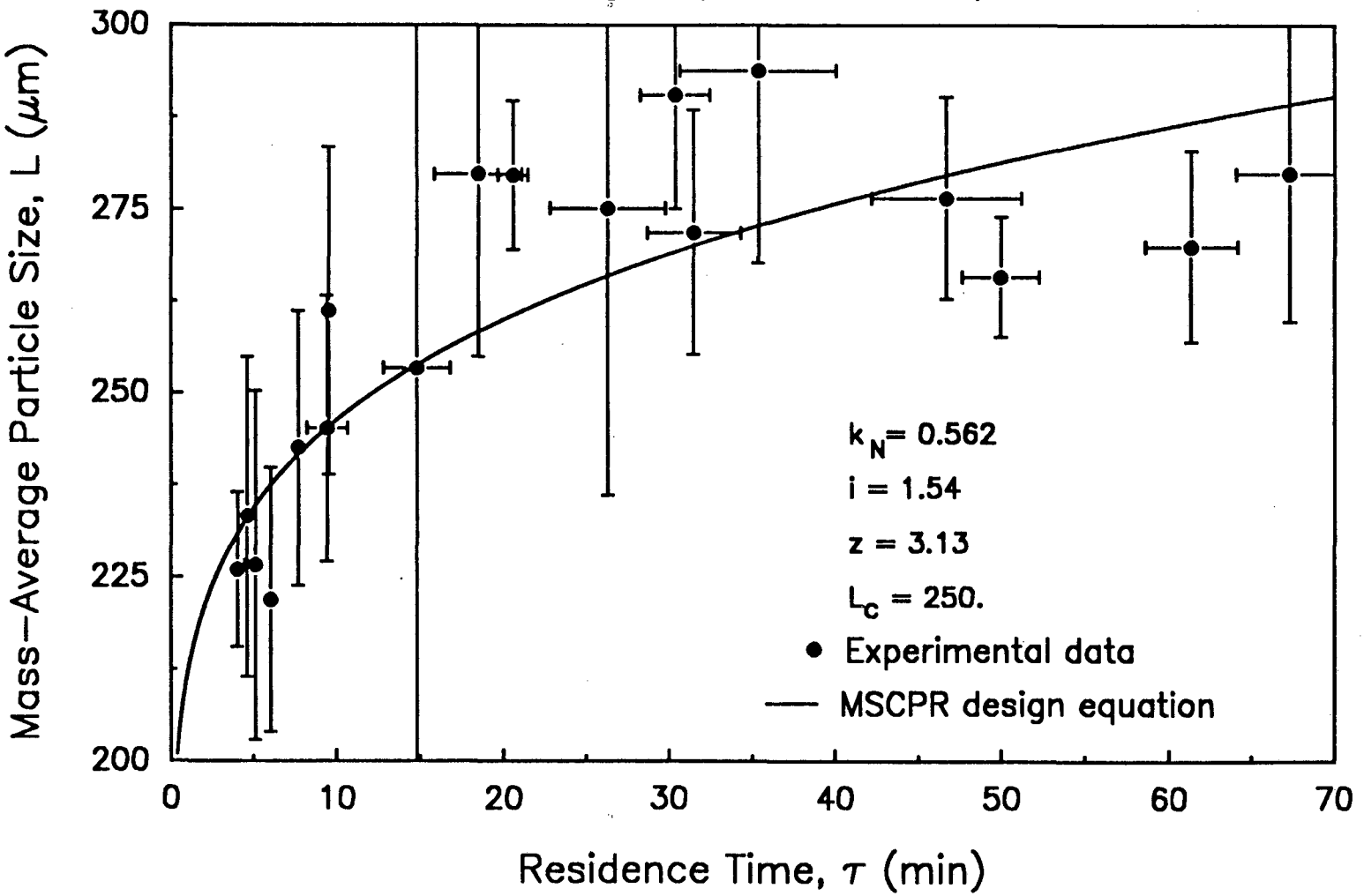

Figure 3.15

Effect of Z on MSCPR Design Equation

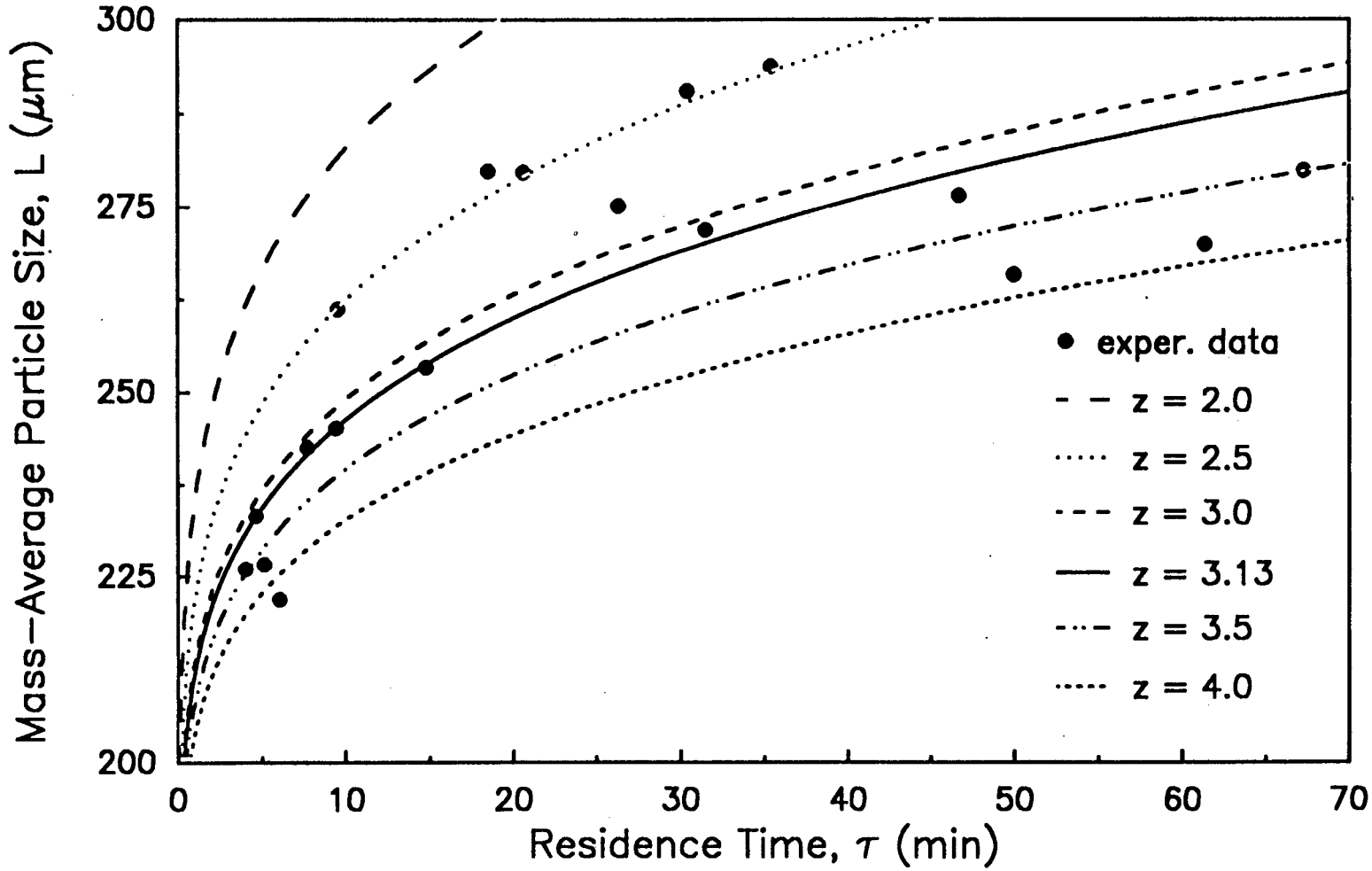

Figure 3.16
Effect of Slurry Density on Crystal–Size Distribution

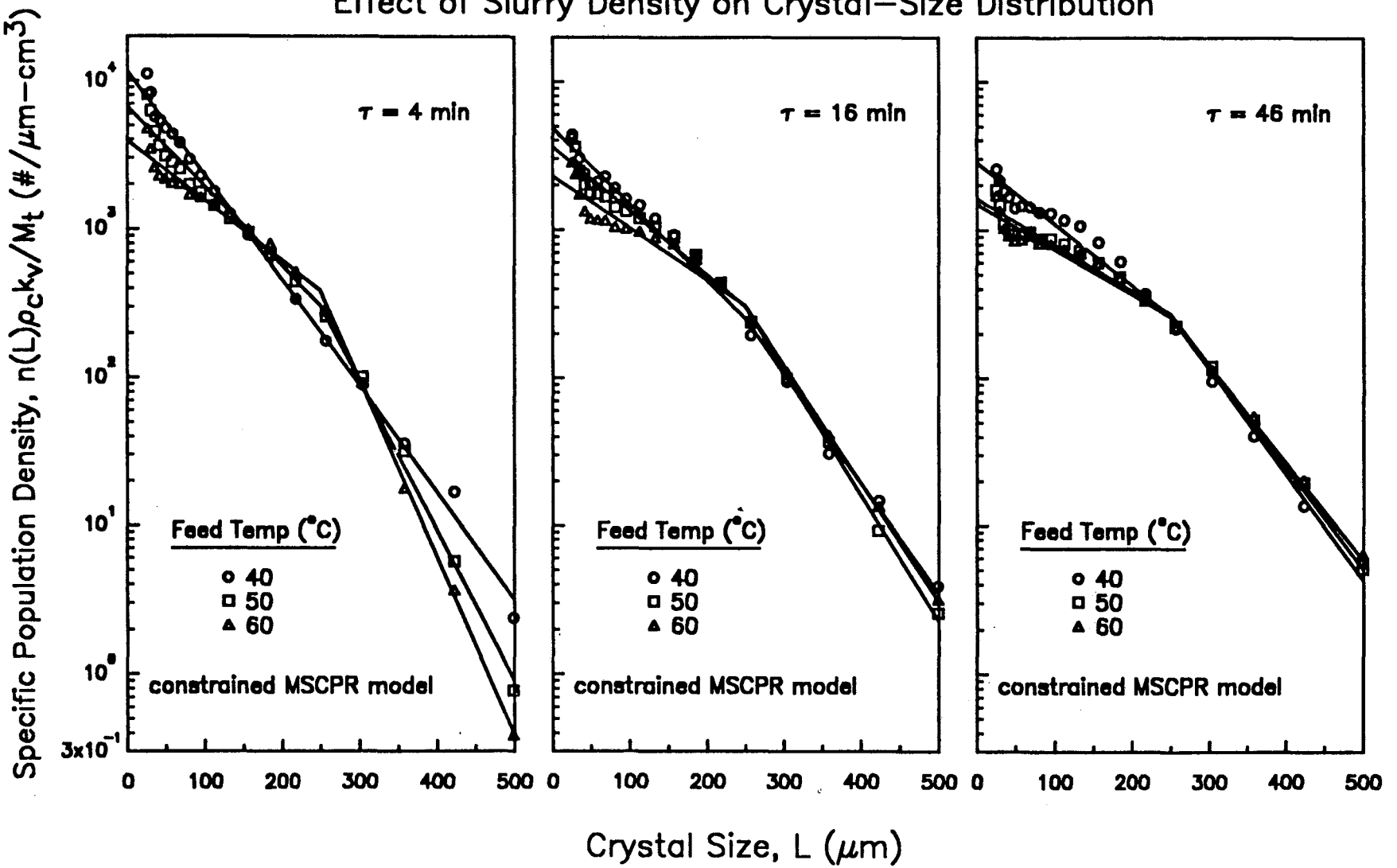

Figure 3.17

Dependence of Crystallization Kinetics on Slurry Density

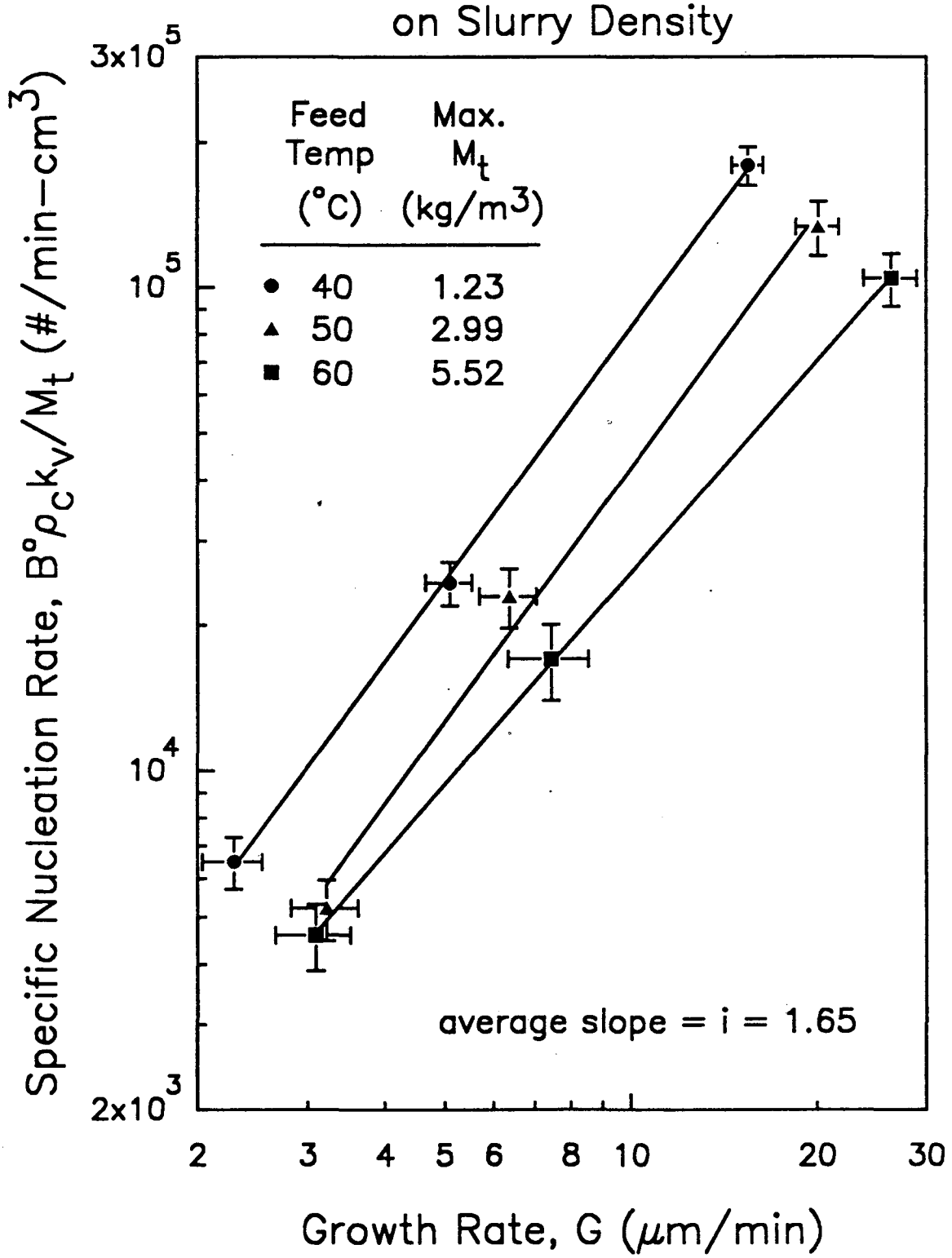

Figure 3.18

Dependence of Mass–Average Particle Size on Slurry Density

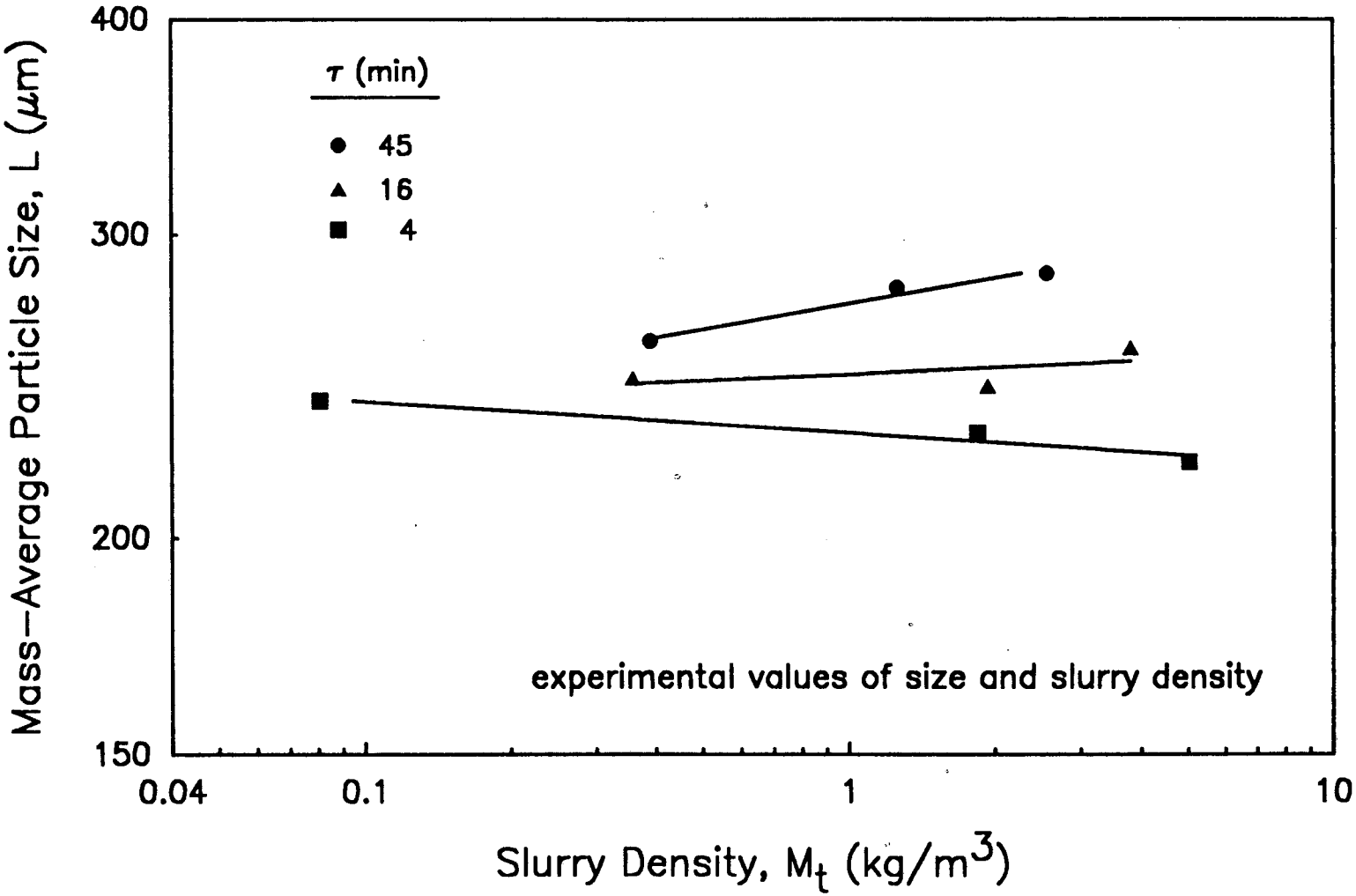

Figure 3.19

Effect of Residence Time and Slurry Density on Z

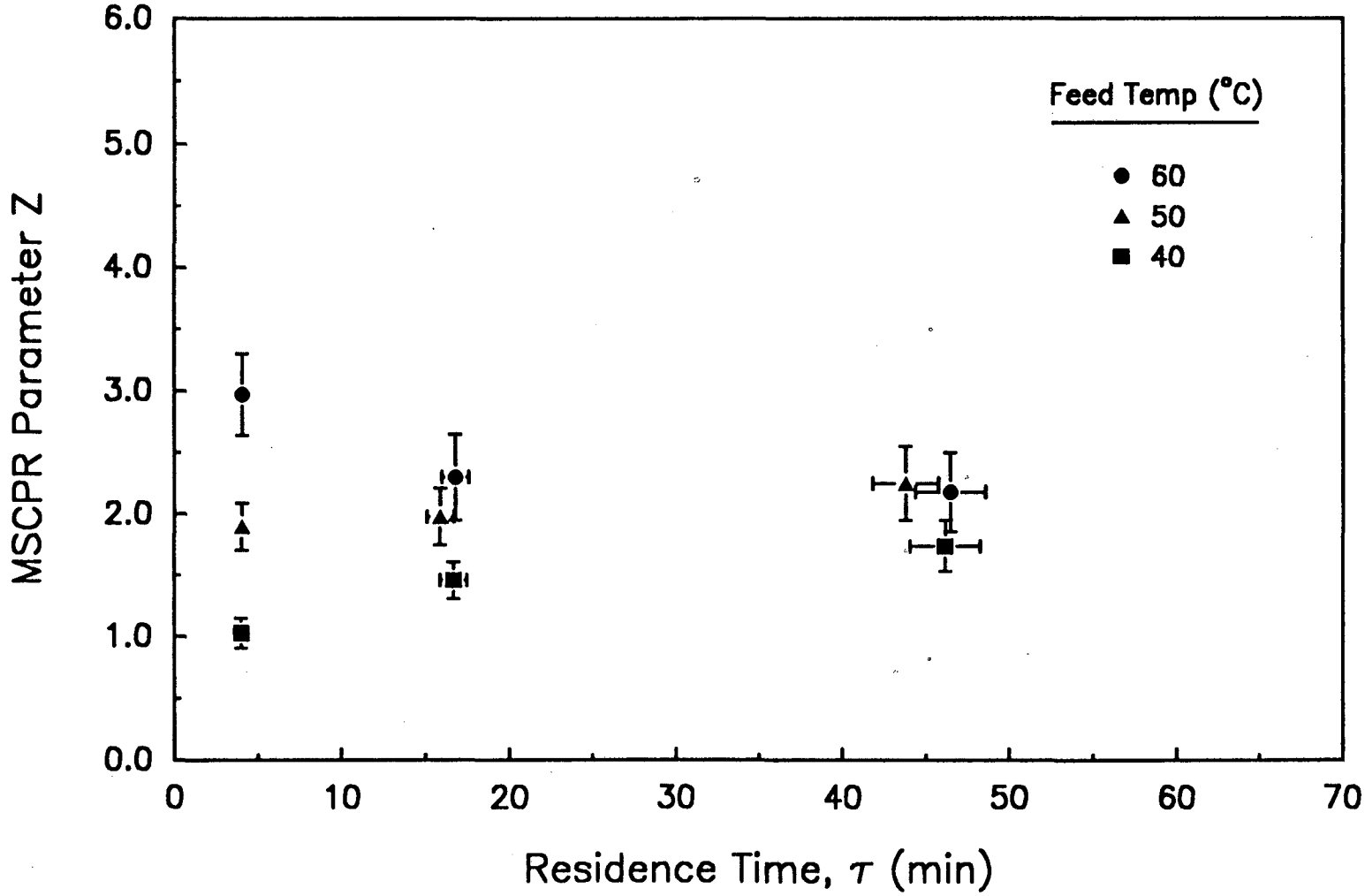

Figure 3.20

Comparison of Design Equation to Experimental Data

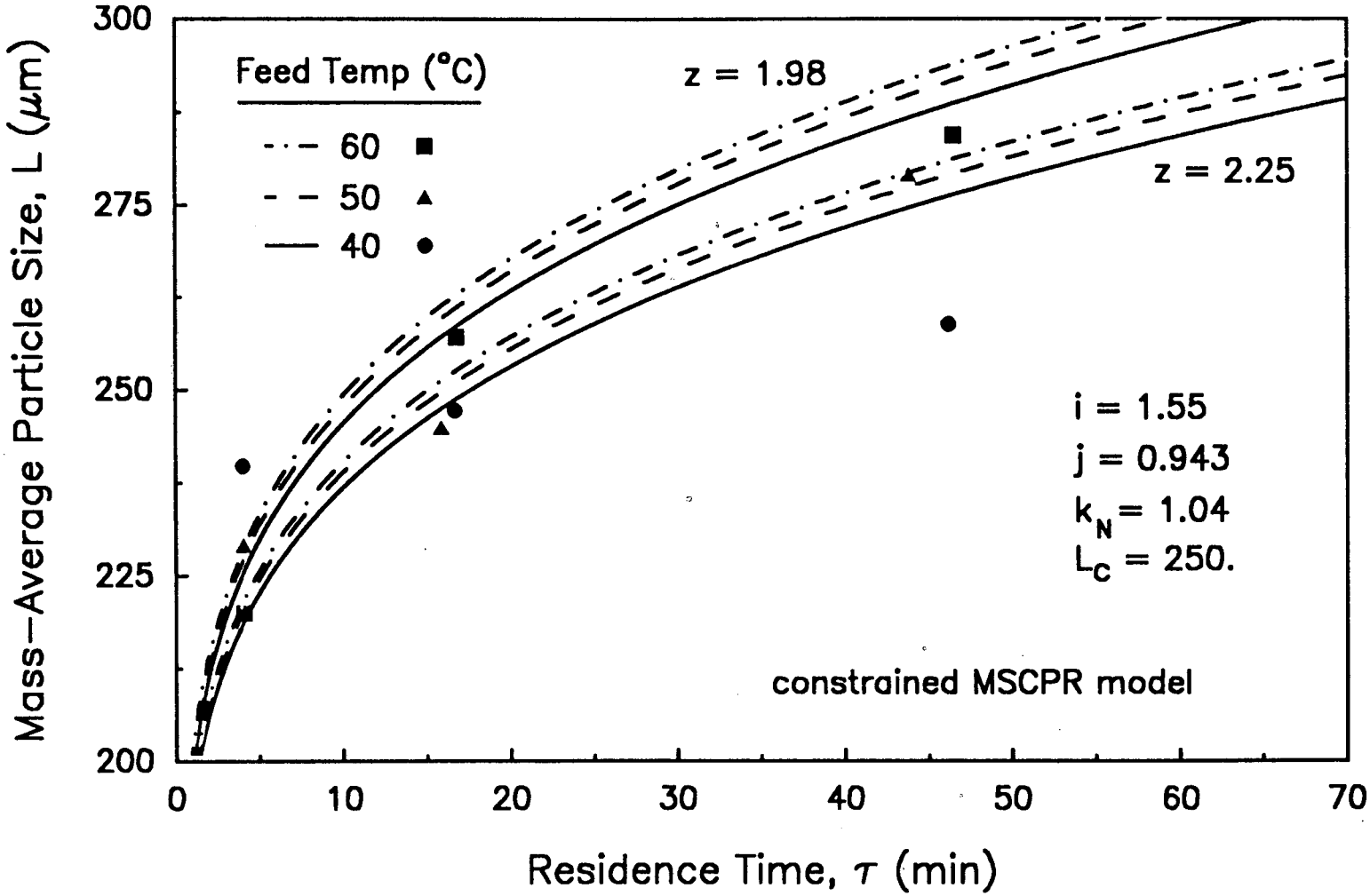

Figure 3.21

Effect of Power Input on CSD

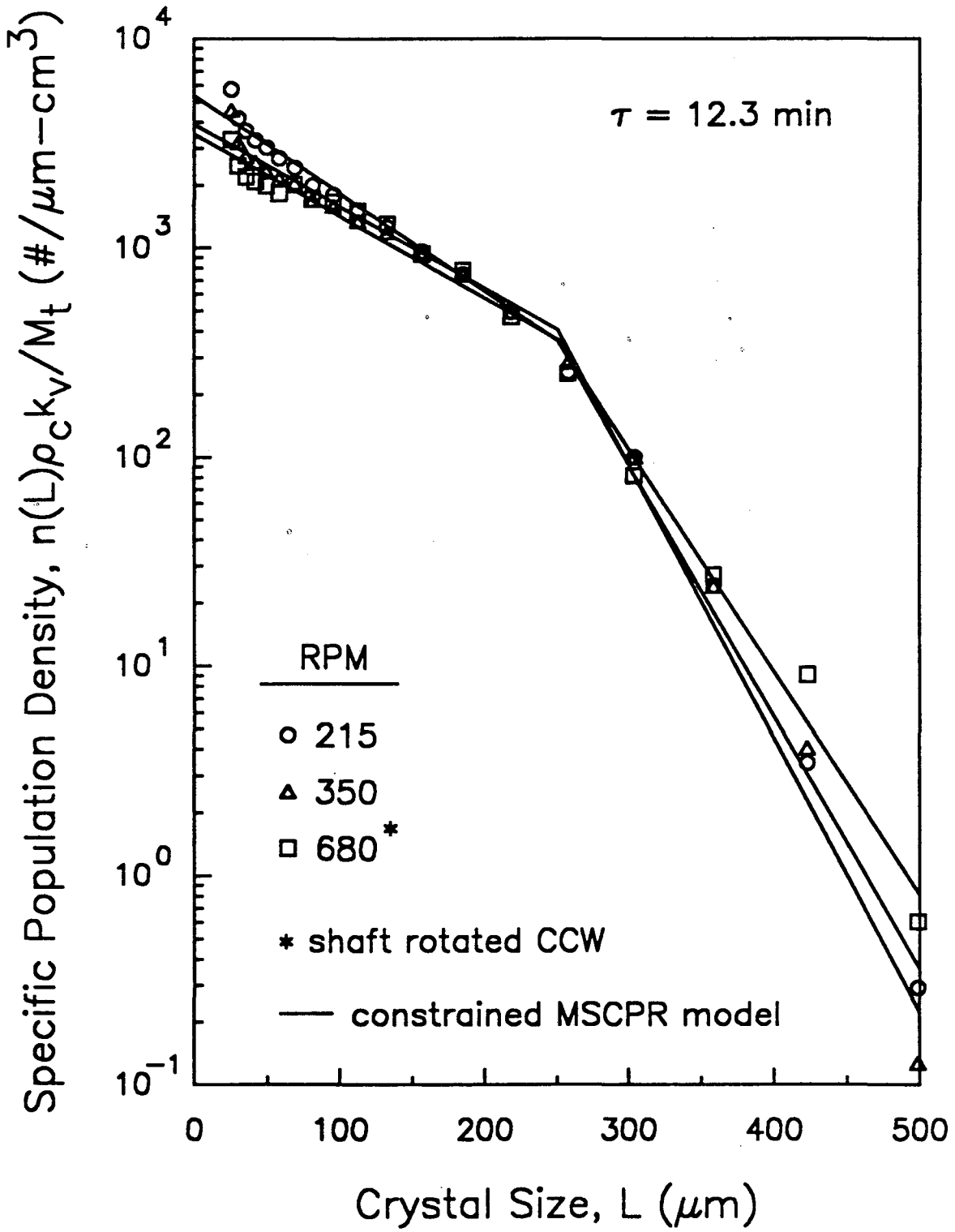

Figure 3.22

Effect of Impeller Power Input on Crystallization Parameters

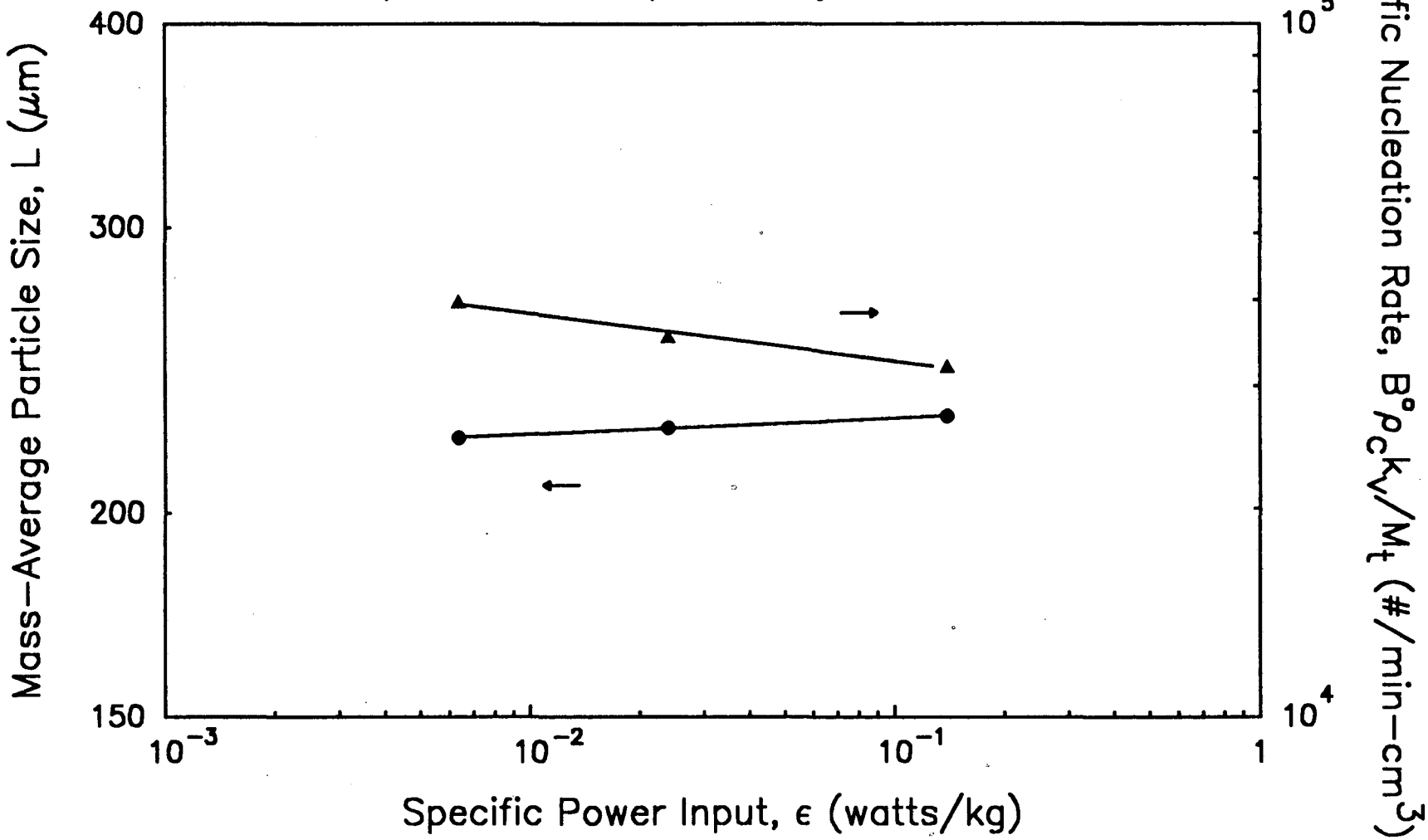

Figure 3.23

Effect of Water Concentration on Crystallization Kinetics

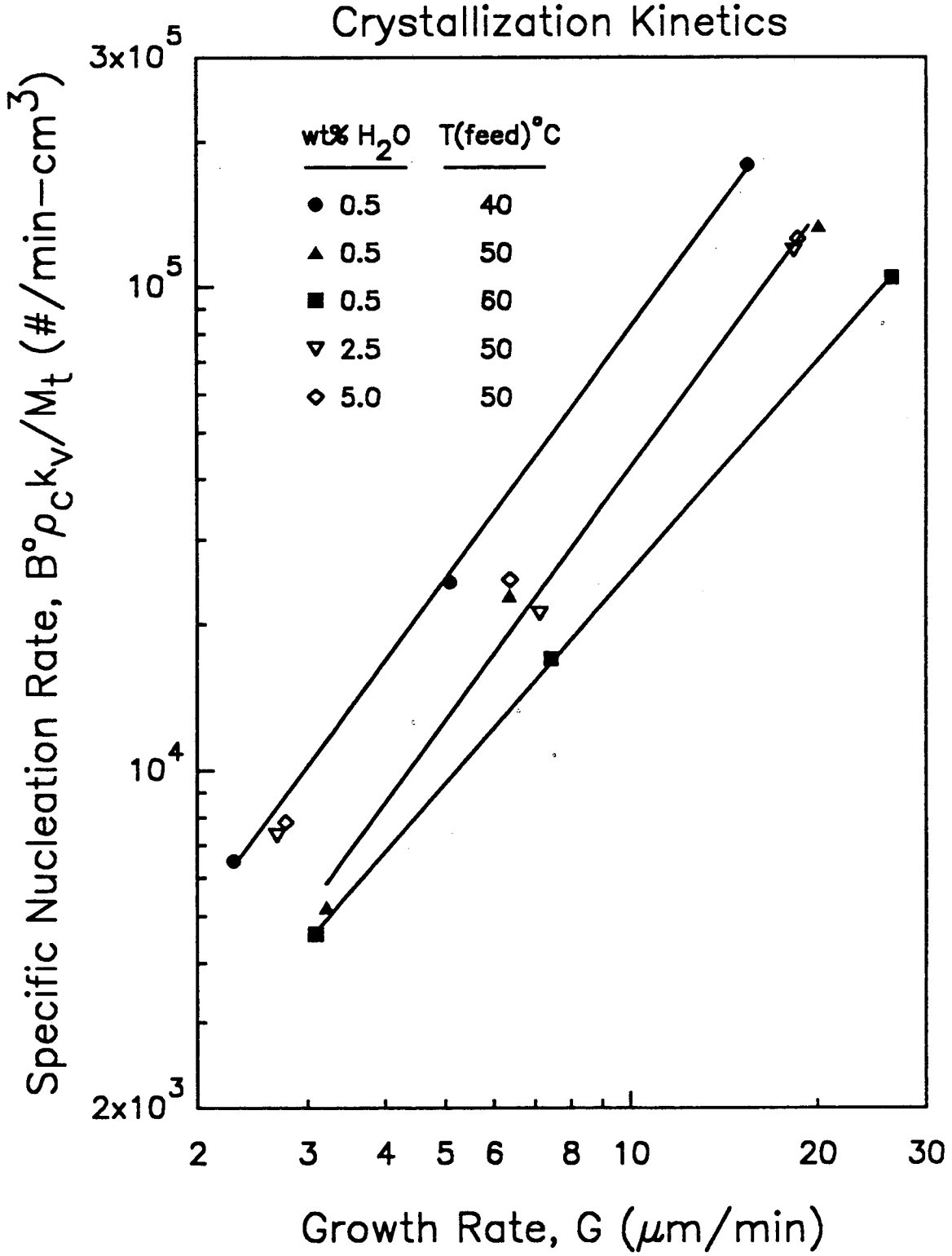

Figure 3.24

Predicted CSD from MSCPR Design Equation

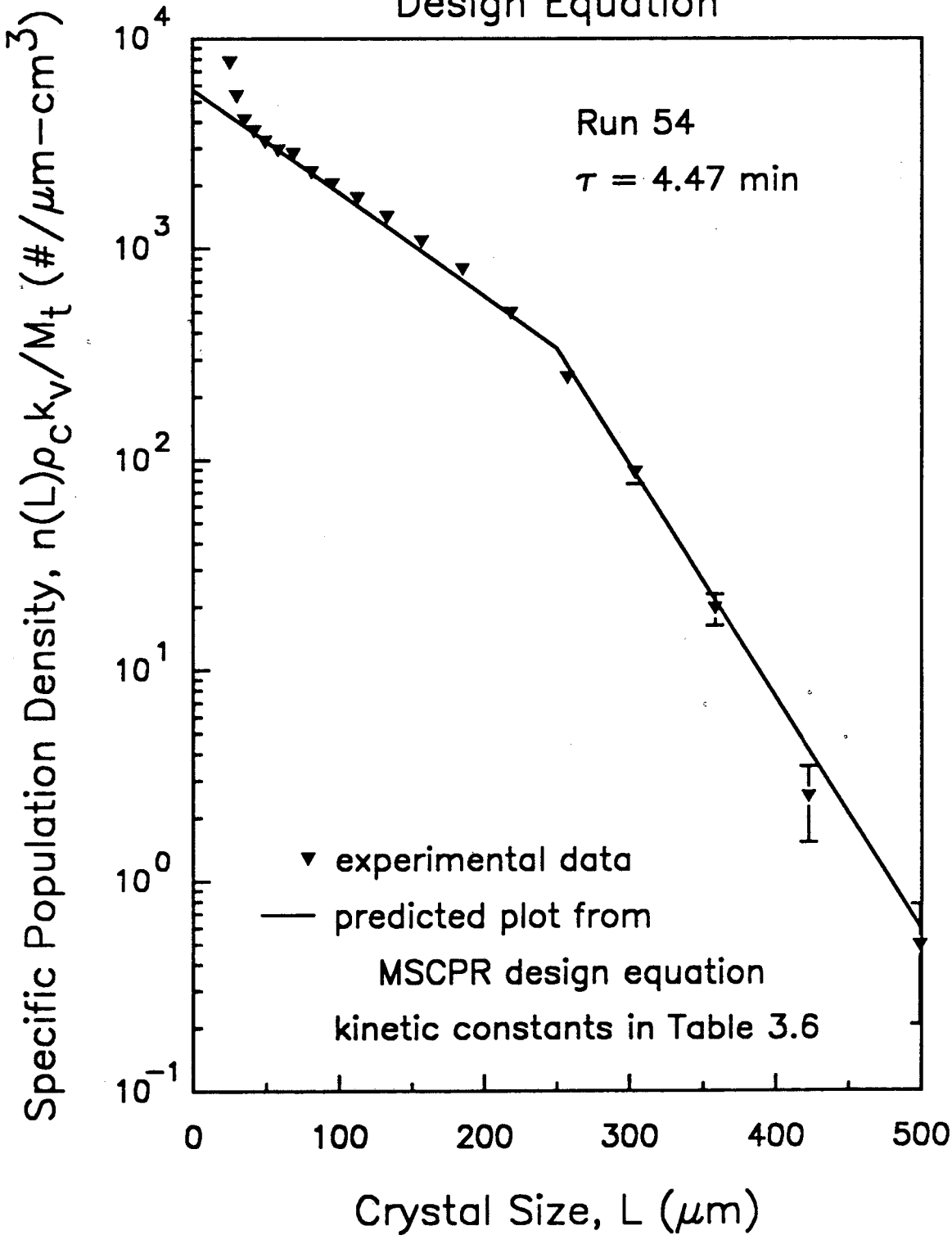

Figure 3.25 Photomicrograph of Sulfur Crystals from Back-Mixed Crystallization Run (p.143)

Figure 3.26 Photomicrograph of Sulfur Crystals from Fluidized-Bed Crystallization Run (p.144)

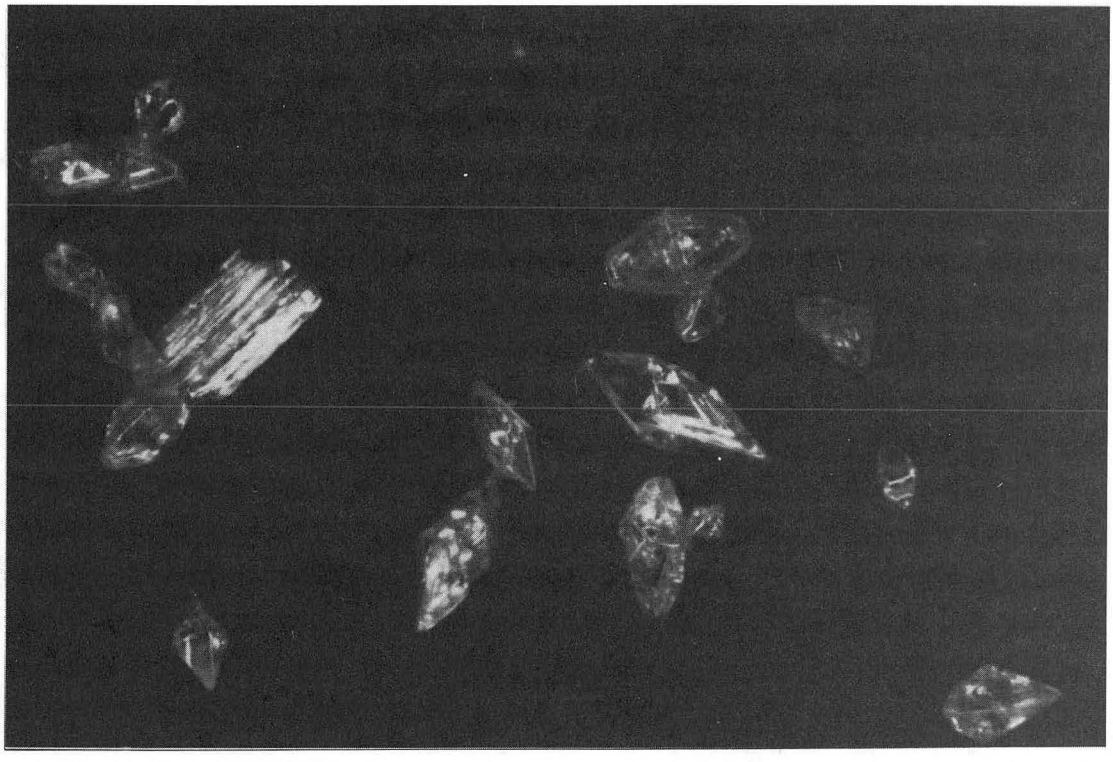

100 μm

XBB 899-7470

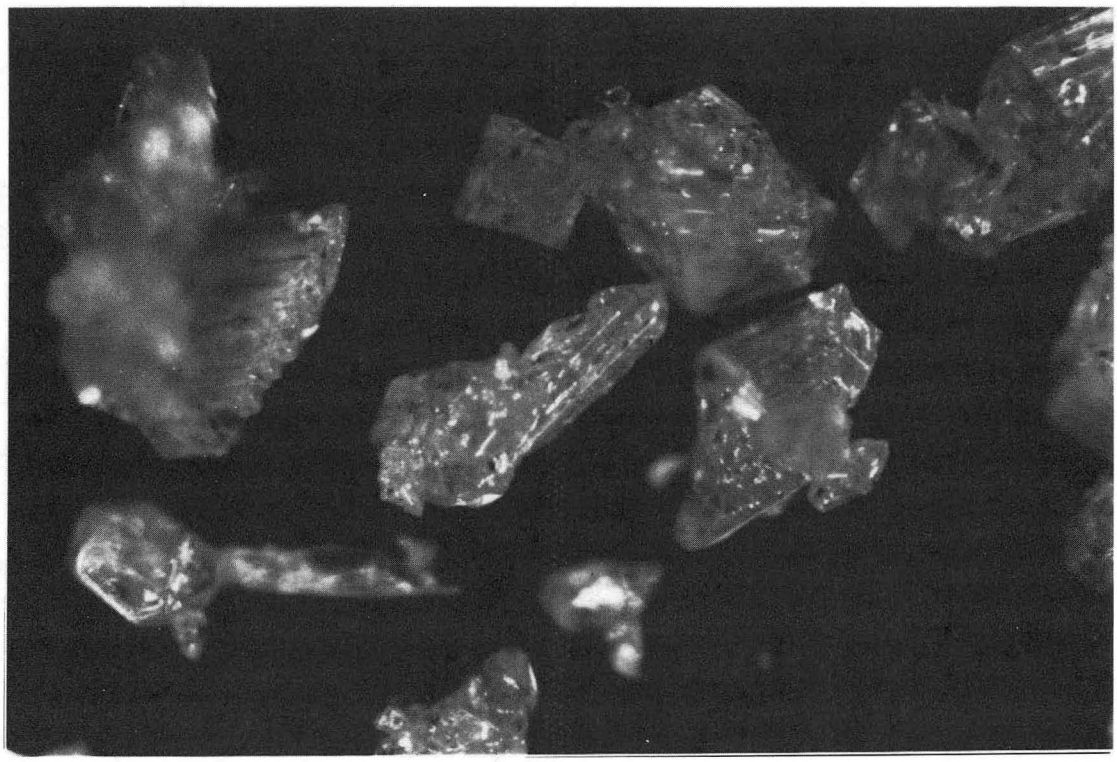

100 μm

XBB 899-7471

CHAPTER 4

REACTIVE CRYSTALLIZATION

4.1 Preface

In the University of California Berkeley Sulfur Recovery Process (UCBSRP), the elemental sulfur is recovered from the process solvent by crystallization. The sulfur is formed by the catalyzed liquid-phase reaction of H_2S and SO_2. The reaction and crystallization are performed in an integrated vessel to minimize the number of processing vessels and to maximize the thermal efficiency of the process. The process flow diagram of the UCBSRP is shown in Figure 1.1. The reactor/crystallizer is fed an H_2S-rich solution from the bottom of the primary absorber and is also fed an SO_2-rich solution from the bottom of the SO_2 scrubber. The H_2S is consumed in the SO_2-rich reactor/crystallizer to produce the crystalline sulfur product. The design criteria of the reactor/crystallizer are that the H_2S-free solvent recycled back to the primary absorber have a low H_2S concentration, that the sulfur crystals in the crystallizer effluent be large to facilitate their easy separation from the mother liquor, and that the volume of the reactor/crystallizer be of reasonable size.

Most of the reactive crystallizers used in the chemical industry produce inorganic salts from aqueous solutions, where the salt is formed by an acid-base reaction (Bamforth, 1965). A typical reactive crystallization operation is the production of ammonium sulfate from ammonia and sulfuric acid. In these operations, the acid-base reaction is practically instantaneous and the crystallization is performed in aqueous solutions. The chemistry of these reactions and the technology of the aqueous-based crystallization are both well known. The reactive crystallization of sulfur from H_2S and SO_2 is somewhat different in that the liquid-phase reaction is not instantaneous and the crystallization is not performed in an aqueous solution. The effect of the reaction between H_2S and SO_2 on the crystallization of sulfur from the polyglycol

ether solvent was investigated and the results are discussed below.

The catalyzed liquid-phase reaction of H_2S and SO_2 was studied by Neumann (1986). Complete conversion of the reactants to elemental sulfur was observed, where no other sulfur or sulfoxy species were detected. The thermal crystallization of sulfur from a polyglycol ether solution was addressed in Chapter 3. The information from these two investigations was combined to develop a model of the reactive crystallization of elemental sulfur from the process solvent. An experimental investigation was also performed to demonstrate the ability to produce sulfur crystals from the reaction of H_2S and SO_2 and to verify the theoretical model.

4.2 Reactor/Crystallizer Model

The reactive crystallization model is composed of two parts. The first part models the liquid-phase reaction of H_2S and SO_2 and the second part models the crystallization of sulfur. The time scale of the reaction is assumed much smaller than that of the crystallization so that the reaction and crystallization are treated sequentially. This assumption will be addressed later in Section 4.5. The benefit of this sequential treatment is that the reaction acts as an additional, independent source of solute during crystallization in the reactor/crystallizer.

4.2.1 Reaction Model

The irreversible liquid-phase reaction of H_2S and SO_2 to produce elemental sulfur and water has the following stoichiometry:

$$2\ H_2S + SO_2 \longrightarrow 3/8\ S_8 + 2\ H_2O \tag{4-1}$$

Neumann (1986) studied the reaction kinetics and found that the reaction is second order overall, first order for both reactants. The reaction is moderately exothermic, where the heat of reaction is approximately -28 kcal/mol of SO_2 reacted. The effect of the homogeneous catalyst concentration on the reaction rate was consolidated in the rate constant. As a result, the reaction rate expression is:

$$r = k_2 C_{H2S} C_{SO2} \tag{4-2}$$

where: C_{H2S} = concentration of H_2S in solution (mol/liter)

C_{SO2} = concentration of SO_2 in solution (mol/liter)

k_2 = second order rate constant (liter/mol-sec)

r = reaction rate (mol/sec)

The reaction is performed in the well-known continuous stirred-tank reactor (CSTR), for which the design equation is based on the fraction conversion of the limiting reactant (Hill, 1977). The fraction conversion is defined and the CSTR design equation is expressed as:

$$f_i = (C_{i,0} - C_i)/C_{i,0} \tag{4-3}$$

$$\tau = V/Q = C_{i,0}\,(f_{i,out} - f_{i,in})/(-r_{i,out}) \tag{4-4}$$

where: C_i = concentration of limiting component (mol/liter)

$C_{i,0}$ = concentration of limiting component in mixing-cup feed (mol/liter)

f_i = fraction conversion of limiting component

Q = volumetric flow rate through reactor (m^3/min)

$r_{i,out}$ = rate of disappearance of limiting reactant evaluated at reactor outlet conditions (mol/min)

τ = residence time of fluid in reactor (min)

V = volume of reactor (m^3)

The "mixing-cup" feed is used where multiple feeds are present. The mixing-cup component concentration is computed by combining all of the feeds. The rate expression and the design equation were combined to produce an equation that related the fraction conversion to the inlet reactant concentrations, the reaction kinetics, and the design variables. The resulting equation was rearranged to accommodate two dimensionless groups whose form was determined by the limiting reactant:

$$f_i = ([\alpha(\beta+1)+1] - \sqrt{[\alpha(\beta+1)+1]^2 - 4\alpha^2\beta})/2\alpha \tag{4-5}$$

Dimensionless Group	H_2S limiting	SO_2 limiting
α	$\tau k_2 C_{H2S,0}$	$2\tau k_2 C_{SO2,0}$
β	$2C_{SO2,0}/C_{H2S,0}$	$C_{H2S,0}/2C_{SO2,0}$

The first dimensionless group (α) is the Damköhler number, and expresses the relative rates of the macroscopic residence time (τ) and the reaction time ($k_2C_{i,0}$). The second dimensionless group (β) is the ratio of the reactant concentrations in the mixing-cup feed. The feed to the reactor has excess SO_2 when $2C_{SO2,0}/C_{H2S,0} > 1$, whereas the feed has excess H_2S when $2C_{SO2,0}/C_{H2S,0} < 1$.

Equation (4-5) was used to calculate the fractional conversion of the limiting reactant for a given residence time, rate constant, and inlet concentrations of reactants. From the change in concentration of the limiting reactant, the change in concentration of the other reaction constituents are then calculated from the stoichiometry of Equation (4-1).

4.2.2 Crystallization Model

The crystallization of sulfur from polyglycol ether solutions was studied in Chapter 3. The crystallization kinetics expression produced from that thermal crystallization study is used here. The solute mass balance is different than that for the thermal crystallization because of the additional feeds and inputs. The solute mass balance is expressed as follows:

$$Q_1C_1 + Q_2C_2 - Q_3C_3 + r_{S8}V = Q_3M_T(\max) \tag{4-6}$$

where: C_k = concentration of sulfur (S_8) in k^{th} stream (mol/liter)

k = integer denoting an inlet or outlet stream
1,2 = feeds; 3 = effluent

$M_T(\max)$ = maximum slurry density of sulfur crystals (kg/m^3)

Q_k = volumetric flow rate of kth stream (m^3/min)

r_{S8} = rate of appearance of sulfur (S_8) from reaction [= $r/(3/8)$] (mol/sec)]

The left-hand side of Equation (4-6) represents dissolved sulfur flowing in and out of

the reactor/crystallizer (Q_kC_k) and also the appearance of dissolved sulfur formed by the reaction ($r_{S8}V$). The right-hand side of the equation is the total amount of solid sulfur produced from the reactor/crystallizer. For a mixed-suspension, mixed-product removal (MSMPR) crystallizer, this maximum solids concentration is equal to the product solids concentration. For the experimental crystallizer, which is characterized by the mixed-suspension, classified-product removal (MSCPR) crystallizer, the maximum solids concentration is separated into two entities: the solids produced as product and the solids removed from the active volume of the crystallizer by the internal classification mechanism. Therefore, the solute mass balance for the experimental crystallizer is written as:

$$Q_1C_1 + Q_2C_2 - Q_3C_3 + r_{S8}V = Q_3M_T + Q_3(z-1)M_T^+ \tag{4-7}$$

where: M_T = slurry density of all crystals in suspension (kg/m^3)

M_T^+ = slurry density of over-sized crystals (kg/m^3)

z = MSCPR model parameter [= 2.25]

The MSCPR design equation is required to predict the crystal-size distribution and mass-average particle size of the sulfur crystals produced from the experimental crystallizer. The derivation of the design equation and its use to predict the crystal-size distribution and mass-average particle size are detailed in Chapter 3. The expressions for the crystallization kinetics (Equations (4-8) and (4-9)), slurry density, mass-average particle size, and the MSCPR design equation are:

$$B^o = k_N \epsilon^h G^i M_T^j \tag{4-8}$$

$$n^o\rho_C k_V/M_T = k_N\rho_C k_V G^{i-1} M_T^{j-1} \tag{4-9}$$

$$M_T = M_T(\max)/[1 + B(z-1)\exp((z-1)L_C/G\tau))(n^o\rho_C k_V/M_T)(G\tau/z)^4] \tag{4-10}$$

$$\mathcal{L} = f_2 G\tau \tag{4-11}$$

$$\tau = \left[\frac{f_1\rho_C k_V k_N \epsilon^h M_T^{j-1} \mathcal{L}^{i+3}}{f_2^{i+3}}\right]^{1/i-1} \tag{4-12}$$

where: B^o = nucleation rate [= n^oG] (#/min-cm^3)

B = fxn (τ, G, z, L_c) [see Chapter 3]

f_1, f_2 = fxn (τ, G, z, L_c) [see Chapter 3]

G = crystal growth rate (μm/min)

h = exponent for the specific power input [= 0]

i = kinetic order [= 1.55]

j = secondary nucleation order [= 0.943]

k_N = kinetic constant [= 1.04]

k_V = crystal volumetric shape factor [= $\pi/6$]

L_c = MSCPR model parameter [= 250.] (μm)

$\mathscr{L}$ = mass-average particle size (μm)

$n^o \rho_C k_V / M_T$ = specific nuclei population density (#/μm-cm^3)

ϵ = specific power input (watts/kg solution)

ρ_C = crystal density (kg/m^3)

τ = residence time of crystals in crystallizer [= V/Q_3] (min)

Equations (4-8) through (4-12) were used to calculate the mass-average particle size and crystal-size distribution of the sulfur crystals for the residence times and maximum solids concentrations observed from the experimental runs. The iterative method of solving the above equations is listed in Appendix B.

4.3 Experimental Apparatus

4.3.1 Back-Mixed Crystallizer

The apparatus used to perform the back-mixed reactive crystallization of sulfur from the polyglycol ether solvent was constructed from the same back-mixed apparatus used in the thermal crystallization study. As modifications, the crystallizer feed lines were altered to facilitate the addition of the H_2S and SO_2 solutions to the experimental crystallizer. A schematic diagram of the back-mixed reactive crystallizer is shown in Figure 4.1. Two 20-liter polyethylene carboys were placed overhead to feed the gas

solutions (one for H_2S and the other for SO_2) to the crystallizer. The carboys both had dip tubes which were connected to H_2S and SO_2 gas cylinders, respectively, to sparge the gases into the solvent residing in each carboy. Rotameters, needle valves, and shut-off valves were put in-line to control and measure the addition of each gas. The dip tubes were also connected, with necessary valves, to a nitrogen supply so that the constant-head feed tanks would deliver steady flow rates as the liquid level dropped in the carboys. The nitrogen supply was pressurized slightly by using an external bubble tube. Gas lines from the top of the carboys were routed to concentrated caustic scrubbers to absorb excess gases while sparging the solvent. The solution feed line from each constant-head tank had an in-line rotameter, needle valve, and shut-off valves to control and measure the addition of each solution to the crystallizer. The feed lines also had fittings equipped with septums to enable sampling of the gas solutions.

The solutions were fed into the 2-liter glass crystallizer through glass dip tubes, which introduced the solutions just above the rotating impeller. The glass impeller was the same as in the thermal crystallization experiments and was rotated clockwise to produce a downward flow of fluid. The temperature of the crystallizer contents was maintained at $30^{o}C$ by pumping cooling water through its jacket. The temperature was monitored using a thermocouple which was placed in a small glass dip tube. A glass tube was located in the exit port of the crystallizer, as in the thermal crystallization study, to reduce the preferential removal of large crystals. The vapor space of the crystallizer was completely sealed to eliminate the escape of H_2S or SO_2. The rotating impeller shaft was sealed with a well-lubricated, ground-glass fitting. The crystallizer vapor space was also pressurized slightly by using a nitrogen supply and an external bubble tube. The liquid volume in the crystallizer was controlled using the photoelectric level controller which actuated a solenoid valve on the crystallizer effluent line.

The crystallizer effluent line emptied into a 60-liter polyethylene solvent holding tank. A dip tube was located in the tank and connected to a nitrogen source so that the crystallizer effluent could be stripped of residual gases after each experimental run. The tank was outfitted with a gas line which was routed to a caustic scrubber to clean residual gases from the stripped gas. The solvent holding tank also had an immersed heat exchanger and stirring device to mix the solution and control the solution temperature. A gear pump was connected to a port on the bottom of the solvent holding tank for pumping clean solution up to the constant-head tanks.

4.3.2 Fluidized-Bed Crystallizer

The apparatus used to perform the fluidized-bed reactive crystallization of sulfur from a polyglycol ether solvent had the same set-up as the fluidized-bed apparatus used in the thermal crystallization study. The constant-head feed tanks and feed lines for the addition of the H_2S and SO_2 solutions to the crystallizer were the same as those discussed in the back-mixed crystallizer. A schematic diagram of the fluidized-bed reactive crystallizer is shown in Figure 4.2.

4.4 Experimental Method

The operation of the reactive crystallizer was semi-continuous. The solvent in each feed tank was loaded with either H_2S or SO_2, the resulting gas solutions were run through the crystallizer, and the crystallizer effluent was treated before pumping it back up to the feed tanks. Enough solvent was in inventory to run the crystallizer for at least ten residence times. The solvent used was triethylene glycol dimethyl ether (Triglyme), the same solvent as that used in the thermal crystallization study. The homogeneous catalyst and its concentration in the solvent were 3-pyridyl carbinol (3PC) and 0.015 M, respectively. The catalyst and its concentration were chosen because reaction rate data were available for them (Neumann, 1986). The operating temperature of the crystallizer remained constant at 30°C throughout all of the runs, as

in the earlier thermal crystallization experiments.

4.4.1 Back-Mixed Crystallizer Operation

A typical run began by setting the sulfur concentration in the feed solutions by agitating the clean solvent in the solvent holding tank with excess solid sulfur at 20°C. The temperature of the solvent holding tank was maintained at approximately 20°C by pumping refrigerated cooling water through the immersed heat exchanger. The sulfur concentration in the solvent was equivalent to its saturation value at 20°C, and was below its room temperature value to prevent sulfur precipitation in the feed lines and feed vessels. The excess solid sulfur was allowed to settle, and the clear liquid was pumped into the two overhead feed tanks. The sulfur/solvent solutions in the two constant-head feed tanks were then sparged with either H_2S or SO_2 to load the solvent with the corresponding gas. The gases which were not absorbed in the solvent were scrubbed in the caustic wash before being vented to the atmosphere. The flows of the gases were monitored by two rotameters so that an estimate of the gas concentration in each feed tank could be made. After the sparging was stopped, the H_2S solution in one tank and the SO_2 solution in the other were sampled to measure the concentration of dissolved gas. The two tanks were pressurized to approximately 50 cm water by bubbling nitrogen through a vertical stand pipe filled with water. The feed solutions were then ready for a reactive crystallization run.

The two gas solutions were fed to the crystallizer and their flows measured by in-line rotameters. The solutions were introduced into the stirred contents just above the downward-pumping rotating impeller to aid in rapid mixing of the reactants. The crystallizer contents were agitated vigorously (RPM = 680 instead of 350 as in thermal crystallization) to maximize mixedness in the wetted volume and to minimize the crystalline fouling on the crystallizer internals. The crystallizer temperature of 30°C was maintained by manually controlling the temperature of the refrigerated cooling water pumped through the crystallizer jacket. The temperature of the cooling water

was 25°C or higher, so that the maximum temperature difference across the glass heat-transfer surface was 5°. The level controller intermittently purged five percent of the total wetted crystallizer volume to the solvent holding tank. The total wetted volume in the crystallizer was measured from the graduations on the side of the crystallizer vessel and was set by the variable on/off delay times for the level controller. The pressure in the crystallizer was maintained at approximately 40 cm water by bubbling nitrogen through a vertical stand pipe. When starting a run, the crystallizer wetted volume was seeded with sulfur crystals to reduce the time required to achieve steady-state operation.

After steady-state operation was reached, three effluent slurry samples were taken and the crystal-size distribution measured using the particle-size analyzer. The analysis technique was the same as that used in the thermal crystallization study. During each run, two samples of each gas solution were taken from the septum port using a 10-milliliter syringe. The gas concentrations in the solutions were determined using the following acid/base reactions:

$$2NaOH + SO_2 = Na_2SO_3 + H_2O \tag{4-13}$$

$$NaOH + H_2S = NaHS + H_2O \tag{4-14}$$

For each sample, a solution of sodium hydroxide was placed in a 250-milliliter Erlenmeyer flask. A magnetic stirring bar was placed inside the flask and a septum fitted over the mouth of the flask. The gas solution was then injected slowly into the stirred sodium hydroxide solution. The mixture was stirred for approximately four minutes to allow the reaction to go to completion. The excess sodium hydroxide was titrated with hydrochloric acid, using phenolphthalein as the indicator. The gas concentration was then computed from the volume of acid added and the masses of the sodium hydroxide solution and the injected gas solution. This technique was standardized and yielded gas concentration errors less than five percent.

After each run, the solids/solvent slurry in the solvent holding tank was degassed

and dewatered by sparging the contents at elevated temperature ($50^{o}C$) with nitrogen. The off-gas was scrubbed in a caustic wash before being vented to the atmosphere. The water concentration in the solvent was measured between runs using the same gas chromatography technique as that discussed in Chapter 3. The 3PC concentration in the solvent was not monitored because a suitable analysis technique was not found.

4.4.2 Fluidized-Bed Crystallizer Operation

The preparation of the feed solutions for the fluidized-bed crystallizer was the same as that for the back-mixed crystallizer, discussed in Section 4.4.1. The operation of the crystallizer and external devices to provide the fluidized bed was the same as in the thermal crystallization study in Chapter 3. In summary, the flow of clear mother liquor up the elutriation leg kept sulfur crystals suspended in the reactor/crystallizer until the size of the crystals was large enough to overcome the fluid velocity in the elutriation leg.

4.5 Back-Mixed Crystallizer Results and Discussion

The reactive crystallization apparatus was used to produce crystals of elemental sulfur from the liquid-phase reaction of H_2S and SO_2. The operating conditions of the reactive crystallization runs were used as input data for the reactor/crystallizer model, described in Section 4.2, to predict the solids concentration and crystal-size distribution of the sulfur crystals. The reactor/crystallizer model is based on a continuous stirred-tank reactor (CSTR) and a mixed-suspension classified-product removal (MSCPR) crystallizer.

4.5.1 Validity of Reactor/Crystallizer Model

The reactor/crystallizer model is based on the assumption that the reaction and crystallization occur sequentially. This assumption is verified by comparing the characteristic times scales for the reaction and crystallization. The time scale for the reaction is expressed as $(k_2C_{i,0})^{-1}$, which is part of the Damköhler number. The time

scale for the crystallization is the residence time, τ. If the two time scales are equal in magnitude, then the reactive crystallization should be modeled as two parallel processes, whereas if the reaction time scale is much less than the crystallization time scale, then the assumption used in the reactor/crystallizer model is justified. To compute the time scales, values for the three variables (k_2, $C_{i,0}$, and τ) are required. From Neumann (1986), the value of the second-order rate constant, k_2, for the liquid-phase reaction of H_2S and SO_2 in Triglyme with a 0.015 M 3PC catalyst concentration is about 20 liter/mol-s. From the various applications of the UCBSRP, the typical limiting reactant concentration in the reactor feed stream is approximately 0.03 mol/liter. From these values of k_2 and $C_{i,0}$, the time scale for the reaction is about 2 seconds. Note that this reaction time scale is independent of the type of crystallizer. The smallest residence time the reactor/crystallizer would operate is approximately 5 minutes or 300 seconds. Since the time scale for crystallization is roughly two orders of magnitude larger than the time scale for reaction, the sequential treatment of the reaction and crystallization is appropriate.

4.5.2 Use of the Reactor/Crystallizer Model

From the residence time, inlet gas concentrations, and gas solution flow rates measured in the experimental reactive crystallization runs, the fraction conversion of the limiting reactant was computed using Equation (4-5). The dependence of fraction conversion on the two dimensionless groups, the Damköhler number and the ratio of the reactant concentrations in the mixing-cup feed, is illustrated in Figure 4.3. When $2C_{SO2,0}/C_{H2S,0} = 1$, the reactants are fed to the reactor in the stoichiometric ratio prescribed by Equation (4-1). For a given residence time, this ratio yields the lowest fraction conversion. With excess H_2S or excess SO_2 present, the fraction conversion increases. Similarly, as the Damköhler number is increased, the fraction conversion increases. For a given rate constant and inlet concentration of the limiting reactant, the Damköhler number is increased by increasing the residence time. From the curves

in Figure 4.3, the operation of the reactor/crystallizer should require at least ten percent excess reactant and a Damköhler number larger than 100 to yield an acceptable (> 0.9) value for the fraction conversion.

The results of the reactor model were used to compute the mass balance of the four reaction constituents: H_2S, SO_2, S_8, and H_2O. The sulfur solubility correlation in Chapter 2 was used to calculate the sulfur concentrations in the feeds and effluent. Using Equation (4-6), the maximum slurry density of sulfur crystals was calculated. The maximum slurry density and the residence time were used to compute the mass-average particle size and the crystal-size distribution of the sulfur crystals from Equations (4-8) through (4-12). Sample calculations for the reactor/crystallizer model are listed in Appendix C.

Detailed operating conditions of the reactive crystallization runs are listed in Table 4.1. The concentrations of the dissolved gases in the experimental feed solutions were different than those fed to the reactor/crystallizer in the various applications of the UCBSRP. The concentrations of the gases in the experiments varied from about equal to roughly six times greater than those proposed for the process. The discrepancy between the experimental and process concentrations is the result of two factors. First, the sulfur concentration in the experimental feeds was two to five times less than that in the feeds to the process reactor/crystallizer. The sulfur saturation temperatures in the proposed process feeds range from 45° to $77^{o}C$, and as a result, the crystallization of sulfur results from both the reduction in temperature of the process solvent and from the liquid-phase reaction. In the experimental feeds, the sulfur saturation temperature was $20^{o}C$. Since the experimental crystallizer was operated at $30^{o}C$, the sulfur formed by the reaction was dissolved in the solvent to its saturation limit before crystallizing out of the solvent. Therefore, larger gas concentrations were required in the experimental feeds to produce sulfur which would crystallize from solution. Second, larger gas concentrations in the experimental feeds

were used to produce larger slurry densities than were produced from the thermal crystallization runs. These runs with larger slurry densities were made to test the applicability of the crystallizer model outside the range of slurry densities from which the model was derived.

4.5.3 Comparison of the Experimental and Model Results

A summary of the feed conditions for the reactive crystallization runs is also listed in Table 4.1. The ratio of the reactant concentrations in the mixing-cup feed and the Damköhler number are based on the assumption that the liquid density of the gas solutions is equal to the pure liquid density. This assumption was checked by calculating the mixture molar volume using Amagat's Law and the maximum gas concentrations observed in the experiments. A maximum error of 1.5 percent between the pure liquid density and the mixture liquid density was calculated and deemed acceptable. The fraction conversion of the limiting reactant (H_2S or SO_2) was calculated from Equation (4-5) and the values are all above 99+ percent conversion.

The maximum slurry density was calculated from Equation (4-6). The predicted slurry density is that produced from the MSCPR crystallizer model, wherein the larger crystals have a smaller residence time in the crystallizer. The reduction of the slurry density from the maximum to the predicted MSCPR is significant and is a consequence of the preferential removal of large crystals. No experimental slurry density data are available for the reactive-crystallization runs because quickly filtering the solids from the mother liquor was difficult. This difficulty was a result of the gross nucleation that occurred when a slurry sample was removed from the crystallizer. Produced from the completion of the reaction (f_i = 0.998 to 1), the small mass of many nuclei plugged the coarse filter paper and slowed filtration to a trickle. The maximum slurry densities for the reactive crystallization runs were at most three times greater than the maximum slurry densities observed in the thermal crystallization study. The agreement found between the measured and predicted mass-average particle size values

is very good. In addition, the crystal-size distributions predicted from the model compare well with those measured during the experimental runs. Figures 4.4 through 4.6 show the ability of the reactor/crystallizer model to predict the crystal-size distributions of the three runs listed in Table 4.1. Not only do the crystallization kinetics predict the crystal-size distributions, but the values of z and L_c determined from the thermal crystallization appear applicable as well. The slopes of the predicted plots on both sides of the "knee" coincide with the experimental crystal-size distributions. The model also conforms with the distributions from runs where the slurry densities were greater than the range studied in the thermal crystallization runs.

Although the crystallization kinetics of the sulfur/solvent system was obtained in a non-ideal, MSCPR crystallizer, the kinetics may be used to design a crystallizer of any configuration with or without classification. The decoupling of the kinetics from the classifying mechanism, which was observed in and modeled for the experimental crystallizer, enables one to use the kinetics expression in modeling any type of crystallizer.

4.5.4 Effects of Reaction on Crystallization

The operation of the experimental reactor/crystallizer was much the same as in the thermal crystallization study. However, the reaction did affect several items. As discussed earlier, the measurement of the slurry density was very difficult because of the inability to quickly filter the mother liquor from the crystals. An additional problem was sulfur encrustation on all wetted surfaces in the crystallizer when the impeller was rotated at low speed (325 RPM). The encrustation was so severe that all of the sulfur was deposited on the internal surfaces, and as a result, it produced a clear mother liquor. This gross encrustation was not observed in the thermal crystallization study, where the impeller speed was also 325 RPM. The encrustation was reduced significantly when the impeller was rotated much faster, at 680 RPM. Encrustation was still slightly visible for experimental runs where the solids

concentration and throughput were large. The gross encrustation at low RPM is believed to be a result of insufficient mixing of the reactants in the crystallizer volume. Treleaven and Tobgy (1971) report that a CSTR with separate reactant feed streams and with insufficient mixing operates as a number of batch systems reacting in parallel. This suggests that the supersaturation of the reaction product (the solute) in particular fluid elements is high while the supersaturation in other fluid elements is low. As a result, the total volume of the experimental crystallizer is not utilized in crystallizing the solute as it was in the thermal crystallization study. Perhaps the highly supersaturated fluid elements deposited the solute onto the vessel surfaces instead of forming nuclei in the fluid element. Garside and Tavare (1985) discuss the effect of mixing on the crystal-size distribution and show that poor mixing produces highly nonlinear crystal-size distributions. Referring to Figures 4.4 through 4.6, these nonlinearities were not observed in this study.

4.6 Fluidized-Bed Crystallizer Results and Discussion

The reactive crystallization apparatus was operated with the withdrawal of sulfur operated in a fluidized-bed arrangement in an attempt to produce large, mono-sized sulfur crystals from the reaction of H_2S and SO_2. The operating conditions of the reactive crystallization run are the same as those for Run 64 and are listed in Table 4.1. The results from the experimental run were similar to the results from the thermal crystallization fluidized-bed runs. The sulfur crystals were still observed to be agglomerates, but the sizes of the agglomerates, dictated by the fluid velocity up the elutriation leg, were too big to measure in the particle-size analyzer.

4.7 Sulfur Purity and Morphology

The purity of the sulfur crystals produced from the reactive crystallization runs was determined by a technique that combines gas-chromatography and gravimetry. This technique is discussed in Chapter 3. The results of the sulfur purity analyses for

sulfur produced from the reactive crystallization runs are comparable to the results from the thermal crystallization runs. The purity of the sulfur crystals produced from Run 63, a fluidized-bed reactive crystallization run, is approximately 99.8 percent. The Triglyme concentrations determined from two independent analyses of the crystals from Run 63 show that the sulfur purity analysis yields reproducible results. The purity of the sulfur crystals produced from the reactive crystallization runs differs only slightly from the purity obtained in the thermal crystallization runs.

A determination of the amount of solvent residing on the crystal surface relative to that residing in the occlusions was made for sulfur crystals produced from Run 66, a back-mixed reactive crystallization run. The sulfur crystals from Run 66 were initially removed from the mother liquor by filtering under vacuum and then quickly washed with an ethanol/water mixture. A small sample of these crystals was analyzed and found to have a Triglyme concentration of 0.29 weight percent. The sulfur crystals were then washed vigorously with several doses of an ethanol/water mixture. A small sample of these crystals were again analyzed, which gave a Triglyme concentration of 0.20 weight percent. Obviously, some of the solvent on the surface of the sulfur crystals was washed away during the second, more-vigorous washing. The sulfur purity data are encouraging for the prospect of producing a marketable sulfur product.

A melting-point analysis was also performed on the sulfur crystals from the reactive crystallization runs. All of the sulfur samples from the crystallization runs listed in Table 4.2 had melting points between 112° to $119^{o}C$. This temperature range indicates that the crystalline morphology of the sulfur is a mixture of monoclinic sulfur (*m.p.* = $119^{o}C$) and orthorhombic sulfur (*m.p.* = $113^{o}C$). The relative amounts of each form are unknown from this analysis, and an attempted visual determination of the relative amounts did not provide any additional information. The sulfur crystals produced from the back-mixed reactive crystallization runs were similar in

appearance to those from the thermal crystallization runs. Figure 3.7 is a photomicrograph of the sulfur crystals produced from the reactive crystallization fluidized-bed run. The large agglomerates appear to be constructed from individual orthorhombic crystals.

4.8 UCBSRP Reactor/Crystallizer Design

A reactor/crystallizer was designed for a particular application of UCBSRP: the results of the design are presented below. The design procedure was based on the information produced from the thermal crystallization and reactive crystallization investigations and by using the computer simulation of the UCBSRP developed by Neumann (1986). The design is sized for treating a gasified-coal stream that fuels a 120-megawatt power plant. The composition, temperature, and pressure of the gasified-coal stream were taken from Neumann (1986). The molar H_2S concentration in the gasified-coal stream is 6140 parts per million (ppm). The stream information necessary to design the reactor/crystallizer was provided by the computer simulation of the UCBSRP. The solvent properties used in the simulation were those of diethylene glycol monomethyl ether (Dowanol DM). Dowanol DM was chosen as the solvent because the tray efficiencies and mass-transfer characteristics for the primary absorber were studied using Dowanol DM in a reactive absorption investigation (Hix, 1989). The flows and conditions of the streams entering and leaving the reactor/crystallizer are listed in Table 4.3. The homogeneous catalyst, 3-pyridyl carbinol (3PC), and its concentration of 0.015 M were also chosen to provide a second-order reaction-rate constant of 20 liter/mol-s (Neumann, 1986) as one of the inputs for the computer simulation. For the design of the reactor/crystallizer, the liquid-phase reaction of H_2S and SO_2 in the reactor/crystallizer was addressed first to determine reactor effluent compositions required to satisfy the mass balance and overall process constraints. Then, the crystallization of sulfur from the process solvent in the reactor/crystallizer was investigated to determine the sulfur crystal-size distribution.

The two most important design criteria for the UCBSRP reactor/crystallizer are that the H_2S concentration in the H_2S-free solvent (recycled back to the primary absorber) be very low and that the sulfur crystals be large. The size of the sulfur crystals must be large enough to use a centrifuge to separate the solids from the mother liquor. The upper limit for the H_2S concentration in the recycle stream is set by its equilibrium backpressure. Its backpressure cannot be larger than the corresponding concentration of H_2S specified for the treated gas exiting the primary absorber. The gas/liquid equilibrium calculations were made from the correlations provided by Sciamanna (1986, 1988). Since the H_2S concentration specified for the treated gas leaving the primary absorber is 1 ppm, the H_2S concentration in the recycle stream must not exceed 2.79 ppm.

4.8.1 Reactor/Crystallizer: One CSTR

The reaction performed in the reactor/crystallizer was characterized using the well-known continuous stirred-tank reactor (CSTR) model. The residence time of the liquid in the vessel was used to calculate the fraction conversion of the limiting component (H_2S), the H_2S concentration in the reactor effluent, and the reactor volume. The dependence of the latter two variables on the residence time is shown in Figure 4.8. With increasing residence time, the H_2S concentration in the effluent decreases but the vessel volume increases. At large residence times, a small reduction in the exit H_2S concentration requires a large increase in residence time, and as a result, a large increase in the reactor volume. For an acceptable H_2S concentration in the effluent stream (< 2.79 ppm), a huge reactor volume is required (> 2500 m^3). Obviously, the use of one CSTR as the reactor/crystallizer in the UCBSRP is unacceptable.

4.8.2 Reactor/Crystallizer: One CSTR and PFR

The volume of the reactor/crystallizer was reduced by relaxing the H_2S

concentration in the effluent stream. The H_2S concentration in the CSTR effluent is subsequently reduced by finishing the reaction using a plug-flow reactor (PFR). The PFR consumes nearly all of the limiting reactant (H_2S) in a minimal reactor volume, thereby providing the low H_2S concentration required in the recycle stream. The residence time in the CSTR was set at 10 minutes, yielding a 0.990 fraction conversion of H_2S. The CSTR volume of 244 m^3 produces an H_2S concentration in the effluent of 37.7 ppm. To achieve the H_2S concentration of 2.79 ppm in the recycle stream, a fraction conversion of 0.926 (based on the inlet concentrations to the PFR) is required in the PFR. The size of the PFR, 6.85 m^3, is small enough that its length (~30m) is comparable to the length of pipe between the reactor/crystallizer and primary absorber. Additional lengths of pipe for the PFR would reduce the H_2S concentration below 2.79 ppm in the recycle stream. This arrangement of a CSTR and PFR in series enables the H_2S specification in the treated gas to be met, but still yields a sizable reactor/crystallizer volume. The series arrangement also facilitates the production of large sulfur crystals. Most of the sulfur formed by the liquid-phase reaction of H_2S and SO_2 is crystallized in the CSTR vessel. The holding time in the vessel allows the crystallization kinetics to provide a crystal-size distribution which is suitably large. Since the sulfur crystals leaving the CSTR are large, any additional sulfur coming out of solution in the PFR is deposited on the existing crystals.

The results from the computer simulation and the reaction calculations were based on Dowanol DM being the process solvent. However, the crystallization study was made with Triglyme as the solvent. In order to use the information from the latter study, the results from the simulation and reaction calculations where Dowanol DM was the process solvent were assumed comparable to those results if Triglyme was the process solvent. This assumption is justified since the solubilities of H_2S and SO_2 and the solubility of sulfur in the two solvents are quite comparable (Sciamanna, 1986 & 1988). In addition, the crystallization of sulfur from Dowanol DM is expected to be

similar to that from Triglyme because the two solvents are chemically and physically alike.

The crystallization of sulfur performed in the CSTR was modeled as a mixed suspension, mixed-product removal (MSMPR) crystallizer. The crystal-size distribution of the sulfur crystals was predicted from the crystallization kinetics correlation obtained in the thermal crystallization study, Equation (4-8). The mass-average particle size of the sulfur crystals was calculated from the MSMPR design equation:

$$\tau = \left[\frac{6\rho_C k_V k_N \, \epsilon^h \, M_T^{j-1} \, \mathcal{L}^{i+3}}{4^{i+3}} \right]^{1/i-1} \tag{4-15}$$

The mass-average particle size of the crystal-size distribution is approximately 330 μm. In addition, roughly 95 percent of the crystal mass is larger than 110 microns. The slurry density of the sulfur solids produced from the two reactors is 1.95 kg/m^3 and is in the range studied in the thermal crystallization investigation.

4.8.3 Reactor/Crystallizer: Three CSTR's and One PFR

The volume of the reactor/crystallizer in the previous section is very large (244 m^3), particularly when sizing the vessel for operation at 2470 kPa (25 atm). The volume may be reduced further by constructing three CSTR's is series. The same PFR follows the three CSTR's to meet the H_2S concentration specification in the H_2S-free solvent stream. As in the previous case, the H_2S concentration in the effluent from the three-CSTR train was set at 37.7 ppm. Assuming equal CSTR volumes, the residence time in each vessel would then be only 19.3 seconds. This small residence time is outside the range of residence times studied in the thermal crystallization study. In addition, this residence time is only one order of magnitude larger than the reaction time scale discussed in Section 4.5.1. In light of these two facts, the results of this design should be used with caution.

This residence time yields a reactor volume of 7.84 m^3. The total volume of the

three CSTR's is 23.5 m^3, an order of magnitude less than for one-CSTR case. The fraction conversions of H_2S in the CSTR's, based on the H_2S concentration in the feed to the first CSTR, are 0.817, 0.958, and 0.990, respectively. The production of sulfur is largest in the first reactor, where most of the conversion occurs. The crystallization kinetics in Equation (4-8) were applied to the cascade of CSTR's to compute the crystal-size distribution and mass-average particle size of the sulfur crystals. The method of predicting the crystal-size distribution from the cascade of crystallizers was that presented by Larson and Wolff (1971). The mass-average particle size is approximately 240 μm, and roughly 95 percent of the crystal mass is larger than 95 μm. Although the mass-average particle size decreases with an increase in number of vessels, the crystal-size distribution is narrower. The benefit in using three reactor/crystallizers in series to greatly reduce the total reactor volume outweighs the decrease in size of the sulfur crystals.

Following the CSTR's and PFR, a solids/liquid separating device (not shown in Figure 1.1) would be required to produce a clarified recycle stream (H_2S-free solvent) to the primary absorber and also to produce a stream with an increased solids concentration. The slurry density of the effluent from the reactor/crystallizer is between 0.001 and 0.01 weight percent (much less than typical salt crystallizers) and requires a large degree of concentrating to feed into the pusher-type centrifuge. A solids concentration of approximately 50 weight percent is required to recover crystals larger than 100 μm in a pusher-type centrifuge (Baumann and Todd, 1973). To achieve the necessary solids concentration, a gravity or cyclone prethickener should be used between the crystallizer and the pusher-type centrifuge (Bamforth, 1965).

4.9 Summary

The reactor/crystallizer model, composed of a CSTR and an MSCPR crystallizer, predicted the experimental reactive crystallization data well. The model also predicted adequately the crystal-size distributions for runs with slurry densities larger than the

slurry densities used in the thermal crystallization study. No effect of the reaction of H_2S and SO_2 on the crystallization of sulfur was detected. The rate of reaction is sufficiently faster than the rate of crystallization so that the two processes may be treated sequentially. The sulfur crystals produced from the experimental apparatus were large, high-quality crystals. The purity and morphology of the crystals are typical of a marketable sulfur product. An industrial-sized reactor/crystallizer was designed for a particular application of the UCBSRP. The design satisfies the objectives for the development of the UCBSRP.

4.10 Nomenclature

B = fxn (τ, G, z, L_c) [see Chapter 3]

B^o = nucleation rate [= n^oG] (#/min-cm^3)

C_i = concentration of limiting component (mol/liter)

$C_{i,0}$ = concentration of limiting component in mixing-cup feed (mol/liter)

C_k = concentration of sulfur (S_8) in k^{th} stream (mol/liter)

C_{H2S} = concentration of H_2S in solution (mol/liter)

C_{SO2} = concentration of SO_2 in solution (mol/liter)

f_i = fraction conversion of limiting component

f_1,f_2 = fxn (τ, G, z, L_c) [see Chapter 3]

G = crystal growth rate (μm/min)

h = exponent for the specific power input [= 0]

i = kinetic order [= 1.55]

j = secondary nucleation order [= 0.943]

k = integer denoting an inlet or outlet stream
1,2 = feeds; 3 = effluent

k_N = kinetic constant [= 1.04]

k_V = crystal volumetric shape factor [= $\pi/6$]

k_2 = second order rate constant (liter/mol-sec)

L_c = MSCPR model parameter [= 250.] (μm)

$\mathscr{L}$ = mass-average particle size (μm)

M_T = slurry density of all crystals in suspension (kg/m^3)

M_T^+ = slurry density of over-sized crystals (kg/m^3)

M_T(max) = maximum slurry density of sulfur crystals (kg/m^3)

$n^o\rho_C k_V/M_T$ = specific nuclei population density (#/μm-cm^3)

Q = volumetric flow rate through reactor (m^3/min)

Q_k = volumetric flow rate of kth stream (m^3/min)

r = reaction rate (mol/sec)

r_{S8} = rate of appearance of sulfur (S_8) from reaction [= $r/(3/8)$] (mol/sec)]

$r_{i,out}$ = rate of disappearance of limiting reactant evaluated at reactor outlet conditions (mol/min)

V = volume of reactor (m^3)

z = MSCPR model parameter [= 2.25]

α = Damköhler number [= $\tau k_2 C_{H2S,0}$ or $2\tau k_2 C_{SO2,0}$]

β = ratio of reactant concentrations in mixing-cup feed [= $2C_{SO2,0}/C_{H2S,0}$ or $C_{H2S,0}/2C_{SO2,0}$]

ϵ = specific power input (watts/kg solution)

ρ_C = crystal density (kg/m^3)

τ = residence time of crystals in crystallizer [= V/Q_3] (min)

List of Tables for Chapter 4

4.1 Operating Conditions for the Reactive Crystallization Runs

4.2 Results from Sulfur Purity Analysis using Gas Chromatography

4.3 UCBSRP Crystallizer Stream Flows and Conditions

List of Figures for Chapter 4

4.1 Reaction Crystallization Apparatus: Back-Mixed Crystallizer

4.2 Reaction Crystallization Apparatus: Fluidized-Bed Crystallizer

4.3 Effect of Reactor Variables on Fraction Conversion

4.4 Crystal-Size Distribution for Run 64

4.5 Crystal-Size Distribution for Run 65

4.6 Crystal-Size Distribution for Run 66

4.7 Photomicrograph of Sulfur Crystals from Fluidized-Bed Crystallization Run

4.8 Effect of Residence Time on CSTR Effluent and Volume

Table 4.1

Operating Conditions for the Reactive Crystallization Runs

Run:	64	65	66
Residence Time (min)	22.6	38.6	5.86
SO_2 Soln Flow (ml/min)	36.0	1.0	120
H_2S Soln Flow (ml/min)	47.0	47.5	200
SO_2 Conc. (mol fraction)	0.0367	0.0886	0.0863
H_2S Conc. (mol fraction)	0.0361	0.0446	0.0830
$C_{SO2,0}$[1] (mol/liter)	0.0901	0.0107	0.1896
$C_{H2S,0}$[1] (mol/liter)	0.116	0.251	0.308
$2C_{SO2,0}/C_{H2S,0}$[1]	1.55	0.09	1.23
Damköhler Number[1]	3160.	496.	2160.
Fraction Conversion[2]	.9994	.9999	.9980
Slurry Density:			
Maximum Slurry Density[3] (kg/m^3)	5.09	0.34	14.43
Predicted M_T[4] (kg/m^3)	2.77	0.21	9.76
% reduction	45.6	38.2	32.4
Mass-Average Particle Size:			
Measured $\mathscr{L}$ (μm)	253.8	246.6	226.8
Predicted $\mathscr{L}$[4] (μm)	239.3	267.3	231.2
% error	5.7	8.4	1.9

Notes:

[1]Assumed $\rho_L(SO_2\ \text{Soln}) = \rho_L(H_2S\ \text{Soln}) = \rho_L(\text{Triglyme})$

[2]Equation (4-5)
[3]Equation (4-6)
[4]Equations (4-8) through (4-12)

Table 4.2

Results from Sulfur Purity Analysis using Gas Chromatography

Run #	Residence Time(min)	Type of Run	Wt. % Triglyme in Solid Sulfur
63	-	fluidized-bed	0.223 ± 0.026
63	-	fluidized-bed	0.201 ± 0.038
66	5	back-mixed (before washing)	0.291 ± 0.038
66	5	back-mixed (after washing)	0.200 ± 0.025

Table 4.3

UCBSRP Crystallizer Stream Flows and Conditions

Stream #	1	2	3
Component Flows (mol/s)			
Solvent	2520.	36.4	2560.
H2O	717.	5.26	734.
H2S	11.7	-	0.00961
SO2	0.461	7.47	2.07
S8 (dissolved)	1.50	0.0147	1.03
S8 (solids)	-	-	3.71
Pressure (kPa)	2470.	2470.	2470.
Temperature (K)	342.	303.	303.

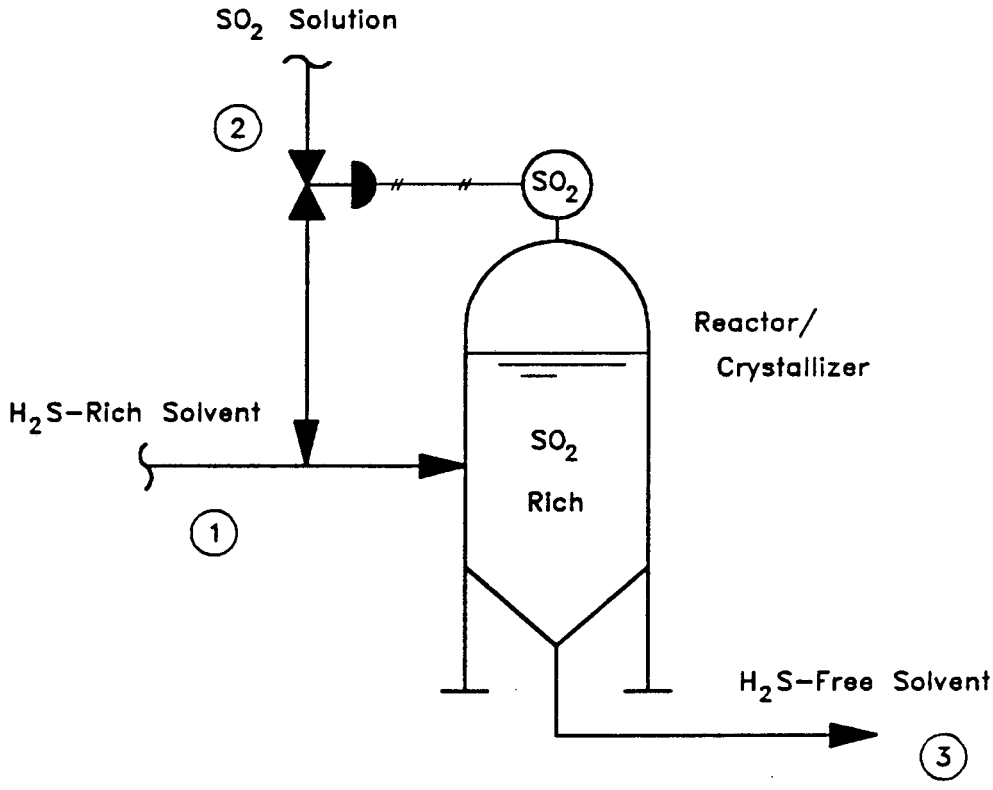

Figure 4.1
Reactive Crystallization Apparatus
Back–Mixed Crystallizer

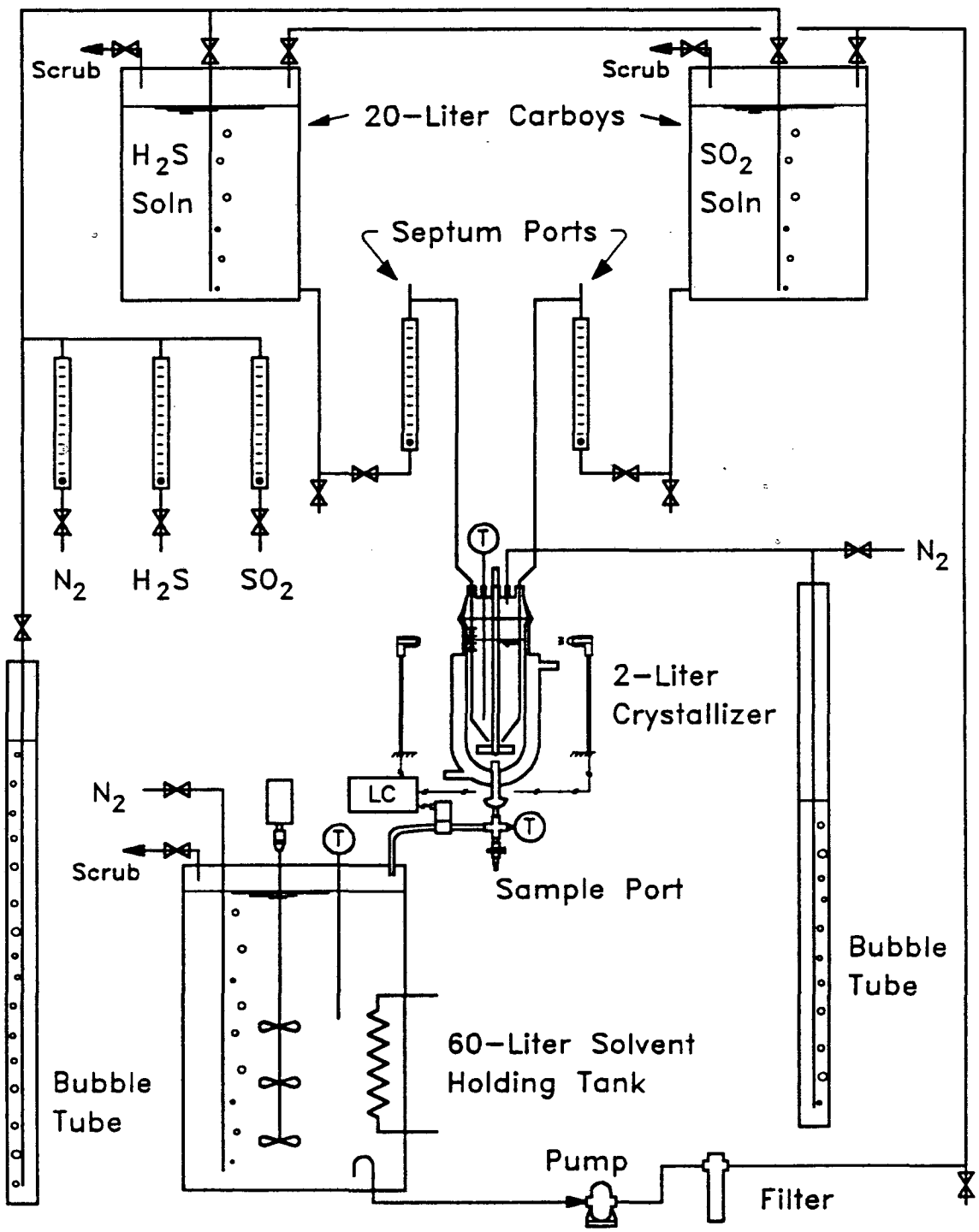

Figure 4.2
Reactive Crystallization Apparatus
Fluidized-Bed Crystallizer

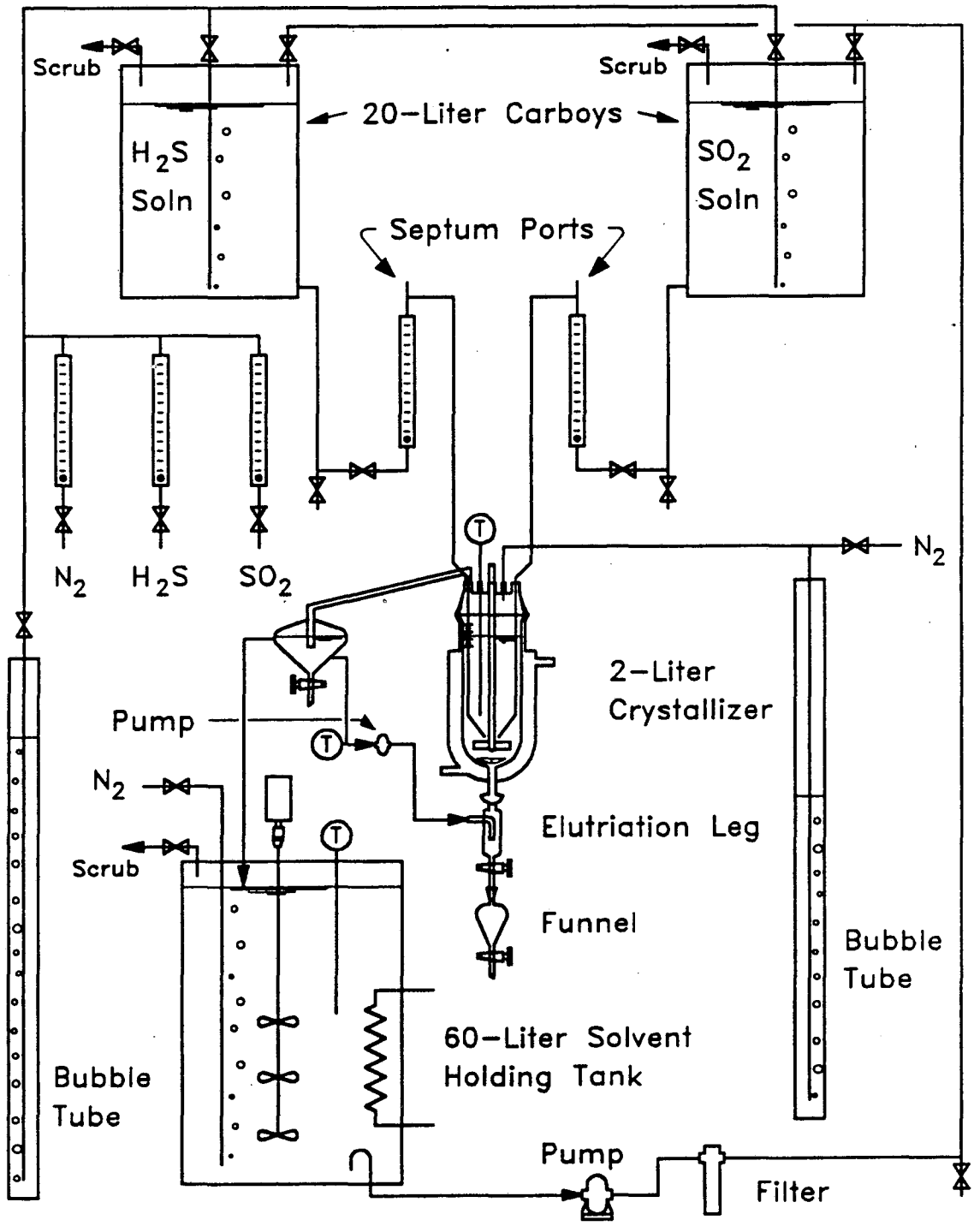

Figure 4.3
Effect of Reactor Variables on Fraction Conversion

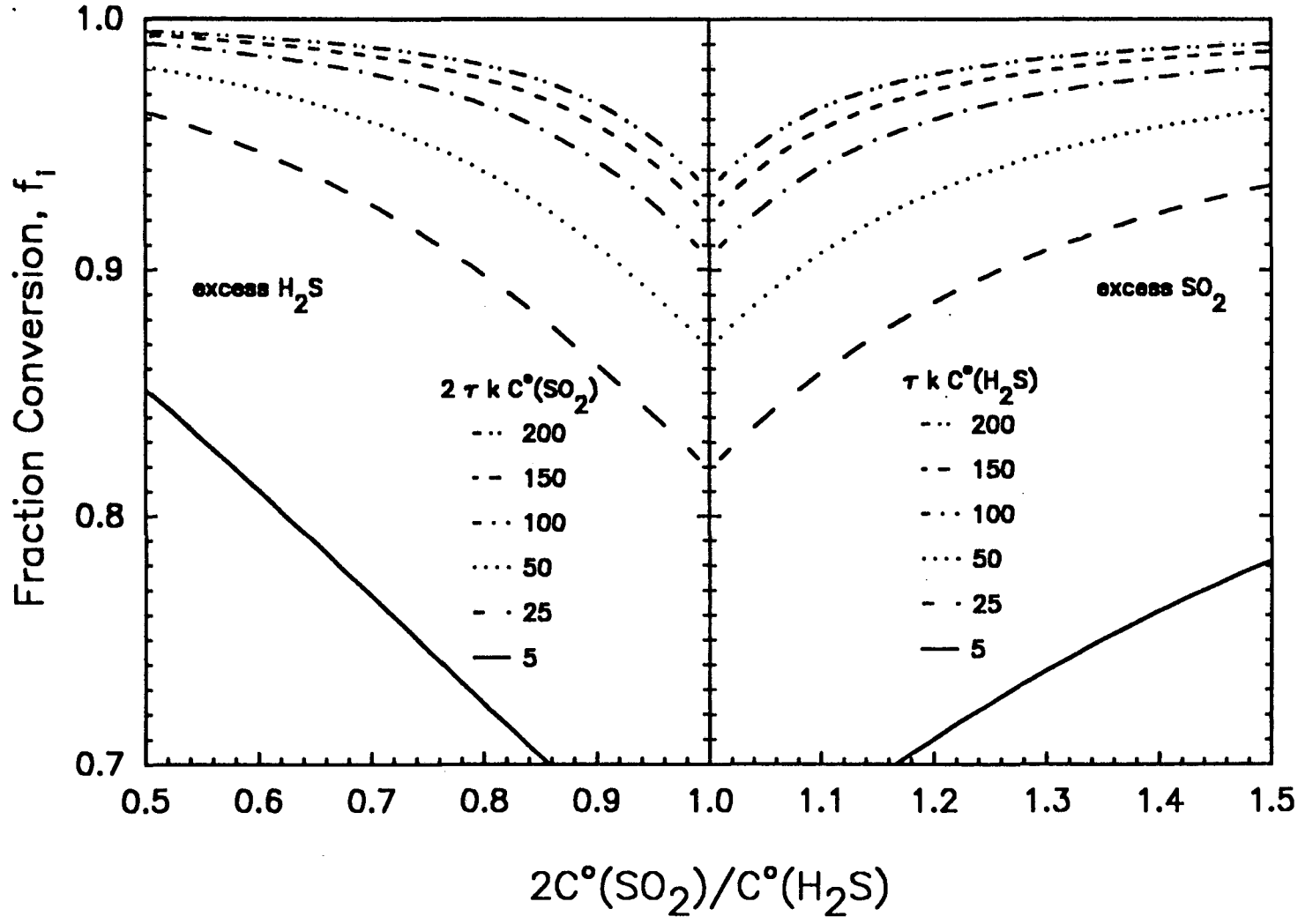

Figure 4.4

Predicted CSD from Reactor–Crystallizer Model

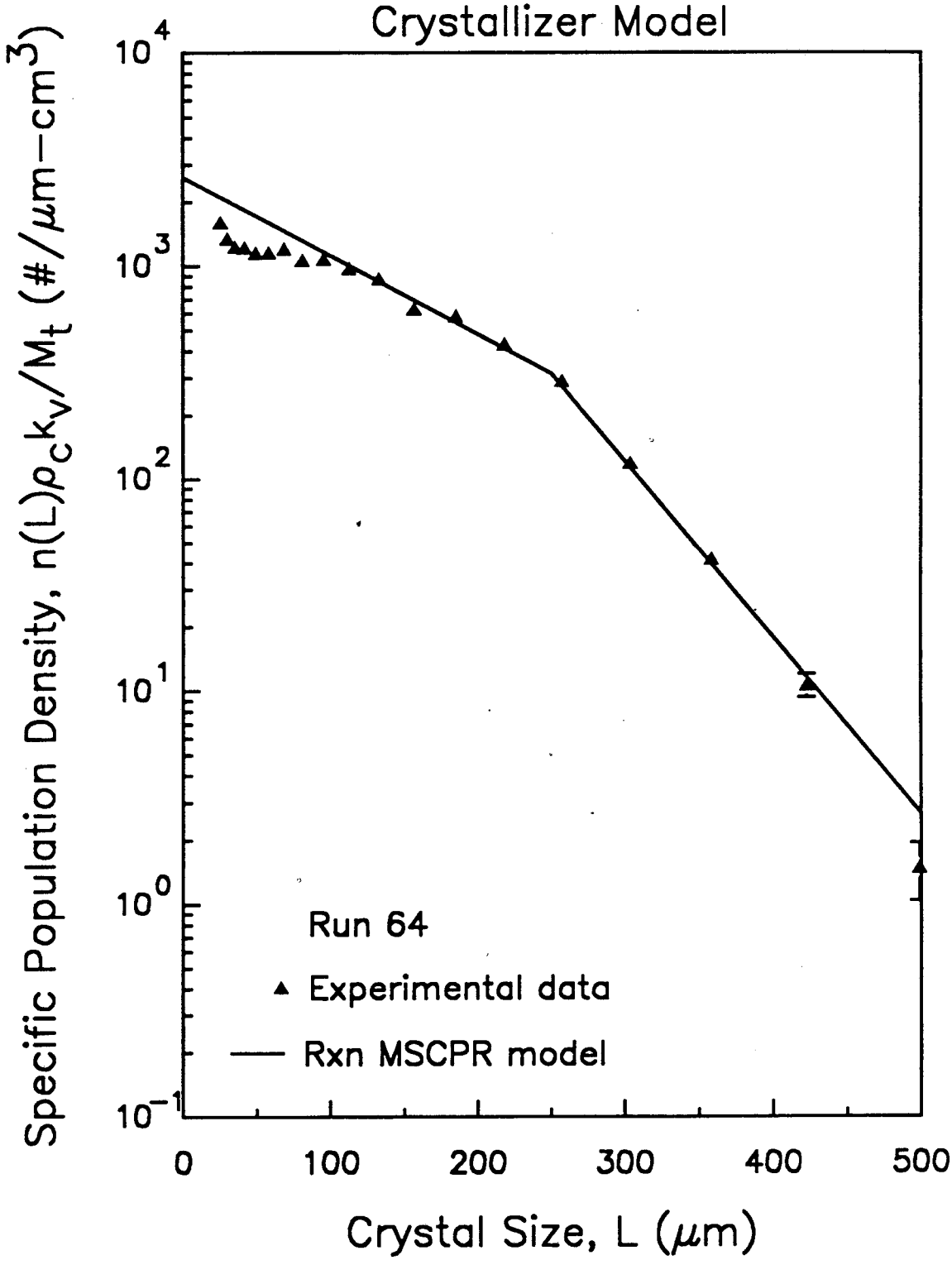

Figure 4.5

Predicted CSD from Reactor–Crystallizer Model

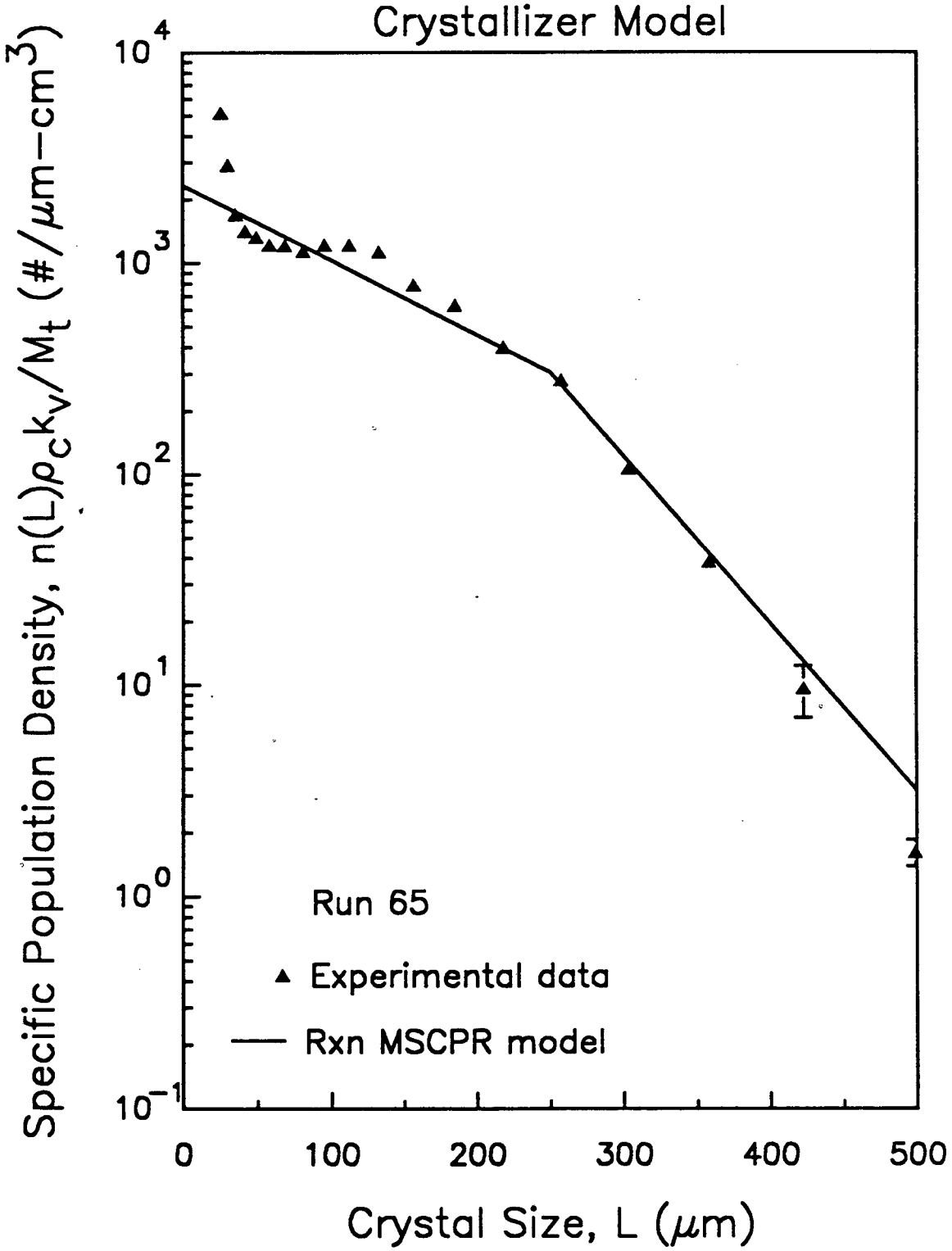

Figure 4.6

Predicted CSD from Reactor–Crystallizer Model

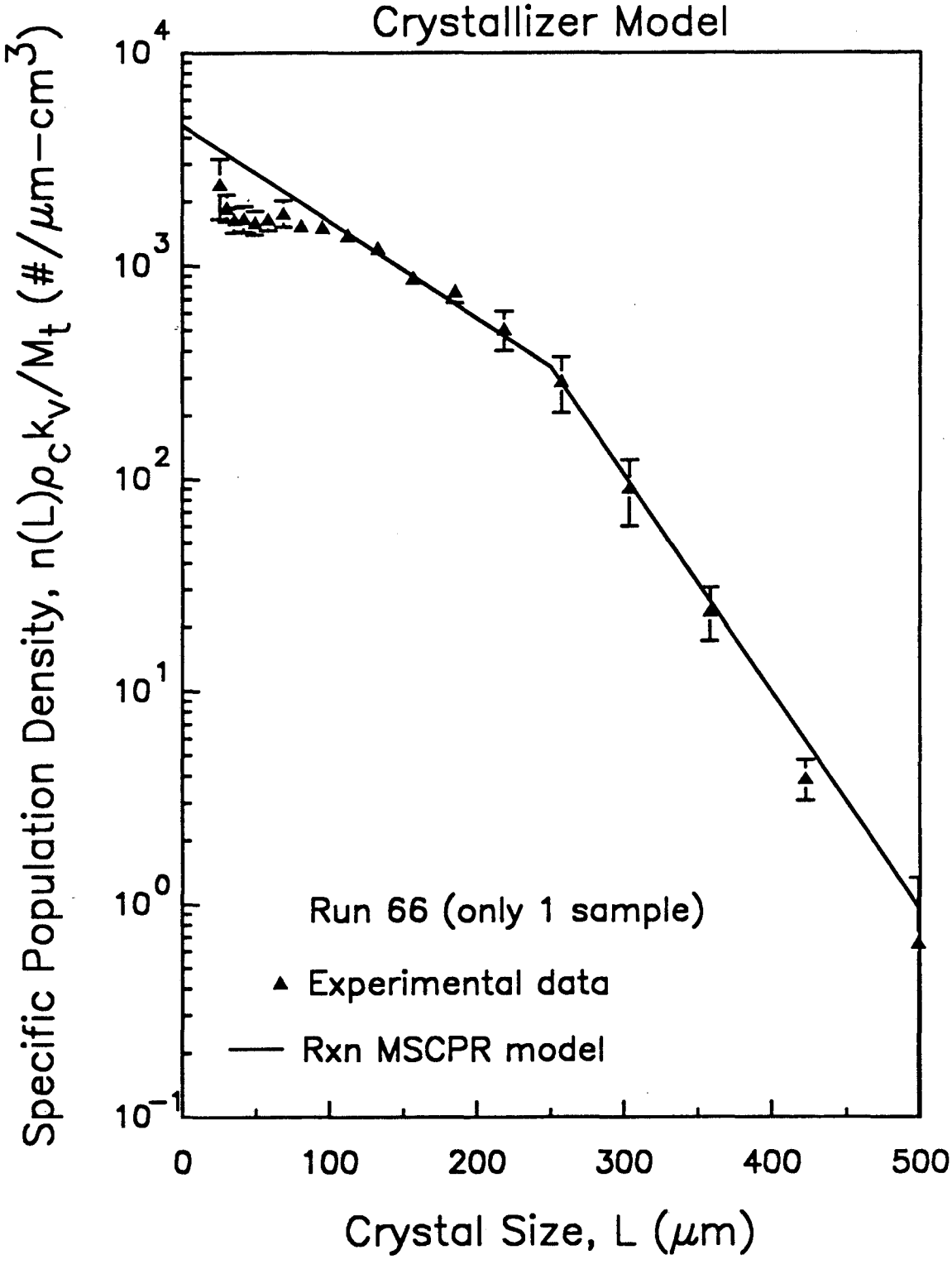

Figure 4.7 Photomicrograph of Sulfur Crystals from Fluidized-Bed Crystallization Run (p.181)

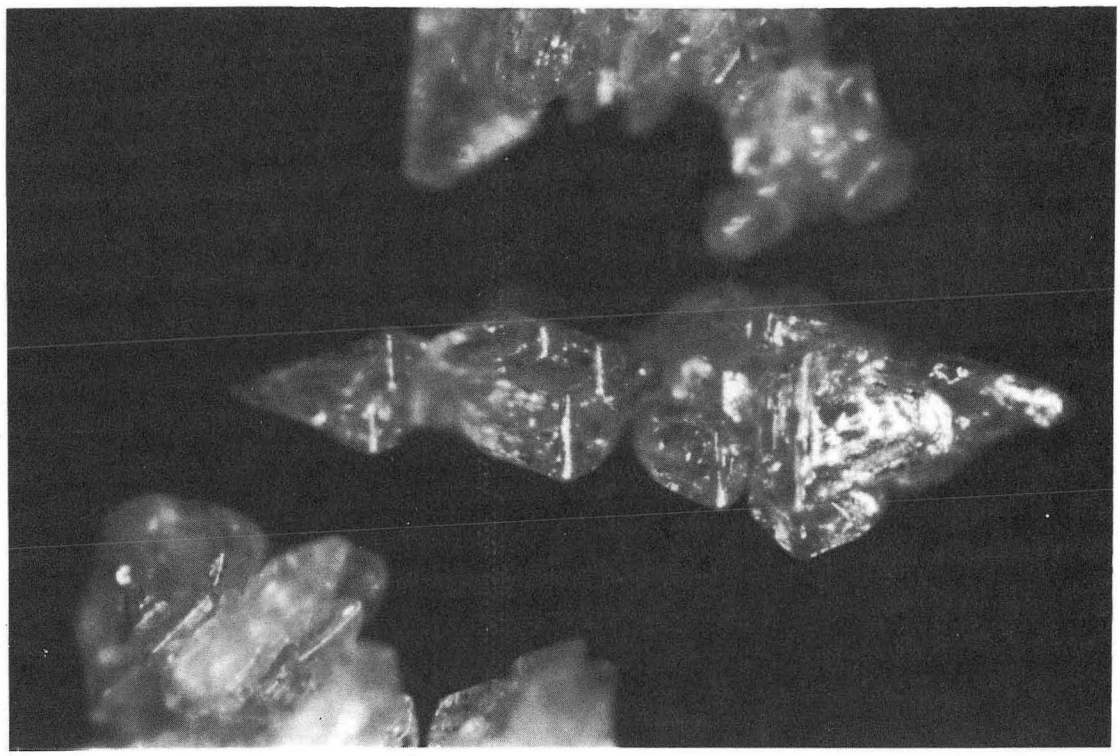

100 μm

XBB 899-7472

Figure 4.8

Effect of Residence Time on CSTR Effluent and Volume

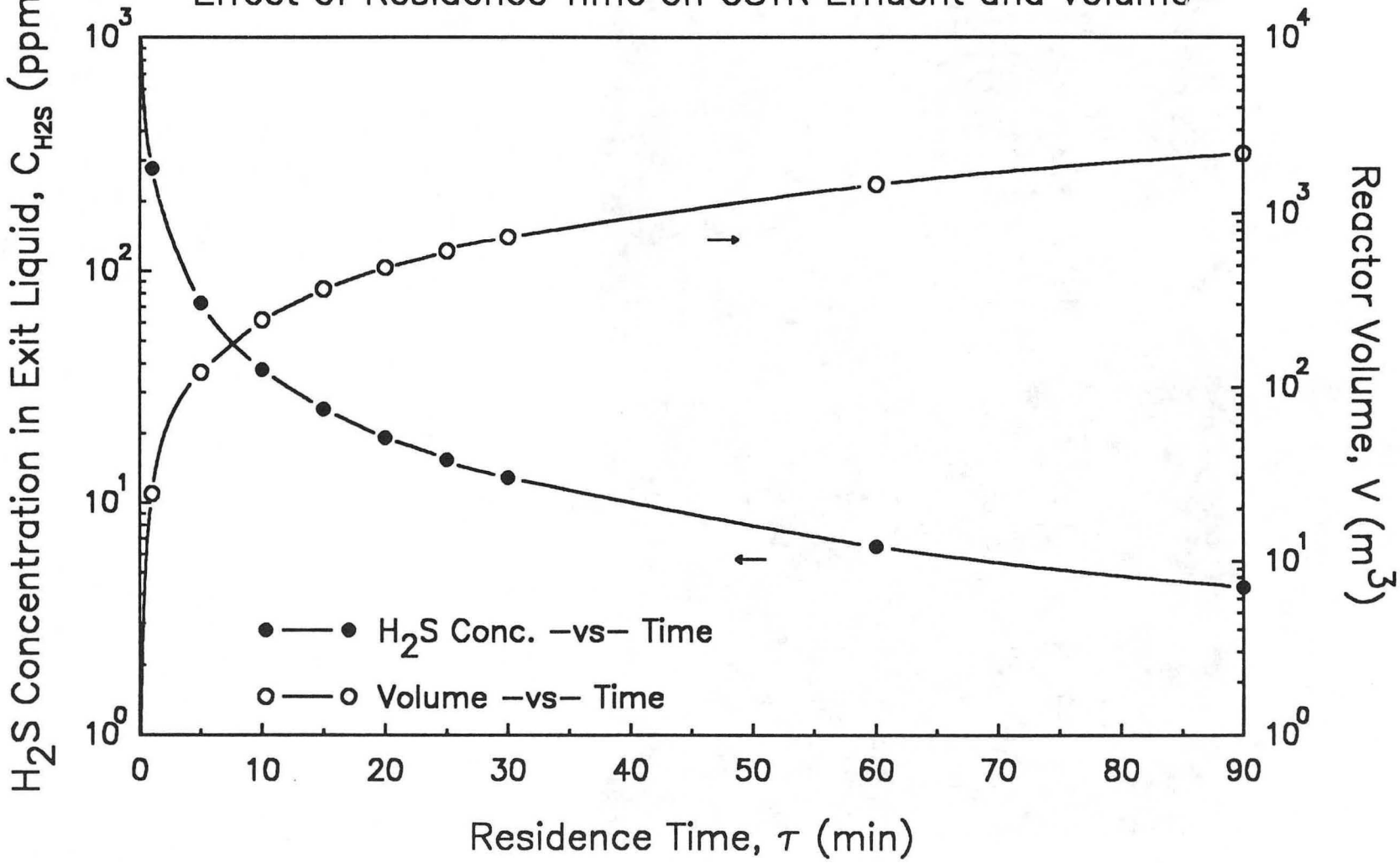

REFERENCES

CHAPTER 1

Colson, T. E. "Development and Evaluation of a Process to Produce Hydrogen from Coal," M.S. Thesis, Department of Chemical Engineering, University of California, Berkeley, CA 1989.

Crean, D. J. "Kinetics and Corrosion Studies of H_2S and SO_2 in Polyglycol Ethers," M.S. Thesis, Department of Chemical Engineering, University of California, Berkeley, CA 1987.

Ferguson, P. A. *Hydrogen Sulfide Removal from Gases, Air, and Liquids*, Noyes Data Corp: Park Ridge, NJ 1975.

Hix, R. M. "Reactive Absorption of H_2S by an SO_2-Rich Polyglycol Ether Solvent," Ph.D. Dissertation, Department of Chemical Engineering, University of California, Berkeley, CA 1989.

Kohl, A. L. and F. C. Riesenfeld *Gas Purification*, 4th ed., Gulf Publishing Co: Houston, TX 1985.

Lynn, S.; Neumann, D. W.; Sciamanna, S. F.; Vorhis, F. H. "A Comparison of the UCB Sulfur Recovery Process with Conventional Sulfur Recovery Technology for Treating Recycle Gas from a Crude Oil Residuum Hydrotreater," *Environ. Prog.*, 6(4), 257 1987.

Neumann, D. W. "Process Studies for a New Method of Removing H_2S from Industrial Gas Streams," Ph.D. Dissertation, Department of Chemical Engineering, University of California, Berkeley, CA 1986.

Neumann, D. W. and S. Lynn "Kinetics of the Reaction of Hydrogen Sulfide and Sulfur Dioxide in Organic Solvents," *Ind. Eng. Chem. Process Des. Dev.*, 25(1), 248 1986.

Sciamanna, S. F. "Development of a Process for Simultaneous Desulfurization, Drying, and Recovery of Natural Gas Liquids from Natural Gas Streams," Ph.D. Dissertation, Department of Chemical Engineering, University of California, Berkeley, CA 1986.

Sciamanna, S. F. and S. Lynn "Sulfur Solubility in Pure and Mixed Organic Solvents," *Ind. Eng. Chem. Res.*, 27(3), 485 1988.

Sciamanna, S. F. and S. Lynn "Solubility of Hydrogen Sulfide, Sulfur Dioxide, Carbon Dioxide, Propane, and *n*-Butane in Poly(glycol ethers)," *Ind. Eng. Chem. Res.*, 27(3), 492 1988.

Sciamanna, S. F. and S. Lynn "An Integrated Process for Simultaneous Desulfurization, Dehydration, and Recovery of Hydrocarbon Liquids from Natural Gas Streams," *Ind. Eng. Chem. Res.*, 27(3), 500 1988.

CHAPTER 2

Broul, M.; Nývlt, J.; Söhnel, O. "Solubilities in Binary Aqueous Solutions," in *Industrial Crystallization 84*, edited by S. J. Jancic and E. J. de Jong, Elsevier Science Publishers B. V.: Amsterdam, The Netherlands p.253 1984.

Prausnitz, J. M.; Lichtenthaler, R. N.; Gomes de Azevedo, G. *Molecular Thermodynamics of Fluid-Phase Equilibria*, 2nd ed., Prentice-Hall: Englewood Cliffs, NJ 1986.

Sciamanna, S. F. "Development of a Process for Simultaneous Desulfurization, Drying, and Recovery of Natural Gas Liquids from Natural Gas Streams," Ph.D. Dissertation, Department of Chemical Engineering, University of California, Berkeley, CA 1986.

Sciamanna, S. F. and S. Lynn "Sulfur Solubility in Pure and Mixed Organic Solvents," *Ind. Eng. Chem. Res.*, 27(3), 485 1988.

CHAPTER 3

Abegg, C. F.; Stevens, J. D.; Larson, M. A. "Crystal Size Distributions in Continuous Crystallizers when Growth Rate is Size Dependent," *AIChE J.*, 14(1), 118 1968.

Akselrub, G. A.; Semenushchun, E. M.; Moma, Y. V. "Kinetics of the Polythermal Crystallization of Sulfur from Solutions of Perchloroethylene," *Zh. Fiz. Khim.*, 50(11), 2846 1976.

Canning, T. F. and A. D. Randolph "Some Aspects of Crystallization Theory: Systems that Violate McCabe's Delta-L Law," *AIChE J.*, 13(1), 5 1967.

Clontz, N. A. and W. L. McCabe "Contact Nucleation of Magnesium Sulfate Heptahydrate," *Chem. Eng. Prog. Sym. Ser.*, 67(110), 6 1971.

Garside, J. and M. B. Shah "Crystallization Kinetics from MSMPR Crystallizers," *Ind. Eng. Chem. Process Des. Dev.*, 19(4), 509 1980.

Jancić, S. J. and P. A. M. Grootscholten *Industrial Crystallization*, Delft University Press -- Kluwer Academic Publishers: Hingham, MA 1984.

Kneule, F. *Chem. Ing. Tech.* 28, 221 1956.

Kuster, O. R. US Patent 3,337,307 1967.

Larson, M. A.; Timm, D. C.; Wolff, P. R. "Effect of Suspension Density on Crystal Size Distribution" *AIChE J.*, 14(3), 448 1968.

Larson, M. A. and A. D. Randolph "Size Distribution Analysis in Continuous Crystallization," *Chem. Eng. Prog. Sym. Ser.*, 65(95), 1 1969.

McCabe, W. L. "Crystal Growth in Aqueous Solutions," *Ind. Eng. Chem.*, **21**(1), 30 1929.

Neumann, D. W. "Process Studies for a New Method of Removing H_2S from Industrial Gas Streams," Ph.D. Dissertation, Department of Chemical Engineering, University of California, Berkeley, CA 1986.

Neumann, D. W. and S. Lynn "Kinetics of the Reaction of Hydrogen Sulfide and Sulfur Dioxide in Organic Solvents," *Ind. Eng. Chem. Process Des. Dev.*, **25**(1), 248 1986.

Nuffield, C. P. "Crystallization of Sulfur from Xylene," *Sch. Sci. Rev.*, **53**(185), 765 1972.

Nývlt, J.; Söhnel, O.; Matuchova, M.; Broul, M. *The Kinetics of Industrial Crystallization*, Elsevier: New York, NY 1985.

Randolph, A. D. "The Mixed Suspension, Mixed Product Removal Crystallizer as a Concept in Crystallizer Design," *AIChE J.*, **11**(3), 424 1965.

Randolph, A. D.; Beckman, J. R.; Kraljevich, Z. I. "Crystal Size Distribution Dynamics in a Classified Crystallizer," *AIChE J.*, **23**(4), 500 1977.

Randolph, A. D. and M. A. Larson *Theory of Particulate Processes: Analysis and Techniques of Continuous Crystallization*, 2nd ed., Academic Press: San Diego, CA 1988.

Rao, K. S.; Rewatkar, V. B.; Joshi, J. B. "Critical Impeller Speed for Solid Suspension in Mechanically Agitated Contactors," *AIChE J.*, **34**(8), 1332 1988.

Rushton, J. H.; Costich, E. W.; Everett, H. J. "Power Characteristics of Mixing Impellers," *Chem. Eng. Prog.*, **46**(8), 395 1950.

Sciamanna, S. F. "Development of a Process for Simultaneous Desulfurization, Drying, and Recovery of Natural Gas Liquids from Natural Gas Streams," Ph.D. Dissertation, Department of Chemical Engineering, University of California, Berkeley, CA 1986.

Sciamanna, S. F. and S. Lynn "Sulfur Solubility in Pure and Mixed Organic Solvents," *Ind. Eng. Chem. Res.*, **27**(3), 485 1988.

Thackray, M. "Phase Transition Rate Measurements," in *Elemental Sulfur*, edited by B. Meyer, John Wiley & Sons: New York, NY 1965.

Tuller, W. N., editor, *The Sulphur Data Book*, McGraw-Hill: New York, NY 1954.

White, E. T. and A. D. Randolph "Graphical Solution of the Material Balance Constraint for MSMPR Crystallizers," *AIChE J.*, **33**(4), 686 1987.

Zwietering, T. N. "Suspending of Solid Particles in Liquid Agitators," *Chem. Eng. Sci.*, **8**, 244 1958.

CHAPTER 4

Bamforth, A. W. *Industrial Crystallization*, The Macmillan Company: New York, NY 1965.

Baumann, D. K. and D. B. Todd "When to Use a Pusher Centrifuge," *Chem. Eng. Prog.*, 69(9), 62 1973.

Garside, J. and N. S. Tavare "Mixing, Reaction, and Precipitation: Limits of Micromixing in an MSMPR Crystallizer," *Chem. Eng. Sci.*, 40(8), 1485 1985.

Hill, C. G. *An Introduction to Chemical Engineering Kinetics and Reactor Design*, John Wiley & Sons: New York, NY 1977.

Hix, R. M. "Reactive Absorption of H_2S by an SO_2-Rich Polyglycol Ether Solvent," Ph.D. Dissertation, Department of Chemical Engineering, University of California, Berkeley, CA 1989.

Larson, M. A. and P. R. Wolff "Crystal Size Distributions from Multistage Crystallizers," *Chem. Eng. Prog. Sym. Ser.* 67(110), 97 1971.

Neumann, D. W. "Process Studies for a New Method of Removing H_2S from Industrial Gas Streams," Ph.D. Dissertation, Department of Chemical Engineering, University of California, Berkeley, CA 1986.

Neumann, D. W. and S. Lynn "Kinetics of the Reaction of Hydrogen Sulfide and Sulfur Dioxide in Organic Solvents," *Ind. Eng. Chem. Process Des. Dev.*, 25(1), 248 1986.

Sciamanna, S. F. "Development of a Process for Simultaneous Desulfurization, Drying, and Recovery of Natural Gas Liquids from Natural Gas Streams," Ph.D. Dissertation, Department of Chemical Engineering, University of California, Berkeley, CA 1986.

Sciamanna, S. F. and S. Lynn "Solubility of Hydrogen Sulfide, Sulfur Dioxide, Carbon Dioxide, Propane, and *n*-Butane in Poly(glycol ethers)," *Ind. Eng. Chem. Res.*, 27(3), 492 1988.

Treleavan, C. R. and A. H. Tobgy "Conversion in Reactors Having Separate Reactant Feed Streams: The Maximum State of Mixedness," *Chem. Eng. Sci.*, 26, 1259 1971.

APPENDIX A

A.1 Experimental Data: Sulfur Solubility in Polyglycol Ether Solvents

Data from Low Temperature Study

Sulfur in Triglyme
Sulfur in Dowanol DM

Data from Sciamanna (1986, 1988)

Diethers:
- Sulfur in Diglyme
- Sulfur in Triglyme
- Sulfur in Tetraglyme
- Sulfur in Diglyme w/ 5.0 wt% Water

Monoethers:
- Sulfur in Dowanol DM
- Sulfur in Dowanol DM w/ 2.5 wt% Water
- Sulfur in Dowanol DM w/ 5.0 wt% Water

A.2 Computer Programs for Data Regression

SOLWT.FOR Determine the constants in Equation (2-2)

SOLWWT.FOR Determine the constant D in Equation (2-7)

A.1 Experimental Data: Sulfur Solubility in Polyglycol Ether Solvents

Low Temperature Study: Sulfur in Triglyme

Wt% S_8	T_s(°C)	T_m(K)/T_s(K)
0.1349	8.0	1.37
0.0963	8.1	1.37
0.1552	10.0	1.36
0.1296	10.0	1.36
0.1631	12.0	1.35
0.1348	12.1	1.35
0.1558	14.0	1.34
0.1343	14.0	1.34
0.1649	16.0	1.33
0.1922	16.2	1.33
0.1643	18.0	1.33
0.2155	18.1	1.33
0.1950	20.0	1.32
0.1922	20.0	1.32
0.1732	23.0	1.30
0.1739	23.1	1.30
0.2279	23.2	1.30
0.2171	26.0	1.29
0.2193	26.2	1.29
0.2438	26.4	1.29
0.2256	29.3	1.28
0.3349	29.4	1.28
0.2367	29.6	1.27
0.2343	31.0	1.27
0.2987	34.1	1.26
0.2994	34.4	1.25
0.4012	40.5	1.23
0.4008	41.6	1.23

Low Temperature Study: Sulfur in Dowanol DM

Wt% S_8	T_s(°C)	T_m(K)/T_s(K)
0.0527	2.0	1.40
0.0547	3.8	1.39
0.0603	5.0	1.39
0.0722	7.2	1.38
0.0582	9.8	1.36
0.0816	12.4	1.35
0.0712	14.8	1.34
0.0986	17.8	1.33
0.0912	20.6	1.31
0.1095	25.0	1.29
0.1073	28.0	1.28
0.1307	32.0	1.26

T_m = Melting Temperature of Sulfur (385.95K)
T_s = Temperature of the Saturated Sulfur/Solvent System

Sciamanna Data: Sulfur in Diglyme

Wt% S_8	T_s(°C)	T_m(K)/T_s(K)
1.00	61.2	1.15
2.00	81.5	1.09
3.00	95.8	1.05
4.00	105.5	1.02
5.00	112.5	1.00

Sciamanna Data: Sulfur in Triglyme

Wt% S_8	T_s(°C)	T_m(K)/T_s(K)
1.00	63.5	1.15
2.00	81.5	1.09
3.00	94.5	1.05
4.00	104.5	1.02

Sciamanna Data: Sulfur in Tetraglyme

Wt% S_8	T_s(°C)	T_m(K)/T_s(K)
0.50	50.5	1.19
1.00	66.0	1.14
1.50	75.5	1.11
2.00	82.5	1.09
2.50	88.5	1.07
3.00	95.0	1.05
3.50	103.0	1.03
4.00	109.3	1.01

Sciamanna Data: Sulfur in Diglyme w/ 5.0 wt% Water

Wt% S_8	T_s(°C)	T_m(K)/T_s(K)
0.50	58.3	1.16
0.60	60.5	1.16
0.70	66.5	1.14
0.90	72.8	1.12
1.00	77.7	1.10
1.50	86.3	1.07

T_m = Melting Temperature of Sulfur (385.95K)
T_s = Temperature of the Saturated Sulfur/Solvent System

Sciamanna Data: Sulfur in Dowanol DM

Wt% S_8	T_s(°C)	T_m(K)/T_s(K)
0.43	63.5	1.15
0.45	67.2	1.13
0.51	67.0	1.13
0.75	75.0	1.11
0.82	79.6	1.09
0.82	80.0	1.09
1.00	84.5	1.08
1.05	87.4	1.07
1.09	84.0	1.08
1.09	90.0	1.06
1.09	90.0	1.06
1.10	88.5	1.07
1.27	94.5	1.05
1.27	93.2	1.05
1.39	95.0	1.05
1.45	97.5	1.04
1.66	100.0	1.03
1.73	100.5	1.03
1.97	105.5	1.02
2.09	107.8	1.01
2.27	110.8	1.01
2.36	111.0	1.00

Sciamanna Data: Sulfur in Dowanol DM w/ 2.5 wt% Water

Wt% S_8	T_s(°C)	T_m(K)/T_s(K)
0.40	68.3	1.13
0.50	75.0	1.11
0.70	82.2	1.09
1.10	94.3	1.05
1.60	105.0	1.02
2.00	109.8	1.01

Sciamanna Data: Sulfur in Dowanol DM w/ 5.0 wt% Water

Wt% S_8	T_s(°C)	T_m(K)/T_s(K)
0.40	73.0	1.11
0.50	80.8	1.09
0.60	85.2	1.08
0.70	88.8	1.07
0.80	93.8	1.05
1.00	97.0	1.04
1.20	104.1	1.02
1.40	107.2	1.01
1.60	111.5	1.00

T_m = Melting Temperature of Sulfur (385.95K)
T_s = Temperature of the Saturated Sulfur/Solvent System

APPENDIX

The remaining Appendices to this report, a 35-page listing of the computer codes used to analyze experimentally-determined crystal-size distribution data and to design the crystallizers discussed above, is available upon request from:

Professor Scott Lynn
Department of Chemical Engineering
University of California
Berkeley, CA 94720-9989

LAWRENCE BERKELEY LABORATORY
TECHNICAL INFORMATION DEPARTMENT
1 CYCLOTRON ROAD
BERKELEY, CALIFORNIA 94720